



**DOLPHIN**  
Hybrid  
*Swimming in the skies*



**2017 – 2018 Undergraduate Team Aircraft Design Competition**

**Hybrid-Electric General Aviation Aircraft (HEGAA)**

Presented by Federal University of Uberlândia

Department of Aerospace Engineering

Minas Gerais, Brazil



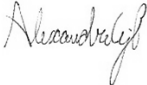
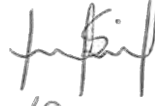
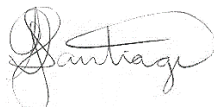
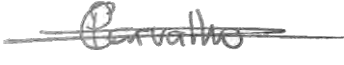
# 2017 – 2018 Undergraduate Team Aircraft Design Competition

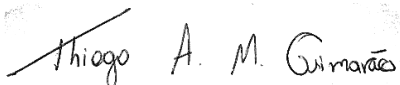
## Hybrid-Electric General Aviation Aircraft (HEGAA)

Presented by Federal University of Uberlândia

Department of Aerospace Engineering

Minas Gerais, Brazil

Team Members	AIAA Numbers	Signatures
Alexandre Acerra Gil	922668	
Eduardo Pavoni Gamba	922678	
Gabriel Araújo Hernández	922675	
Guilherme Miquelim Caires	922581	
Higor Luis Silva	922459	
João Paulo Vieira	922563	
Kimberly Costa Carvalho	922564	
Luiz Gustavo Santiago	922576	
Pedro Brito	922566	
Roberto Martins de Castro Neto	922571	



Advisor: Dr. Thiago A. M. Guimarães - 498079



## Table of Contents

1.	Introduction .....	6
2.	Design Requirements and Proposals .....	7
3.	Market Research.....	9
4.	Conceptual Design.....	10
4.1.	Initial Design Estimate.....	11
4.2.	Hybrid-Electric Aircraft Design.....	17
4.3.	Design Assumptions .....	19
4.3.1.	Typical Aircraft Mission Profile.....	20
4.3.2.	Battery Design.....	21
4.3.2.	Internal Combustion Engine (ICE).....	22
4.4.	Genetic Algorithm Implementation .....	23
4.5.	Aircraft of Comparable Role and Configuration.....	30
5.	Aerodynamic Analysis .....	32
5.1.	Conceptual Aerodynamic Design .....	32
5.1.1.	Wing Planform .....	32
5.1.2.	Airfoil Section .....	34
5.1.3.	Optimization of the Wing Planform .....	36
5.2.	High Lift Devices.....	37
5.3.	Fuselage .....	37
5.4.	CFD Analysis.....	38
5.4.1.	CFD Optimization .....	38
5.5.	Interference Drag – Wing Fuselage .....	39
5.6.	Winglets.....	40
5.7.	Final Drag Polar.....	41
6.	Performance Analysis .....	42



6.1. Take-off analysis.....	42
6.2. Aircraft climb.....	43
6.3. Cruise condition.....	45
6.4. Landing.....	48
6.5. Payload-Range Diagram.....	48
6.6. Emergency situation.....	49
7. Structural Analysis.....	50
7.1. Structural Wing Design.....	56
7.2. Structural Empennage Design.....	61
7.2.1. Structural Horizontal Tail Design.....	62
7.2.2. Structural Vertical Tail Design.....	64
7.5. Final Material Composition.....	69
8. Aeroelastic Analysis.....	69
9. Modal Analysis of the Aircraft.....	73
10. Stability Analysis.....	73
10.1. Longitudinal Static Stability.....	73
10.2. Lateral-Directional Static Stability.....	75
10.3. Longitudinal Dynamic Stability.....	76
10.4. Lateral-Directional Dynamic Stability.....	77
11. Center of Gravity.....	78
12. Subsystem Selections.....	80
12.1. Electric.....	80
12.2. Hydraulic.....	80
12.3. Fuel.....	81
12.4. Control.....	82
13. Landing Gear.....	84
13.1. Main landing gear.....	84
13.2. Nose landing gear.....	85



14. Interior Design.....	85
14.1. Thermal & Acoustic Insulation.....	87
14.2. Alternative Cabin Options .....	88
15. Geometric Configurations .....	89
16. Cost Analysis.....	91
16.1. Development and Production Costs .....	91
16.2. Operational Cost .....	94
17. Conclusions .....	96
18. Bibliography .....	97



## 1. Introduction

The study of fully or partially electric aircraft has been the subject of discussion between researchers and engineers at universities and the aeronautics industry over the last years. The need to develop ever more efficient and greener aircraft leads to the motivation to expand technologies and move toward previously unfeasible concepts.

Currently, most General Aviation aircraft typically use internal combustion engines (ICE) as a power source. These engines burn fossil fuels with high energy densities, making this type of raw material very advantageous for aviation. However, they are highly polluting, since their burning generates the production of carbon dioxide (CO<sub>2</sub>), which is the main responsible gas for global warming. The Air Transport Action Group (ATAG) points out that 2% of anthropometric carbon dioxide emissions come from aviation, and this number only tends to increase along with the number of aircraft in operation [1,2]. Under those circumstances, several targets have been defined in Vision 2020 and AGAPE 2020 for the next few years [3].

Besides the problem of emissions and pollution, the amount of fossil fuels available in the world is limited. Even not knowing about its availability and scarcity in the future, the fossil fuel prices themselves tend to increase in the coming decades due to the fast-growing worldwide energy demands and the uncertain political situation in the Middle East [4].

Thereby, all the situations mentioned above lead to consider and rethink in alternative ways of the power supply. Thus, the introduction of electric propulsion systems has been a great option. First of all, batteries can be used as a power source instead of conventional fuels. However, the battery use itself brings challenges such as the weight on board and its specific energy. Regarding the first one, aircraft are very sensitive when it comes to weight because as it increases on board, the available payload diminishes. Regarding the second one, the batteries currently have low specific energy when compared to high specific energy of conventional fuels. However, studies have shown great results for batteries in the future. Lithium-air batteries may show an impressive theoretical specific energy of 11,680 Wh/kg [5]. But in more realistic numbers, Zn-O<sub>2</sub> batteries with specific energy of 400 Wh/kg in 2025 are expected [6]. It is also worth remembering the challenge related to the international aviation regulations, which require that the minimum level of safety compared to the batteries be guaranteed.

Moreover, engines have a lower efficiency and power-to-weight ratio when compared to electric motors [7]. Hence, hybrid-electric systems are proposed to balance the advantages of both engine and motor systems, improving



the performance. Such systems have potential advantages including low fuel costs, lower vibrations, lower pollution, and reduced noise.

After all, it is not an easy task to balance all these interests and to develop a wholly or partially electric propulsion system, but it is of great importance and necessity to carry on the study and improvement of physical limitations, fulfilling the requirements and guidelines for the future.

Along those lines, when designing an aircraft, it is important to seek the best aerodynamic efficiency, good stability control, lower associated weight, better aeroelastic behavior, and ease of manufacturing. In this work, it is done a conceptual design of two hybrid-electric aircraft whose design requirements were determined through a Request for Proposal (RFP) published by the committees of the annual design competition sponsored by The American Institute of Aeronautics and Astronautics (AIAA).

The initial characteristics and geometries of a conventional aircraft were estimated through the study of historical trends. Then, the hybridization characteristics were evaluated using the series architecture, which affects mainly the range equations and the definition of the propulsive system elements that better fit the project, e.g., the internal combustion engine and batteries. To explore the multidisciplinary characteristics of the aircraft development, it was implemented an optimization based on a genetic algorithm fully integrated with an aerodynamic module with performance and stability constraints, searching for the best values of the geometrical design variables.

## **2. Design Requirements and Proposals**

For the year 2017-2018, the AIAA Request for Proposal (RFP) is for the design of two-member Hybrid-Electric General Aviation Aircraft family, one for 4 passengers and another one for 6 passengers. The year entry-into-service (YEIS) is 2028 for a 4-seat model with 1000 nmi of range and 2030 for the 6-seat model with 750 nmi of range. The intent is to have energy storage for takeoff, climb, go-around and emergencies via batteries and electric motors with an engine providing additional power and/or direct propulsion. Moreover, the airframe and propulsion system commonality, by weight, between the 4-seat and 6-seat variant should be 75% or greater of the 4-seater's empty weight.

The other requirements are presented in Tables 1, 2 and 3.



**Table 1: General requirements for both aircraft.**

<b>General Requirements</b>	Passenger/pilot weight of 190 lb
	Baggage weight per passenger/passenger of 30 lb and volume of at least 4 cubic feet per passenger
	Capable of taking off and landing from different runways (dirt, grass, metal mat, gravel, asphalt, and concrete)
	Takeoff, and landing performance should also be shown at 5,000 ft above mean sea level (ISA + 18 deg F) as well as for grass & concrete fields at sea level (ISA + 18 deg F)
	Minimum cruise speed of 174 knots & Target cruise speed: 200 knots or greater
	Capable of VFR and IFR flight with an autopilot
	Meets applicable certification rules in FAA 14 CFR Part 23
	Use of engine(s) and electric motor(s) that will be in service by 2028 and document battery energy and power density assumptions based on reasonable technology trends
	Show airframe and propulsion system commonality of at least 75% between the 4-seater and 6-seater by weight
	Show the emergency range to get to an alternate airport at the maximum feasible weight from an engine failure at 5000 ft AGL (ISA + 18 deg F) with electric power from batteries alone for both the 4- and 6-seat variants
	Provide systems and avionics architecture that could enable autonomous flight; otherwise, provide a market justification for choosing to either provide or omit this capability
	Meet 14 CFR 23.67 Climb: One engine inoperative requirements with either propulsion type inoperative if it will be treated as a twin-engine airplane

**Table 2: Design requirements for the aircraft of 4 passengers.**

<b>4-Seat Variant</b>	Crew: 1 pilot + 3 passengers
	1000 nmi design range mission with IFR reserves
	Maximum takeoff and landing field lengths of 1,500' over a 50' obstacle to a runway with dry pavement (sea level ISA + 18oF day)
	Initial climb rate at sea level (ISA+ 18oF) at least 1500 fpm with both electric and fossil fuel propulsion operating

**Table 3 - Design requirements for the aircraft of 6 passengers.**

<b>6-Seat Variant</b>	Crew: 1 pilot + 5 passengers
	750 nmi design range mission with IFR reserves
	Maximum takeoff and landing field lengths of 1,800 ft over a 50 ft obstacle to a runway with dry pavement (sea level ISA + 18oF day)
	Initial climb rate at sea level (ISA + 18 deg F) at least 1300 fpm with both electric and fossil fuel propulsion operating



### 3. Market Research

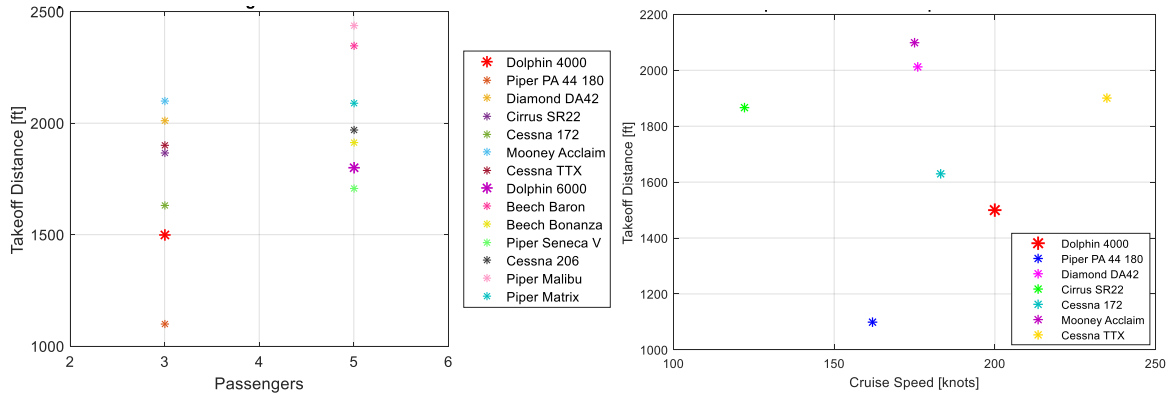
For everyone that loves airplanes, the biggest dream is to build one that emits noise as close to zero as possible. In order to do that, the solution that first come up to mind is a full electric power system, where the noise would be reduced, along with the fuel consumption and air pollution. However, the weight of the set of batteries and generator is so high that the aircraft would be stuck at the ground. Therefore, how could be possible to reduce noise, fuel consumption and air pollution on an aircraft? The answer is simple: hybrid propulsion.

The hybrid propulsion combines the power of electric and conventional engines, this way “*a plane might taxi to the runway on electricity. During high-demand phases of flight such as takeoff and climb, it could supplement that with energy from a turbine generator to provide lots of power without lots of noise. Once at altitude, the plane could loaf along with just the generator driving electric fans, diverting excess power back to recharge onboard batteries. Then, the plane could descend and land again as a quiet electric*”[8].

This reality is not as far away as it looks. According to Engadget[9], Airbus, Rolls-Royce and Siemens are partnering on a hybrid-electric aircraft prototype, the E-Fan X, that will prove the mixture of conventional and electric engines will work. The demonstrator will modify a BAe 146 by replacing one of its gas turbine engines with a 2MW electric motor, followed by a second if everything goes smoothly. It is currently slated to fly sometime in 2020.

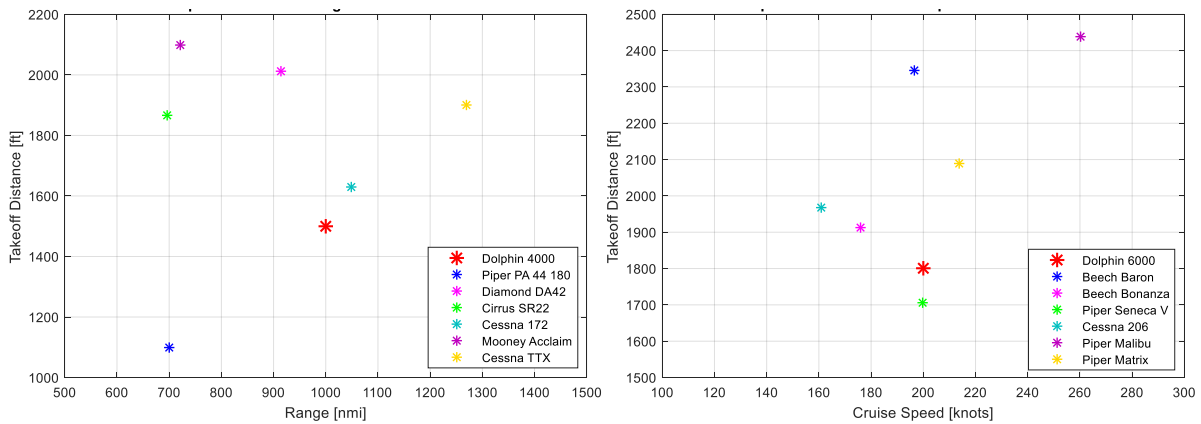
The aircraft project proposed here would compete with the airplanes in the general aviation category, such as Piper PA 44 180, Diamond DA42, Cirrus SR-22, Cessna 172, Mooney Acclaim and Cessna TTX for the 4PAX aircraft (Dolphin 4000) and Beechcraft Baron, Beechcraft Bonanza, Piper Seneca, Cessna 206, Piper Malibu and Piper MATRIX for the 6PAX aircraft (Dolphin 6000).

Figure 1 shows the comparison of takeoff distance between the 4 and 6 seats aircraft. As one can see, both aircraft of the spec have shorter takeoff distance than most of the competitors, which turns possible to takeoff from smaller runways. Figure 1 also shows the comparison of cruise speed and takeoff distance between the 4 seats aircraft. As shown, the cruise speed from the spec is higher than most of the competitors, except for the Cessna TTX. However, the takeoff distance is shorter, which is an advantage over Cessna TTX.



**Figure 1: Passengers count (on the left) and cruise speed (on the right) vs takeoff distance.**

Figure 2 shows the comparison of range and takeoff distance between the 4 seats aircraft. As one can see, the range proposed by the spec is greater than most of the competitors. Figure 2 also shows the comparison of cruise speed and takeoff distance between the 6 seats aircraft. As presented, the cruise speed proposed by the AIAA design requirements is among the competitors' average.



**Figure 2: Range (on the left) and cruise speed (on the right) vs takeoff distance.**

#### 4. Conceptual Design

This work deals with the design of two hybrid-electric aircraft: one for four passengers (4PAX) and the other for six passengers (6PAX). Both aircraft are expected to have 75% or greater of communality. Therefore, the first aircraft to be designed was the 4PAX one, since the AIAA specifications require shorter field lengths for takeoff and landing, a higher rate of climb and a more significant range. Thus, after having that aircraft in hands, it is easier to adapt it to the 6PAX configuration, changing the empennage, but keeping the same wing.

The design of this hybrid-electric aircraft was obtained using the procedures and theories presented by Venson [10-15], and only the conceptual and preliminary design phases were evaluated.



#### 4.1. Initial Design Estimate

First of all, in the conceptual design of the aircraft, several trend tables were used to obtain some initial estimates. But for that, it was necessary to assign some initial configurations to the aircraft. Thus, four main configurations were assumed: twin-engine with T-tail, twin-engine with conventional tail, single-engine with T-tail, and single-engine with conventional tail.

The algorithm used to estimate the design of the aforementioned aircraft considers several coefficients and characteristic values of conventional aircraft presented in historical tables present in the literatures [10-15]. Most of them are represented by a function defined by:

$$f(a, W_0, c) = aW_0^c \quad (1)$$

where  $f(a, W_0, c)$  represents the characteristic to be calculated such as wetted area ( $S_{wet}$ ),  $a$  and  $c$  are constants that depend on the type of aircraft under analysis, and  $W_0$  is the gross weight estimate of the aircraft, which is iterated throughout the project.

This process of iteration and updating of the aircraft weight is performed considering the weight variation and performance during the phases of flight which the fuel consumption is higher: cruise and loiter. In [14,15] the weight ratios per phase are introduced, setting a correlation between them during the aircraft mission. The simplified scheme of iteration flow is presented in Figure 3 (first iteration) and Figure 4 (other iterations).

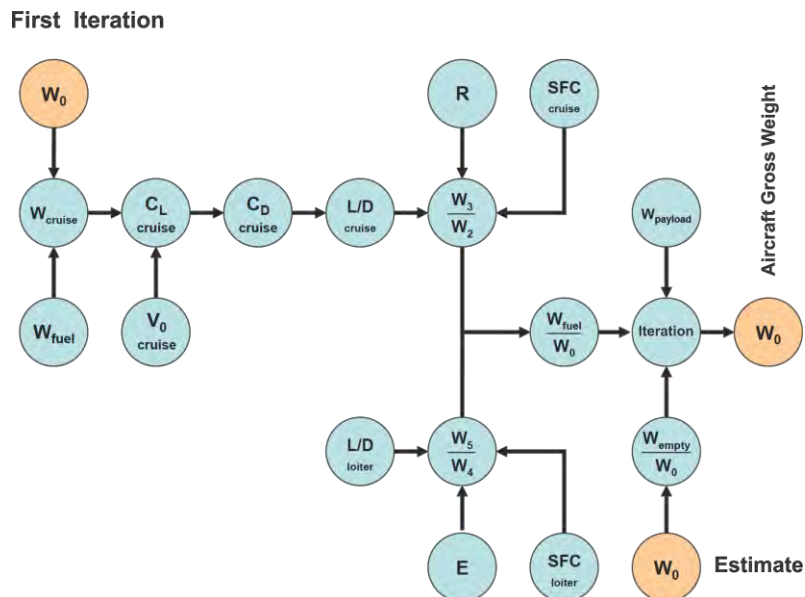


Figure 3: First iteration for aircraft gross weight estimate. Source: Venson [12].

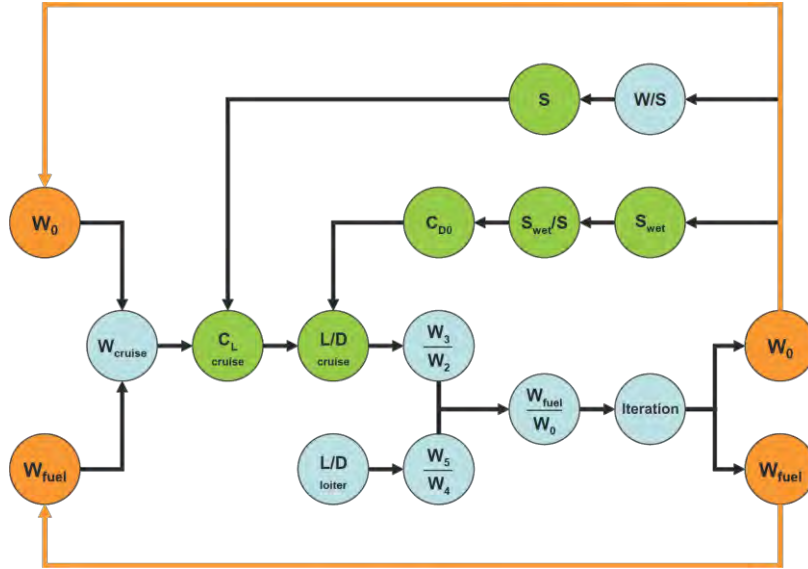


Figure 4: Other iterations for aircraft gross weight estimate. Source: Venson [12].

Hence, the values used as respective inputs for each aircraft in the algorithm are presented in Table 4. It is worth remembering that these values come from historical tables mentioned above.

Table 4: Algorithm inputs for each aircraft configuration.

	Twin-engine aircraft with T-tail	Twin-engine aircraft with conventional tail	Single engine aircraft with T-tail	Single engine aircraft with conventional tail
$AR_W$	7.8	7.8	7.2	7.2
$\lambda_W$	0.75	0.75	0.75	0.75
$\Lambda_W$ [°]	22	22	22	22
$e_w$	0.82	0.82	0.83	0.83
$C_{L_{max}}$	1.7	1.7	1.7	1.7
$AR_{HT}$	4.4	4.3	4.1	39
$\lambda_{HT}$	0.5	0.5	0.5	0.5
$V_{HT}$	0.96	0.84	0.60	0.45
$AR_{VT}$	1.0	1.4	1.2	1.5
$\lambda_{VT}$	0.4	0.4	0.5	0.5
$V_{VT}$	0.071	0.050	0.030	0.030
$a_{S_{wet}}$	0.2933	0.2933	0.6762	0.6762
$c_{S_{wet}}$	0.5632	0.5632	0.4884	0.4884
$a_{W_0}$	766	0.766	0.892	0.892



$c_{W_0}$	-0.20	-0.020	-0.047	-0.047
$a_{W/S}$	1.512	1.512	0.408	0.408
$c_{W/S}$	0.664	0.664	0.804	0.804
$a_T$	0.0116	0.0116	0.0116	0.0116
$c_T$	0.4789	0.4789	0.4789	0.4789
$S_{Wet}/S_{Ref}$	4.0	4.0	4.5	4.5
$C_{fe}$	0.055	0.055	0.055	0.055
$W_1/W_0$	0.984	0.984	0.990	0.990
$W_2/W_1$	0.990	0.990	0.992	0.992
$W_4/W_3$	0.992	0.992	0.993	0.993
$W_6/W_5$	0.992	0.992	0.993	0.993
$a_{D_{TO}}$	9.68	9.68	8.23	8.23
$a_{D_{LND}}$	1.463	1.463	1.524	1.524
$a_{fuselage}$	0.4088	0.4088	0.4088	0.4088
$c_{fuselage}$	0.3140	0.3140	0.3140	0.3140
$x_L/d$	8.3	8.3	8.3	8.3
$x_N/d$	1.3	1.3	1.3	1.3
$x_C/d$	0.56	0.56	0.56	0.56
$x_T/d$	2.3	2.3	2.3	2.3
$R_x$	0.34	0.34	0.25	0.25
$R_y$	0.38	0.38	0.38	0.38
$R_z$	0.39	0.39	0.39	0.39
$C_{L_{clean}}$	1.6	1.6	1.5	1.5
$C_{L_{TO}}$	1.9	1.9	1.8	1.8
$C_{L_{LND}}$	2.3	2.3	2.0	2.0
Aileron wing Ratio	0.05	0.05	0.07	0.07
Elevator Tail Ratio	0.44	0.44	0.41	0.41
Rudder Tail Ratio	0.38	0.38	0.36	0.36
Main gear at mac	0.52	0.52	0.50	0.50
Nose gear at length	0.17	0.17	0.13	0.13
Inner engine span	0.34	0.34	0.30	0.30



Besides the inputs from Table 4, the algorithm needed an engine to be considered during the performance analysis. Since both aircraft were going to be hybrid, the strategy used here was to get started choosing an electric motor instead of a conventional engine. Searching for commercial and available electric motors, the Siemens' SP260D was chosen due to its application in electric aircraft, such as the Extra 330LE, also developed by Siemens. Moreover, this electric motor provides 260 kW along with a significant efficiency of 95%, which would be sufficient for both aircraft, and weighs only 50 kg, saving a lot of weight. Further details and technical information are available in [16].



Figure 5: Electric motor SP260D (on the left) and Siemens Extra 330LE (on the right). Source: Endless Sphere.

Thus, after running the algorithm, it was released the following outputs for each aircraft, shown in Table 5.

Table 5: Algorithm outputs for each aircraft configuration.

	Twin-engine aircraft with T-tail	Twin-engine aircraft with conventional tail	Single engine aircraft with T-tail	Single engine aircraft with conventional tail
MTOW [kg]	1880.10	1880.10	1466.20	1466.20
Fuel Weight [kg]	297.60	297.60	233.07	233.07
Empty Weight [kg]	1183.30	1183.30	833.97	833.97
Payload Weight [kg]	399.20	399.20	399.20	399.20
Structural Weight [kg]	487.97	487.19	433.03	433.14
$b_w$ [m]	11.83	11.83	10.74	10.74
$c_{r_w}$ [m]	1.73	1.73	1.70	1.70
$c_{mac_w}$ [m]	1.53	1.53	1.50	1.50
$y_{mac_w}$ [m]	2.82	2.82	2.56	2.56



$S_w$ [m <sup>2</sup> ]	17.94	17.94	16.01	16.01
$C_{L_{cruise}}$	0.26	0.26	0.22	0.22
$CD_0$	0.02	0.02	0.02	0.02
$k_2$	0.05	0.05	0.05	0.05
$x_w$ [m]	2.65	2.72	3.21	3.10
Service Ceiling [ft]	12000.00	12000.00	12000.00	12000.00
Mach (cruise)	0.28	0.28	0.28	0.28
$V_{stall}$ [m/s]	31.96	31.96	29.88	29.88
$W_1/W_0$	0.98	0.98	0.99	0.99
$W_2/W_1$	0.99	0.99	0.99	0.99
$W_3/W_2$	0.89	0.89	0.89	0.89
$W_4/W_3$	0.99	0.99	0.99	0.99
$W_5/W_4$	0.98	0.98	0.98	0.98
$W_6/W_5$	0.99	0.99	0.99	0.99
Takeoff Distance [m]	268.05	268.05	290.45	290.45
Landing Distance [m]	747.39	747.39	680.47	680.47
Range [km]	1228.00	1228.00	1094.60	1094.60
ROC [ft/min]	2483.90	2483.90	1377.20	1377.20
$l_{fuselage}$ [m]	8.52	8.52	8.52	8.52
$d_{fuselage}$ [m]	1.70	1.70	1.70	1.70
$S_{HT}$ [m <sup>2</sup> ]	7.71	6.75	3.53	3.53
$c_{r_{HT}}$ [m]	1.77	1.67	1.16	1.31
$b_{HT}$ [m]	5.83	5.39	3.80	3.71
$c_{mac_{HT}}$ [m]	1.37	1.30	0.95	1.00
$x_{HT}$ [m]	6.75	6.85	7.36	7.21
$S_{VT}$ [m <sup>2</sup> ]	4.42	3.11	1.51	1.51
$c_{i_{VT}}$ [m]	3.00	2.13	1.58	1.39
$b_{VT}$ [m]	2.10	2.09	0.87	0.87
$c_{mac_{VT}}$ [m]	2.23	1.58	1.74	1.76



$x_{VT}$ [m]	5.52	6.39	6.94	7.13
$x_{Landing.gear}$ [m]	4.43	4.43	4.26	4.26
$y_{engine}$ [m]	1.45	1.45	0.00	0.00
$I_{xx}$ [kg·m <sup>2</sup> ]	7602.20	7602.20	2640.20	2640.20
$I_{yy}$ [kg·m <sup>2</sup> ]	4926.80	4926.80	3842.30	3842.30
$I_{zz}$ [kg·m <sup>2</sup> ]	393790.00	393790.00	213500.00	213500.00
$x_{CG}$ (empty aircraft) [m]	3.81	3.82	4.15	4.14
$x_{CG}$ (loaded aircraft) [m]	3.67	3.68	3.89	3.88
Sale Price [US\$]	1062300.00	1061200.00	893590.00	893750.00
Operating Costs per Year [US\$/year]	35092.00	35092.00	33082.00	33082.00
Operating Costs per Hour [US\$/hr]	116.97	116.97	116.74	116.74

Thus, gathering the results from Table 5, the following aircraft configurations were obtained and are presented in Figure 6.

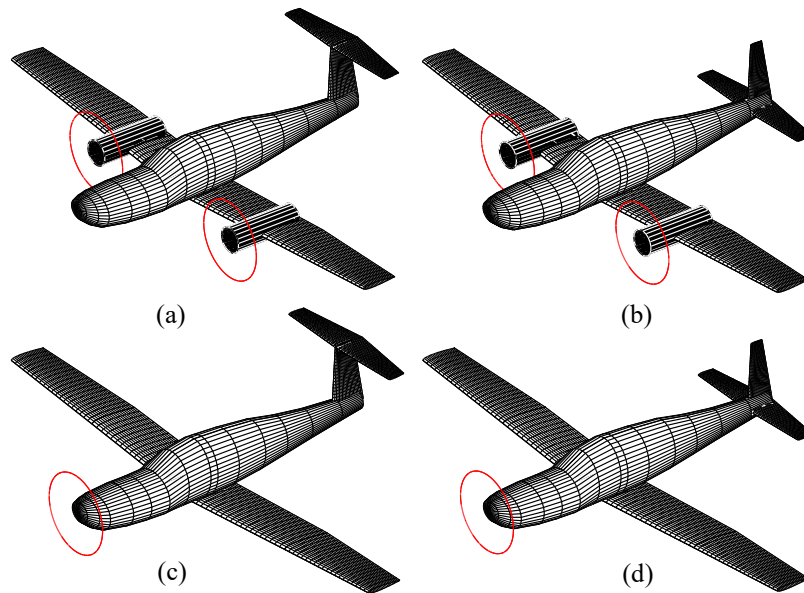


**Figure 6: Sketch of the 4 aircraft released by the initial concept design estimate: (a) twin-engine with T-tail, (b) twin-engine with conventional tail, (c) single engine with T-tail, (d) single engine with conventional tail.**

Analyzing the AIAA design requirements with the results from Table 5, the aircraft that best satisfies the specifications are the single engine aircraft, either with conventional or T-tail. In both cases, the single engine provides



sufficient power for the aircraft to fly and reaches the required performance. So, it was easy to choose only one engine. But for the tail, it goes beyond that.

The design of an empennage for any aircraft is extremely important, since it affects the aircraft mass and center of gravity, i.e., the static and dynamic stability. Then, it is necessary to consider the effects of both empennages arrangement. The conventional tail provides appropriate stability and control, and also leads to the most lightweight construction in most cases, so much so that approximately 70% of aircraft are fitted with it [17]. Moreover, for this configuration, the stabilizer trim is relatively less complex and the vertical tail is usually larger. However, engines cannot be coupled to the rear of the aircraft, what is useful for static stability. Furthermore, spin characteristics can be bad in the case of conventional tail due to the blanketing of the vertical tail, in addition to the downwash of the wing being relatively large in the area of the horizontal tail.

On the other hand, the T-tail is heavier than the conventional tail because the vertical tail has to support the horizontal tail. However, the T-tail has advantages that partly compensate this important disadvantage (weight). Because of the end plate effect, the vertical tail can be smaller. In addition, the horizontal tail is more effective because it is positioned out of the airflow behind the wing and is subjected to less downwash. Therefore, it can be smaller. For the same reason, the horizontal tail is also subject to less tail buffeting. As the T-tail creates space at aircraft's rear, there is enough space to fix the engines, improving static stability.

Hence, since the aircraft is going to have a lightweight engine at the nose, considering the information above and aiming an easier structural analysis, the conventional empennage was chosen for this aircraft design.

Thus, at this point an overall configuration for the aircraft had been defined. However, it was necessary to improve and refine the aircraft adjusting equations and algorithms for it to become a hybrid-electric one. In other words, the performance equations had to be solved using the hybrid-electric architectures, what would imply in new results and configurations. But, first of all, the propulsion system architecture had to be determined.

#### **4.2. Hybrid-Electric Aircraft Design**

Several papers indicate the parallel architecture as the most appropriate arrangement for large aircraft due to the lower weight associated, since the batteries only feed an electric generator, which helps the main shaft of a turbojet engine, for example. However, the aircraft designed here will be small, carrying four and six passengers, what makes



the architecture simpler. Therefore, the series-architecture was chosen for the aircraft, since the engine is already an electric-motor, requiring only electric power to move it. Figure 7 depicts the propulsion system architecture proposed.

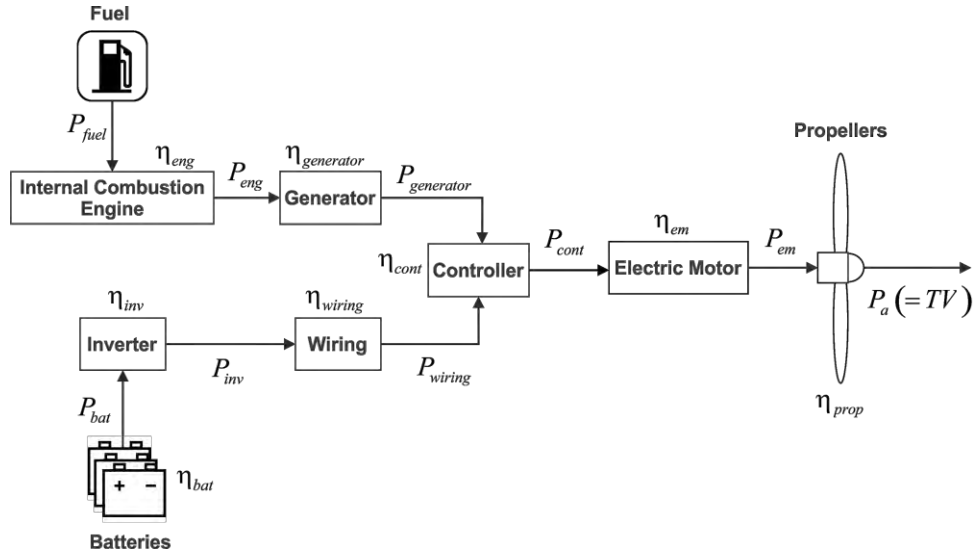


**Figure 7: Series-architecture used in both 4PAX and 6 PAX aircraft.**

In the analysis of the participation of each of the energy sources (energy internal combustion (ICE) and batteries), it was considered that ICE would be maintained at its optimum rotation speed and would provide a "constant" power during takeoff, climb and cruise phases. In this way, as the aircraft requires more power than ICE provides, the batteries would be responsible for supplying the remainder of the electrical power, ensuring the operation of the electric motor, which is located on the nose of the aircraft. In the loiter and landing phases, the ICE would no longer be used. Thus, the motor is fully powered by the batteries. For the architecture above, all efficiencies were assumed base on literatures and papers, as presented in Table 6.

**Table 6: Efficiencies for the hybrid-electric propulsive system.**

Efficiency	Value
$\eta_{bat}$	90% <sup>[18]</sup>
$\eta_{inv}$	95% <sup>[19]</sup>
$\eta_{wiring}$	97% <sup>[20]</sup>
$\eta_{cont}$	99% <sup>[21]</sup>
$\eta_{eng}$	60% <sup>[22]</sup>
$\eta_{generator}$	95% <sup>[23]</sup>
$\eta_{em}$	95% <sup>[23]</sup>
$\eta_{prop}$	85% <sup>[24]</sup>



Now it is necessary to come up with the new performance analysis. First, the classic Bréguet's range is formulated for a conventional fuel powered aircraft at zero wind conditions, and thrust vector parallel to the airspeed vector, which defines the following:

$$R = \int_{W_{final}}^{W_{start}} \frac{V}{c_T} \frac{C_L}{C_D} \frac{1}{W} dW \quad (2)$$

where  $c_T$  means the specific fuel consumption.

The solution to the integral depends on the flying strategy used (e.g., gradual climb at a constant airspeed and angle of attack) and the models used to represent the propulsion system and the aerodynamic characteristics. Solutions to the most common flying strategies can be found in many standard textbooks on aircraft performance. But, fundamentally, these solutions use the idea that weight changes gradually throughout the flight. Therefore, the range equation cannot be applied to the hybrid aircraft to be designed here, which uses an electric system (batteries) as energy supply. Thus, Voskuijl presents in [25] a new formulation for the range equation relating the energy stored to the consumption of a hybrid aircraft with parallel architecture. Since the architecture of both aircraft under analysis here is going to be in series, the formulation is reevaluated for the scheme available in Figure 7, which results in the following equation:

$$R = \frac{\eta_{cont} \eta_{em} \eta_{prop}}{g \left( \frac{c_p}{\eta_{generator}} \frac{H_{fuel}}{g} (1-S) + \frac{S}{\eta_{inv} \eta_{wiring}} \right)} \frac{C_L}{C_D} \frac{H_{battery} H_{fuel}}{\psi H_{fuel} + (1-\psi) H_{battery}} \ln \left( \frac{(\psi H_{fuel} + (1-\psi) H_{battery}) g E_{start} + W_{empty} + W_{payload}}{H_{battery} H_{fuel}} \frac{H_{battery} H_{fuel}}{W_{empty} + W_{payload}} \right) \quad (3)$$

### 4.3. Design Assumptions

Before finishing the concept design, some aspects were added and settled for the development of both aircraft (4PAX and 6PAX), such as: typical aircraft mission profile, the batteries and an internal combustion engine (ICE) for the hybrid system.



### 4.3.1. Typical Aircraft Mission Profile

Based on historical data, FAR – Part 23 and AIAA specifications, some mission characteristics were chosen and are presented in Table 7. The flight level FL120 was chosen to avoid any pressurization issues, since the regulation 14 CFR 91 requires supplemental oxygen system for aircraft flying over FL120.

Also, the minimum cruise speed required by the AIAA is 174 knots. Thus, the chosen cruise speed for this project was chosen to be 185 knots, since similar aircraft, such as the Diamond DA42, usually fly around this velocity during cruise. Besides, the rate of climb of 1500 and 1300 fpm were kept the same as specified, and the rate of descent were assumed 900 fpm from trends in [26]. The ranges for both aircraft are also fixed by AIAA and the estimate of endurance in cruise is obtained dividing these ranges by the respective cruise speed. Additionally, the total endurance is an estimate of the time to reach the AIAA requirements (climb and cruise), the assumptions (descent) and the FAR Sec. 125 regulations (taxi, takeoff, approach, loiter and landing).

**Table 7: Chosen mission characteristics for both aircraft design.**

Mission Characteristics	4PAX	6PAX
Service ceiling [ft]	12000	12000
Cruise speed [knots]	185	185
Rate of climb [ft/min]	1500	1300
Rate of descent [ft/min]	900	900
Range in cruise [km]	1860	1340
Endurance in cruise [hr]	5.43	3.9
Total endurance [hr]	7.22	5.79

Thus, evaluating the time spent during all phases of flight, reaching the parameters in Table 7, typical flight mission for the 4PAX and 6PAX aircraft regarding altitude and flight time are shown in Figures 8 and 9, respectively. The percentage values are related to the total time spent on the mission, which was calculated as it follows.

For 4PAX, for example, during taxi and takeoff, it was considered that the aircraft usually spend a time of 15 minutes. Next, climbing from 0 ft to 12000 ft at a rate of 1500 fpm would take 8 minutes to reach that altitude. For cruise phase, and flying at 185 knots, it would take about 5 hours to reach the specified range of 1860 km. Moreover, it was considered a descent and approach in 50 minutes, and 15 minutes for landing. Summing up all those values, the entire mission would take about 400 minutes. Therefore, it was estimated the percentage values of Figures 8 and 8.

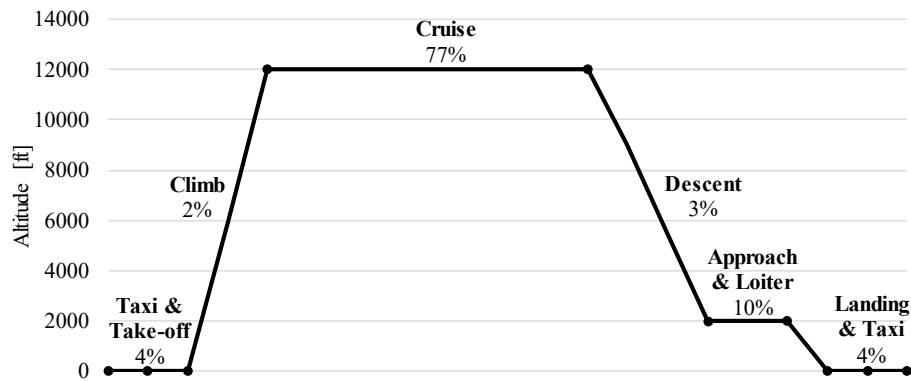


Figure 8: 4PAX aircraft typical flight mission.

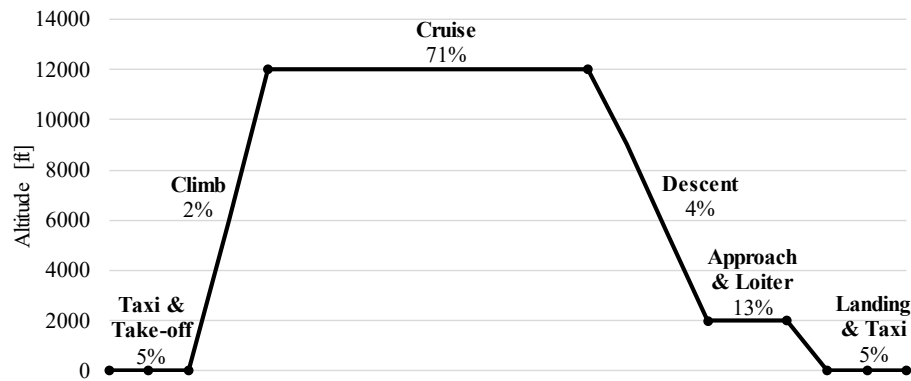


Figure 9: 6PAX aircraft typical flight mission.

#### 4.3.2. Battery Design

The choice of batteries to be used in the aircraft hybrid system was based on the estimates proposed by Hepperle [42] and Girishkumar [43] for the technology available in 2025, which are shown in Table 8. The theoretical specific energy values are not truly feasible in actual applications. The amount of energy that the batteries are able to provide are much less than the expected. In other words, there is an efficiency associated to these chemical reactions involved. Thus, when choosing a battery system, it is very important to consider these effects.

Table 8: Specific energy density of current and future chemical battery systems [27].

System	Theoretical specific energy density	Actual battery energy density expected in 2025
Li-Ion	390 Wh/kg	250 Wh/kg
Zn-O <sub>2</sub>	1090 Wh/kg	400-500 Wh/kg
Li-S	2570 Wh/kg	500-1250 Wh/kg
Li-O <sub>2</sub>	3500 Wh/kg	800-1750 Wh/kg



Later, it was performed an assessment of the feasibility of using such batteries in both aircraft in 2028, as required by AIAA specifications. According to Bruce [28] and Ji [29], the researches with Li-S and Li-O<sub>2</sub> batteries are in full development and implementation. However, the reliability and safety of these types of batteries are still unknown, which makes them unviable for aerospace applications expected in 2028.

On the other hand, Zn-O<sub>2</sub> batteries have been developed since the 1960s and already have medical and telecommunication applications [30]. In addition, companies such as Teck Cominco Metals Ltd.<sup>®</sup> and Tesla Motors, Inc.<sup>®</sup> hold patents for the application of this type of battery in the automotive industry [31,32]. Thus, due to its energy density (higher than for Li-Ion), maturity of their behavior and safety, which is crucial for aerospace applications, the type of battery chosen for both aircraft was the Zn-O<sub>2</sub>. Using a more conservative approach, the energy density that will be considered for this battery will be 400 Wh/kg.

#### 4.3.2. Internal Combustion Engine (ICE)

To choose an internal combustion engine (ICE) that better fits the aircraft selected in Section 4.1, it was compared the viability of two turbo-engines. The first one is a 4-cylinder engine with rated power below the power required for cruising (145 kW) and climb (215 kW), while the second one is a 6-cylinder engine with power output greater than those required in both cruise and climb conditions. Table 9 shows the main characteristics of each ICE.

**Table 9: Main characteristics of Austro AE330 and Lycoming IO-580 engines.**

Characteristic	Austro AE330	Lycoming IO-580
Number of Cylinders	4	6
Rated Power [kW]	134	220
Mass [kg]	186	201
Dimensions [m]	0.74 x 0.85 x 0.57	0.99 x 0.87 x 0.53
Fuel consumption [kg/hr]	31.20	47.68

The degree of hybridization was considered so that the ICE used its maximum capacity during taxi & takeoff, climb and cruise phases. For the remaining phases, aiming to reduce noise during approach, loiter and landing, the ICE would stay in idle, and all the power required for that phase would be supplied by the batteries.

To estimate the amount of battery required in each phase of flight, it was considered the typical mission from Figure 8. Thus, during takeoff + climb phase, the aircraft would require from the electric motor about 228 kW of power to reach the rate of climb specified. To provide that 228 kW to the electric motor, the ICE Austro AE330 would provide 134 kW, remaining 102 kW to be provided by the batteries, resulting in a degree-of-hybridization (S) of 0.4126, not



considering the efficiencies of the architecture. Considering a takeoff + climb of 8 minutes (i.e., 0.13 hr) and an energy density of 400 Wh/kg for the batteries, it would be necessary 33.15 kg of battery for that phase of flight. Since the fuel consumption of the ICE Austro AE330 is 31.20 kg/hr, for the same time spent, it would be necessary 4.06 kg of fuel. Similarly, the other phases of flight were evaluated.

Table 10 shows the comparison of the 4-cylinder engine with the proposed hybridization, and Table 11 shows a 6-cylinder engine with a higher power than required and without hybridization.

**Table 10: 4-cylinder engine with proposed hybridization.**

Phase of Flight	S (degree-of-hybridization)	Time [hr]	Battery Weight [kg]	Fuel Weight [kg]
Takeoff + Climb	0.4126	0.13	33.15	4.06
Cruise	0.1092	5.52	226.62	172.41
Loiter	1.0000	0.50	46.83	0.00
Descent + Landing	1.0000	0.22	20.81	0.00
TOTAL	-	6.37	327.41	176.47

**Table 11: 6-cylinder with higher power required and without hybridization.**

Phase of Flight	S (degree-of-hybridization)	Time [hr]	Battery Weight [kg]	Fuel Weight [kg]
Takeoff + Climb	0.0000	0.13	0.00	6.32
Cruise	0.0000	5.52	0.00	266.48
Loiter	0.0000	0.50	0.00	23.68
Descent + Landing	0.0000	0.22	0.00	10.52
TOTAL	-	6.37	0.00	307.01

Analyzing costs, the 4-cylinder engine has an estimated cost of US\$106.64 in fuel [33] and US\$25.84 for the total recharge of the batteries [34], resulting in a total cost of US\$132.48 per flight, while the 6-cylinder engine has a total cost of US\$185.42 per flight.

Therefore, there is a saving of US\$52.94 per flight when using the Austro AE330 engine. In addition, the 4-cylinder engine is 38 kg lighter and has a 27% lower volume than the 6-cylinder engine, which justifies its application in conjunction with the hybridization of the aircraft.

#### 4.4. Genetic Algorithm Implementation

In Section 4.1, it was estimated an initial definition for the main characteristics of both aircraft. Next, it was defined the hybrid architecture and its components. Now it comes up with the idea to implement an algorithm of



optimization to vary those characteristics and find better configurations for both aircraft, increasing efficiency and saving weight. Thus, after formulating the new range equation for hybrid-electric aircraft, an optimization algorithm was implemented in Matlab to find the best aircraft configuration.

The type of optimization implemented was based on the differential evolution algorithm proposed by Rainer Storn [35]. In this method, 300 generations were created, where each generation contained 10 members per population. However, because of the several iteration variables, the genetic algorithm requires too much processing, which generates a huge computational cost, spending many hours to reach the final result. In this case, for example, it took an average of 15 hours to end the optimization, which justifies the low value of 10 members per population.

The input variables for the objective function were generated based on the values of geometry, weight and performance from the results presented in Section 4.1. Table 12 shows the maximum and minimum values used in each optimization variable.

**Table 12: Maximum and minimum values for each optimization variable.**

<b>Parameter</b>	<b>Max</b>	<b>Min</b>
Takeoff Engine Power [kW]	200.000	260.000
Climb Engine Power [kW]	200.000	260.000
Wing position along the aircraft's longitudinal axis [m]	3.238	5.397
Wing span [m]	8.033	13.388
Wing root-chord [m]	1.313	2.188
Wing taper ratio	0.525	0.875
Wing swept angle [°]	0.000	10.000
Wing breaking-point [m]	1.339	2.231
Wing dihedral [°]	0.000	5.000
Wing incidence angle [°]	0.000	3.000
Wing twist [°]	0.000	3.000
Wing profile	1.000	5.000
Horizontal tail span [m]	1.134	1.890
Horizontal tail taper ratio	0.525	0.875
Horizontal tail root-chord [m]	0.794	1.324
Horizontal tail swept angle [°]	0.000	5.000
Horizontal tail profile	1.000	3.000
Vertical tail span [m]	1.126	1.876
Vertical tail taper ratio	0.525	0.875



Vertical tail root-chord [m]	0.883	1.472
Vertical tail swept angle [°]	0.000	5.000
Vertical tail profile	1.000	2.000
Fuel Weight [kg]	54.348	380.437

---

Thus, the genetic algorithm used these inputs to find the best configuration option for the aircraft, meeting the AIAA requirements and achieving a lower gross weight as optimization variable. Different airfoil profiles were used for the objective function to be used in the wings and empennage. All of them were also optimization variables:

- Wing: NACA 23010, NACA 23012, NACA 23015, NACA 23016 and NACA 63415;
- Horizontal Tail: NACA 0012, NACA 0009 and NACA 2412;
- Vertical Tail: NACA 0012 and NACA 0009.

For the trimming, aerodynamics and dynamics stability analyses, it was necessary to use a program to aid in the process. For this genetic algorithm, the chosen program was the AVL (Athena Vortex Lattice). An example of how the AVL deal with aircraft geometries is presented in Figure 10.

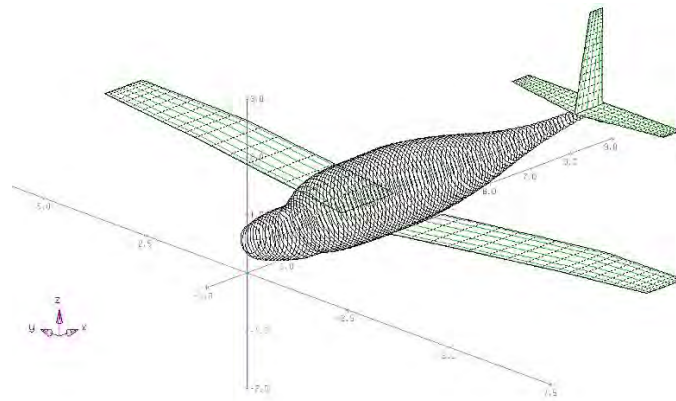


**Figure 10: 4PAX aircraft AVL model.**

Therefore, the AVL provides aerodynamics and stability results to the genetic algorithm. In addition, it is possible to calculate the performance characteristics using the hybridization ratios. So, it compares these values to the specified criteria shown in Table 13.

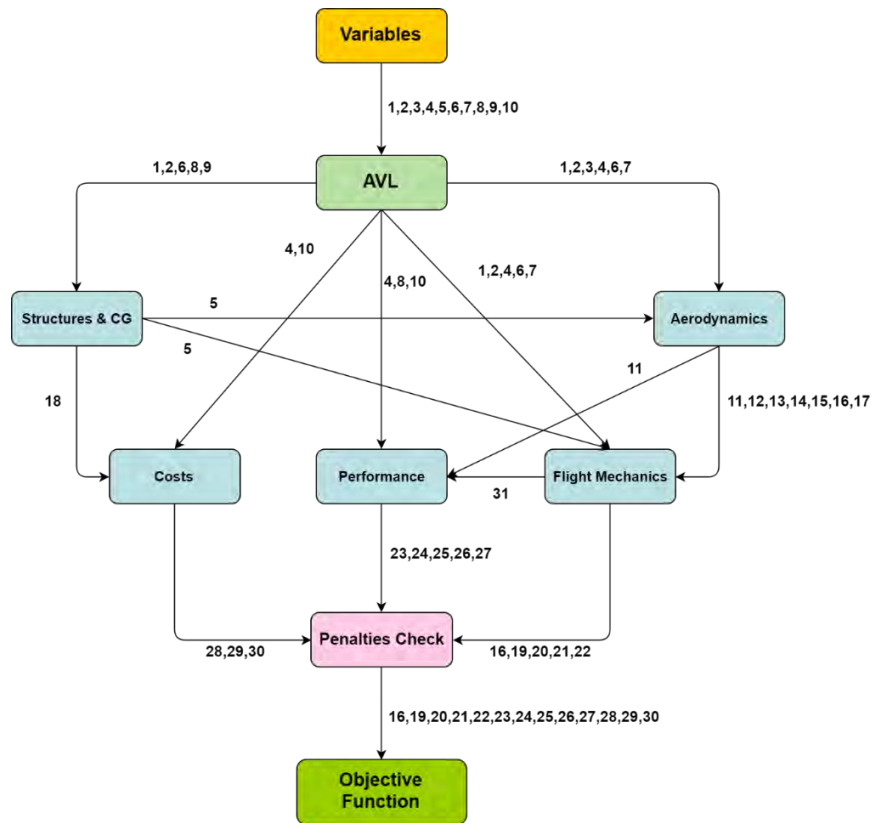
During the optimization, if the aircraft do not meet all the criteria presented, a penalty is added to an optimization variable. Thus, these aircraft with penalties are discarded over time by the objective function.

Figure 11 shows the flowchart used in the optimization process described above. The numbers in the process are associated to the variables available in Table 14.



**Table 13: Specified criteria for genetic algorithm.**

		4PAX		6PAX	
		Min	Max	Min	Max
Geometrical	$AR_W$	-	13	-	13
	$AR_{HT}$	-	7.5	-	7.5
	$AR_{VT}$	1.5	5.5	1.5	5.5
Performance	Takeoff Length [m]	-	457.20	-	548.64
	Landing Length [m]	-	457.20	-	548.64
	Rate of Climb [ft/min]	-	1500	-	1300
	Angle of Climb [°]	5	30	5	30
	Range [km]	1852	-	1389	-
	$E_{max}$	10	20	10	20
Stability	$C_{m\alpha}$	-	-0.40	-	-0.40
	Static Margin	10	40	10	40
	Trimmed Angle of Attack [°]	0	5	0	5
	Elevator Deflection for Trimmed Condition [°]	-10	10	-10	10
	$C_{n\beta}$	0.05	-	0.05	-
	$C_{l\beta}$	-	-0.04	-	-0.04



**Figure 11: Genetic algorithm flowchart.**



**Table 14: Variables used in the genetic algorithm and represented in Figure 11.**

Variable	Description
1	Wing and Empennage Positions
2	Wing, Empennage and Fuselage Dimensions
3	Wing and Empennage Sweep, Dihedral, Incidence, Twist Angles and Profiles
4	Sea Level Condition
5	CG Position
6	Flap and Control Surfaces Dimensions
7	Flap and Control Surfaces Positions
8	MTOW
9	Moment of Inertia
10	Engine Power/Consumption and Fuel Weight
11	Wing and Empennage $CL_\alpha$
12	Non-trimmed Drag Polar
13	Wing and Empennage $Cm_\alpha$
14	$dCl_\delta$ aileron and $dCl_\delta$ rudder
15	$dCn_\delta$ aileron and $dCn_\delta$ rudder
16	$Cn_\beta$ and $Cl_\beta$
17	$dCL_\delta$ elevator and $dCm_\delta$ elevator
18	Structural Weight
19	Full Aircraft $Cm_\alpha$
20	Empty and MTOW Static Margins
21	Longitudinal Trim Conditions
22	Lateral–Directional Trim Conditions
23	Range
24	Endurance
25	Rate of Climb
26	Takeoff and Landing Length
27	Service Ceiling
28	Sale Price
29	Operating Costs Per Year
30	Operating Costs Per Hour
31	Trimmed Drag Polar

Finally, the genetic algorithm released an optimized aircraft configuration, which satisfies all requirements for the 4PAX configuration. However, this aircraft had to be modified in order to better fit the 6PAX arrangement. A length of 0.75 m was added in the passenger cabin to accommodate the two extra passengers, in addition to the increase in payload. Thus, the optimizer was reshaped so that it provides just a new empennage (horizontal and vertical), since



the wing was assumed to be the same. Therefore, the final configurations for both aircraft generated by the genetic algorithm are presented in Table 15. The CATIA models for both configurations are shown in Figure 12.

Here it is possible to evaluate the commonality of both aircraft. Since they have the same wing, propulsion components (ICE, electric motor, batteries), and part of the fuselage, the commonality of by weight obtained is 96%, which minimizes the development, certification, and manufacturing costs a significant amount.

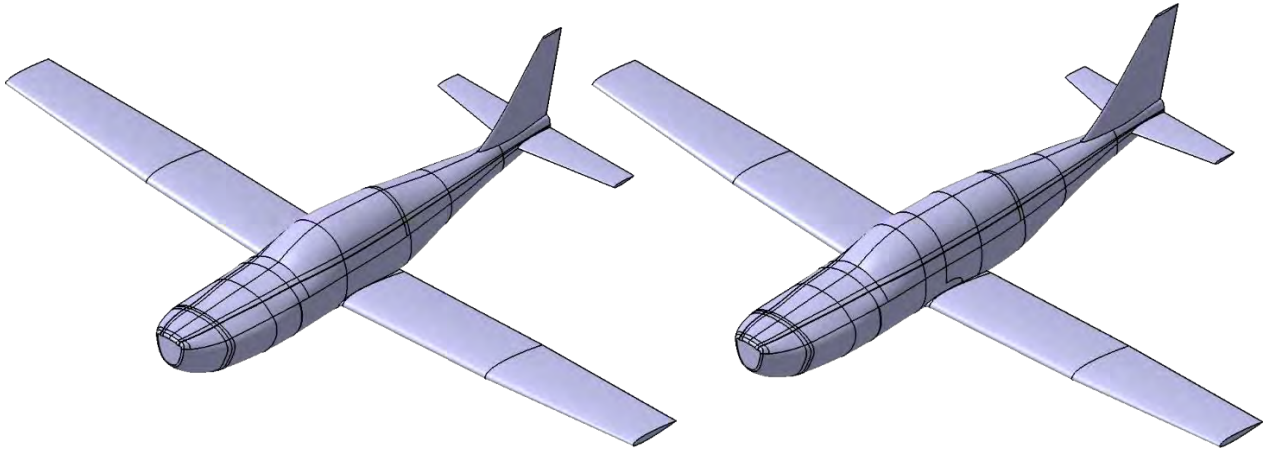


Figure 12: 4PAX aircraft CATIA model.

Table 15: Final optimized configurations for both hybrid aircraft.

		4PAX	6PAX
<b>Weight</b>	MTOW [kg]	1855.10	1966.20
	Fuel [kg]	176.57	130.63
	Empty [kg]	1279.30	1236.80
	Payload [kg]	399.20	598.80
	Structural [kg]	474.38	497.50
	TZFW [kg]	1713.80	1861.70
	Battery [kg]	370.63	309.71
<b>Wing</b>	$b_w$ [m]	13.38	13.38
	$c_{r_w}$ [m]	1.31	1.31
	$c_{mac_w}$ [m]	1.19	1.19
	$AR_w$	12.84	12.84
	$\lambda_w$	0.70	0.70
	$\Lambda_w$ [°]	0.080	0.080
	$S_w$ [m <sup>2</sup> ]	13.95	13.95
	$C_{L_{max}}$	1.51	1.51
	$C_{D_0}$	0.024	0.024
	$k_2$	0.046	0.046



	$x_w$ [m]	2.88	3.52
	Y-Position Break [m]	3.61	3.61
	$\Gamma_w$ [°]	4.70	4.70
	$i_w$ [°]	2.00	2.00
	$C_{L_{max}}$ with take-off flap	2.00	2.00
<b>Performance</b>	Maximum Ceiling [m]	5486.40	5486.40
	$V_{cruise}$ [m/s]	94.14	94.14
	$M_{cruise}$	0.28	0.28
	$T / W$	0.11	0.10
	$V_{stall}$ [m/s]	33.20	34.18
	Takeoff Distance [m]	442.16	533.62
	Range [km]	1869.80	1404.00
	Landing Distance [m]	442.16	533.62
	ROC [ft/min]	1558.50	1311.90
	Takeoff Angle [°]	9.83	7.96
<b>Fuselage</b>	Length [m]	8.12	8.87
	Cabin [m]	2.40	3.15
	Nose [m]	2.21	2.21
	Tail [m]	3.51	3.51
	Cabin Diameter [m]	1.70	1.70
<b>Horizontal Tail</b>	$S_{HT}$ [m <sup>2</sup> ]	2.23	1.84
	$AR_{HT}$	6.31	5.36
	$c_{r_{HT}}$ [m]	0.76	0.75
	$\lambda_{HT}$	0.57	0.55
	$V_{HT}$	0.65	0.52
	$b_{HT}$ [m]	3.75	3.14
	$c_{mac_{HT}}$ [m]	0.59	0.59
	$x_{HT}$ [m]	7.58	8.11
	$\Lambda_{HT}$ [°]	0.00	0.00
<b>Vertical Tail</b>	$S_{VT}$ [m <sup>2</sup> ]	0.84	0.63
	$AR_{VT}$	3.27	4.27
	$c_{r_{VT}}$ [m]	0.70	0.54
	$\lambda_{VT}$	0.44	0.41
	$V_{VT}$	0.022	0.016
	$b_{VT}$ [m]	1.66	1.64
	$c_{mac_{VT}}$ [m]	0.50	0.38
	$x_{VT}$ [m]	7.66	8.32



	$\Lambda_{VT}$ [°]	0.00	0.00
<b>Control Surfaces</b>	Aileron Root Chord [m]	0.31	0.31
	Aileron Tail Chord [m]	0.29	0.29
	Aileron Span [m]	0.50	0.50
	Y-position Aileron [m]	5.99	5.99
	Elevator Root Chord [m]	0.19	0.18
	Elevator Tail Chord [m]	0.11	0.10
	Elevator Span [m]	3.75	3.14
	Rudder Root Chord [m]	0.35	0.27
	Rudder Tail Chord [m]	0.16	0.11
	Rudder Span [m]	1.66	1.64
<b>Landing Gear</b>	$x_{Landing.gear-Nose}$ [m]	1.11	1.15
	$x_{Landing.gear-Main}$ [m]	4.26	4.43
<b>Electrical Engine</b>	Takeoff Power [kW]	240.00	230.00
	Climb Power [kW]	228.12	216.99
	Cruise Power [kW]	150.43	151.04
	Descent Power [kW]	24.56	31.98
	$\eta_{prop}$	0.85	0.85
<b>Center of Gravity</b>	Empty $x_{CG}$ [m]	3.21	3.73
	MTOW $x_{CG}$ [m]	3.35	3.96
	TZFW $x_{CG}$ [m]	3.30	3.92
<b>Stability</b>	$c_{n\beta}$	0.054	0.066
	$c_{l\beta}$	-0.11	-0.11
	$c_{m\alpha}$	-0.38	-0.42
	Empty Static Margin	35.15	32.63
	MTOW Static Margin	16.72	12.89
	Trim Angle [°]	2.58	2.89
	Elevator Trim Deflection [°]	-1.79	-1.13

#### 4.5. Aircraft of Comparable Role and Configuration

Searching for other aircraft of the same category, it was found models such as the Cessna TTx, Cirrus SR22 and Diamond DA42. These aircraft present similar characteristic to the hybrid-electric aircraft designed here. As an exemplification, they are compared to the hybrid-electric aircraft of 4PAX in Table 16. In addition, they are placed over each other to show the differences in size, as show in Figure 13.



**Table 16: Aircraft of comparable role and configuration.**

Characteristics	Diamond DA42	Cirrus SR22	Cessna TTx	Hybrid 4PAX
Wing span [m]	13	11	11	13.38
Fuselage length [m]	8.56	8.28	7.68	8.12
Height [m]	2.49	2.72	2.74	2.96
Range [km]	1693	1289	2352	1875
Endurance [hr]	8.8	4.5	5.25	7.22
Cruise speed [km/h]	326	226	435	343
Takeoff field [m]	776	600	390	442
Landing field [m]	620	620	805	442
MTOW [kg]	1999	1111	1633	1855
Passengers	3	3	3	3
Fuel [kg]	231	220	280	176
Service ceiling [m]	5500	4100	7620	3660
Climb Rate [ft/min]	1337	720	1400	1559

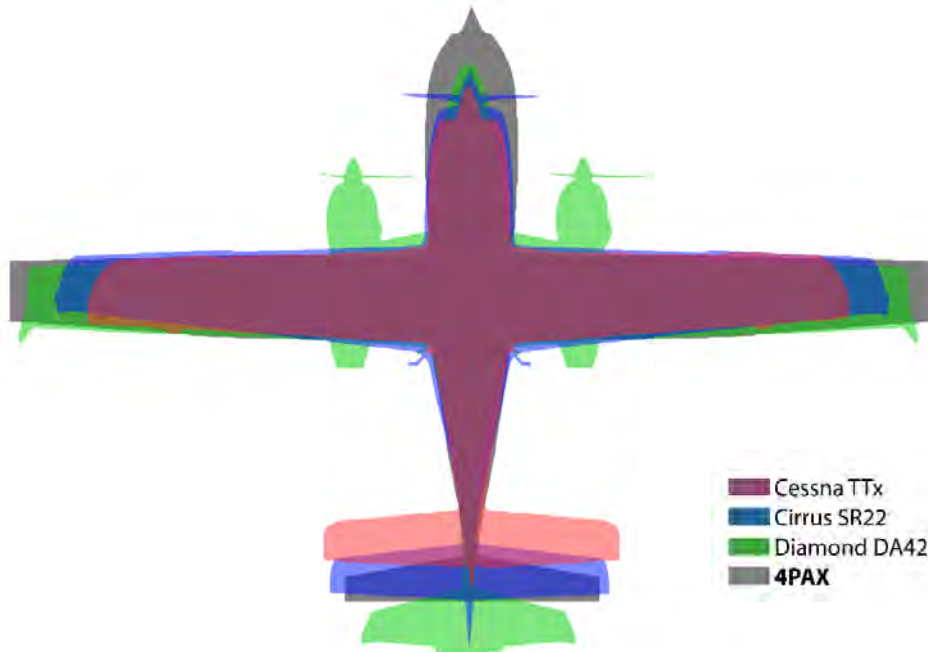


**Figure 13: Aircraft of comparable role and configuration overpainted.**

Therefore, the aircraft developed in this work meet the AIAA requirements and also is competitive in the aviation market. Since it presents good general and performance characteristics, its main differential certainly would be lower fuel consumption because of the hybrid-electric system on board, attracting new customers. The aircraft presents a longer and larger nose compared to the other aircraft because all the propulsive system, which includes batteries, inverter, ICE, generator, controller and electric motor, was assumed to be placed at the front of the aircraft. Due to its similarity, that “big” nose inspired the name of the aircraft: Dolphin. Thus, the aircraft of 4 passengers was named Dolphin 4000 and the one of 6 passengers, Dolphin 6000.



## 5. Aerodynamic Analysis

The goal of the aerodynamic design was to find the best compromise between drag and lift, especially to the cruise phase by ensuring a high lift to drag ratio to maximize the range of the aircraft and to reduce the battery's weight. Some challenges were initially identified by the aerodynamic sector in reason of some conflicting requirements of the spec. The requirements are:

- High minimum climb rate of 1500 ft/min;
- Same wing geometry to both aircraft to ensure high commonality (imposed by the team);
- Considerable battery weight to sustain a minimum cruise speed of 174 knots.

### 5.1. Conceptual Aerodynamic Design

#### 5.1.1. Wing Planform

The first step was the determination of the wing planform to be used in both aircraft, and some initial considerations about the structural twist and aerodynamic tailoring to guarantee good spanwise lift distribution to minimize the induced drag factor (K).

Firstly, some aircraft with fairly recent designs were analyzed to study the aspect ratio tendency. Eight aircraft were considered: DA-42, DA-62, Cirrus SR22, Cessna TTx, Bonanza S35, Piper Seneca, Cessna 206 and the Cessna 210. The geometric characteristics of the eight wings are shown in Table 17.

**Table 17: Wing characteristics of similar aircraft.**

	Aircraft	Year	Wingspan [m]	Wing Area [m <sup>2</sup> ]	Aspect Ratio
Recent Aircraft	DA-62	2012	14.57	17.1	12.41
	DA-42	2002	13.56	16.3	11.29
	Cirrus SR22	2001	11.68	13.5	10.11
	Cessna TTX	2004	11	13.1	9.24
Older Aircraft	Piper Seneca	1971	11.96	19.3	7.38
	Cessna 206	1962	10.92	16.3	7.32
	Cessna 210	1957	11.2	16.2	7.73
	Bonanza S35	1947	10.21	16.8	6.21

Due to the high climb rate imposed by the spec, a range including high values for aspect ratio, as the more recent aircraft shown in Table 17, was considered. The choice for a high aspect ratio is beneficial due to good glide characteristics, low induced drag factor and high maximum lift coefficient (closer to the airfoil). It was stipulated a



range for AR between 12 and 13.5. Although high AR leads to low flutter velocities, this characteristic is not critical to this project since the flight regime is below Mach 0.4.

With the goal of ensuring low manufacturing cost, elliptical planforms were eliminated, moreover excluding unfavorable stalling characteristics presented in these types of geometry. Therefore, only aerodynamic surfaces defined by terms of straight lines were considered and three configurations: rectangular tapered, double tapered and triple tapered were pondered.

According to Thomas [F. Thomas, 1984] the combination of trapezoidal section together with the appropriate distribution of structural twist can produce a planform that performs nearly as well as an elliptical distribution, overcoming the stalling problems. Thomas states that a double tapered wing with  $-3^\circ$  twist in the outer section seems to offer the best compromise, which can be seen in Figure 14. These results were obtained for  $AR = 25$  but vary little with aspect ratio. Thus, a structural twist of  $-3^\circ$  was assumed.

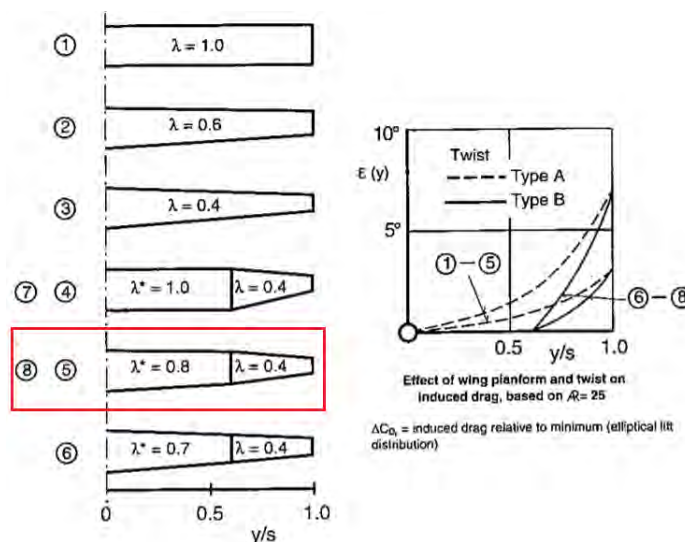


**Figure 14: Effect of wing planform and twist on induced drag [F. Thomas].**

Thomas in his book also states that both theoretical investigations and practical experience suggest that a double tapered wing having a taper ratio of 0.4:0.8:1 and a taper break at  $y/s = 0.6$  yields especially good results. Triple tapered wings have featured only designs where there is an intense need for better approximate of an elliptical planform, as can be seen in some sailplanes, such as the Discus, ASH 25 and Nimbus 4. To continue ensuring low manufacturing costs, a double taper configuration was assumed to be enough to ensure good lift distribution.

Still analyzing Table 17, it is possible to observe a tendency for wing area in the range of 13 to 17  $m^2$  for more recent aircraft. Taking into consideration that almost all aircraft structure will be manufactured using composite



materials, which leads to low empty weight, a decision for a small wing area was taken. A small range of 13.5 to 14 m<sup>2</sup> was assumed for the wing area. The maximum wing root chord was also limited to 1.4 m, in order to reduce the percentage of the turbulent boundary layer over the chord of the entire wingspan. This decision was based on light aircraft that have used this strategy to keep as much laminar region as possible to reduce drag.

So far, it has been determined the range for the wing's aspect ratio, the structural twist, the number of sections of the wing, wing area and an initial idea about how the taper ratio and break point can occur. Table 18 shows all the ranges for the wing's characteristics.

**Table 18: Wing characteristics and range of variables**

Characteristic	Value	Unit
AR	12 - 13.5	---
Twist	3	°
Area	13.5 - 14	m <sup>2</sup>
Number Sections	2	---
Max Chord	1.4	m
Taper	Double tapered	---
Taper Brake Point	0.6	y/s

### 5.1.2. Airfoil Section

The selection of the airfoils was done considering the following requirements:

- to exhibit low drag in high-speed flight (low lift coefficient);
- to provide a high maximum lift coefficient for low landing and takeoff speeds;
- to contribute to gentle stall characteristics;
- to be as thick as possible to allow deep spars and high torsional stiffness;

The last three requirements do not conflict and are easy to solve by using thicker airfoils, which tend to be superior in low-speed flight; however, the first requirement is usually solved by adopting thin airfoils and increasing performance at high speeds. Although the four requirements are conflicting, relatively good performance can be reached by balancing out thin and thick airfoils at certain regions of the wing.

The choice of airfoils was thought so that flow separation occurs first on the inboard sections of the wing. This prevents premature loss of aileron control and reduces the tendency of the aircraft to fall off on one wing and enter into a spin. To solve this problem, the incidence of the wing's root airfoil had to be set so that the maximum lift coefficient was exceeded first on the inboard section of the wing.



Although it was stated that a taper ratio of 0.4:0.8:1 yields especially good results for lift distribution (elliptical), the  $C_L$ -distribution of rectangular tapered wing gives the best stalling behavior. Nonetheless, having an elliptical wing geometry makes the  $CL_{max}$  to be reached along the entire wing all at once, and the stall characteristics may be problematic. This way, the final taper ratio of the wing is still open and might be a little different of 0.4:0.8:1.

To improve the stall characteristics of the double tapered wing, different airfoils were considered. In this respect, the airfoils, especially in the outer wing, was selected to gentle trailing edge stall behavior.

Considering the MTOW of both aircraft, 1855 kg for the Dolphin 4000 and 1966 kg for the Dolphin 6000 (see Table 15 in Section 4.4), and taking into consideration the atmospheric conditions at 12000 ft, the  $C_{L_{cruise}}$  is around 0.38 for the Dolphin 4000 and 0.40 for the Dolphin 6000 for minimum cruise velocity.

Based on the family of airfoils of some similar aircraft and on the considerations made before, airfoils NACA five-digit and 6-series were selected to further study of the aerodynamic characteristics. An especial attention was given to the airfoils of the five-digit family due to the big experimental data available [Abbot & Doenhoff] that match close Reynolds number of the mean aerodynamic chord of the wing at cruise speed.

Table 19 shows some characteristics of eight airfoils for two Reynolds numbers, four of them thought to the inner sections of the wing and the last four to the outer sections. Almost all airfoils chosen were designed to have lift coefficient of 0.3. Although the lift coefficient of the aircraft is closer to 0.4 than it is to 0.3, such decisions were based on the fact that at least 10% of the total lift of the aircraft will come from the fuselage for cruise configuration.

**Table 19: Airfoil's characteristics.**

Airfoil	Designed Location	Designed $c_l$	$C_{Lmax}$ Re=3e6	$C_{Lmax}$ Re=6e6	$C_m$ at designed $c_l$	$C_d$	LE radius
N23015	Root	0.3	1.5	1.7	-0.03	0.0059	2.48%
N23016	Root	0.3	1.78	1.85	-0.01	0.0060	2.82%
N64415	Root	0.4	1.48	1.6	-0.3	0.0050	1.59%
N63415	Root	0.4	1.53	1.63	-0.3	0.0052	1.59%
N23010	Tip	0.3	1.71	1.82	-0.01	0.0054	1.10%
N23012	Tip	0.3	1.6	1.72	-0.04	0.0050	1.58%
N64210	Tip	0.2	1.35	1.41	-0.18	0.0043	0.72%
N64212	Tip	0.2	1.4	1.45	-0.18	0.0045	1.04%

The analysis of the airfoils from Table 19 reveals that though the NACA 6-series presents smaller values of drag coefficient than the NACA five-digit, due to the laminar bucket, the small leading-edge radius leads to lower maximum lift coefficients in reason of rapid acceleration or deceleration, resulting in sharp pressure gradient [S.



Farokhi]. Furthermore, the 6-series airfoils produce considerable aft load if compared to the five-digit family, which requires larger horizontal tails; consequently, more drag can be generated when considering the entire aircraft. Although the drag coefficients are slightly higher for the five-digit, the good surface quality offered by the carbon fiber together with a good manufacture precision can help to reduce the friction drag. Therefore, the airfoils NACA23016 and NACA23015 were considered to the inner sections of the wing and the airfoils N23012 and NACA23010 to the outer sections.

### 5.1.3. Optimization of the Wing Planform

To determine the final planform of the wing, an advanced differential evolution algorithm was used. In this process, modules of performance, stability & control and aerodynamics (coupled with the AVL software) using Matlab was employed to help meet all the criteria imposed (climb ratio, range, etc.). The range of all parameters and goals of the optimization process are shown in Table 20.

**Table 20: Optimization range of all parameters and optimization goals**

Variable	Lower Limit	Upper Limit	Unit
AR	12	13.5	---
S	13.5	14.5	m <sup>2</sup>
<i>c<sub>root</sub></i>	1.2	1.4	m
Structural Twist	-3	-3	°
Taper	0.4:0.7:1	0.7:0.8:1	---
Taper Break Point	0.45	0.65	---
Variable	Goals		
Aerodynamic Eff.	>13.5		---
<i>CL<sub>max</sub></i> w/o flaps	minimum 1.7		---
<i>CL<sub>cruise</sub></i>	0.38 (D4000) & 0.40(D6000)		---
Cruise Velocity	> 174		Knots

The optimization process was repeated several times to ensure that the same solution was reached at the end of each run. The final geometry was later analyzed using other potential solvers such as the Non-Linear Lifting Line coupled with viscous corrections to check the aerodynamics coefficients obtained using AVL. The final planform of the wing can be seen in Figure 15.

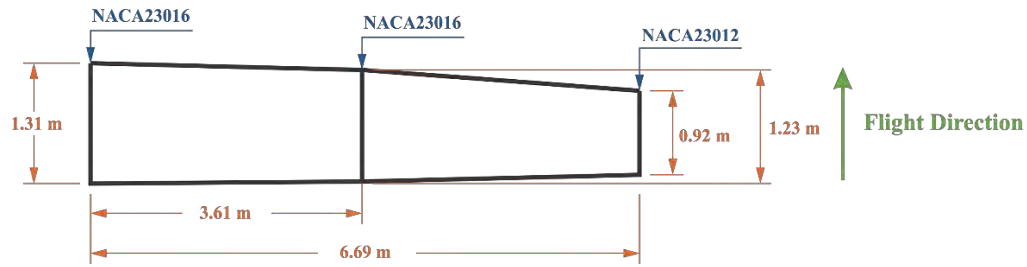


Figure 15 - Final wing planform

## 5.2. High Lift Devices

In order to fulfill the requirements stipulated by performance sector, a flap was designed to reach  $C_{L_{max}}$  of 2.14. The main idea was to introduce the structure only in the first section of the wing to reduce the manufacturing complexity and with 20% of the local chord.

The theory of lift induced by partial span flaps below stall presented by Roskam was used to verify the  $C_L$  increase due to the chosen flap. The  $C_L$  increase should be enough to achieve the ratio of climb specified previously and to land at low speeds.  $\Delta C_L$  was estimated using the Lowry and Polhamus's method and reached a value of 0.47 for a small deflection of  $15^\circ$ , which is high enough to provide the lift requested.

## 5.3. Fuselage

The design process of the fuselage, as mentioned before, had the goal of producing at least 10% of the total lift of the aircraft during cruise flight. Besides that, the right position of all internal components had to be ensured to guarantee correct CG location with an external shape that generates minimal drag force.

A design close to a slender shape was thought to reduce the drag coefficient by avoiding any detached flow over the entire fuselage and without impairing visual capacity inside the cockpit. The initial design was based (inspired) on the aircraft Pipistrel Panthera. The sketch of the fuselage is shown in Figure 16.

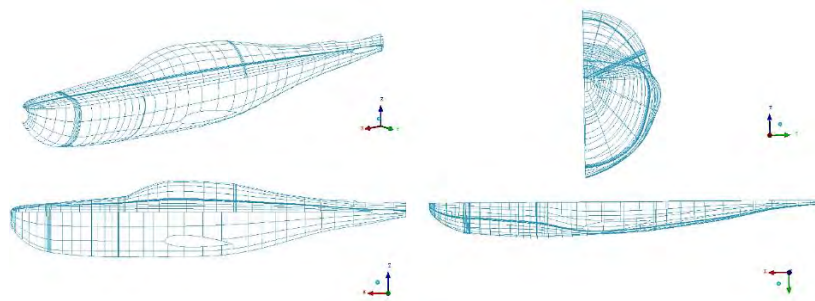


Figure 16: Views of the fuselage.



## 5.4. CFD Analysis

To better analyze the flow characteristics and take into consideration the boundary layer and turbulence effects, some computation fluid dynamics simulations (CFD) were performed using the complete aircraft geometry. The two-equation model *k-epsilon*, one of the most traditional turbulence models still in use, was employed in Ansys Fluent® solver. This model was chosen due to a better facility of convergence and lower computational cost inherent to its numerical methodology. Besides that, the *k-epsilon* turbulent model allows us to work in the *log-law* region ( $30 < Y^+ < 300$ ), requiring meshes with less prism layer elements at the wall. In reason of large pressure gradients and possible detached flow at high angles of attack (AoA), the options *Realizable* (RKE) and *Non-equilibrium wall function* were applied. The scheme couple (pressure-velocity) together with the pseudo transient option were used to speed up (accelerate) convergence.

All the unstructured meshes produced using the software Ansys ICEM® contained around  $4.7 \times 10^6$  elements, most of them tetra elements. The size of the domain was  $150 \times 100 \times 50$  mean aerodynamic chords to avoid wall interference even though symmetry condition was set on some walls. The maximum stretching ratio was 5.45 to ensure good mesh quality and 8 prism layers were used to keep  $Y^+$  between 30 and 300. Figure 17 shows some mesh characteristics in more detail.

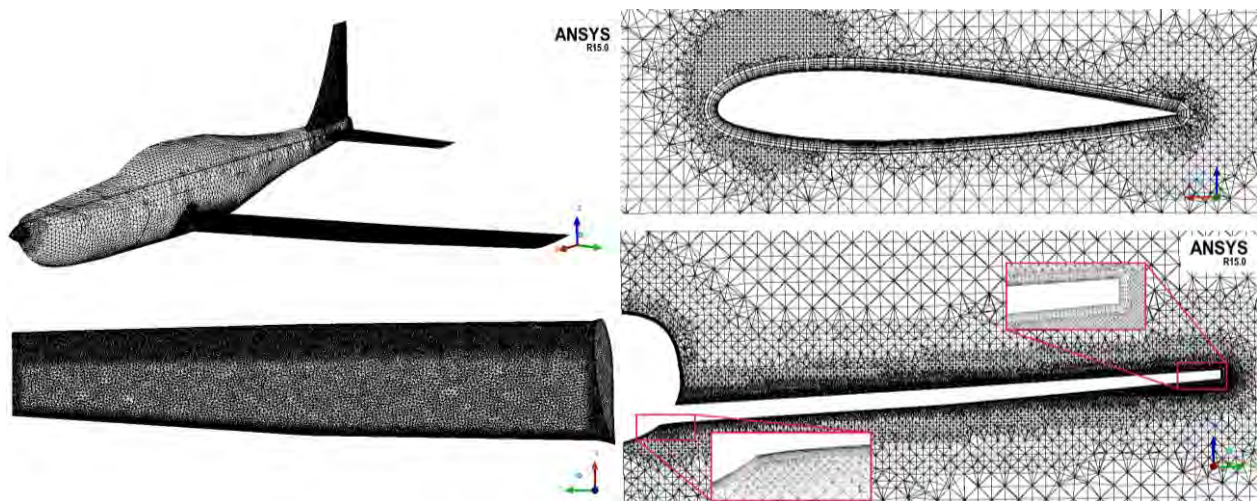


Figure 17: Mesh details.

### 5.4.1. CFD Optimization

Although the criteria for aerodynamic efficiency had been reached during the optimization process using the aerodynamic solver AVL, the solutions based on potential methods do not offer high precision for viscous drag



calculations and enough detail about the flow field. Hence, some CFD simulations, especially at cruise speed configuration, were performed to identify possible regions subject to modifications to increase even more the aerodynamic efficiency. All the simulations were performed using the software Ansys Fluent.

### 5.5. Interference Drag – Wing Fuselage

The initial CFD results revealed that the lift to drag ratio was smaller than the one predicted by AVL due to a considerable region of separation caused by the interference of the boundary layer of the wing root with the one of the fuselage, causing a wake that propagates over the aft part of the fuselage, resulting in additional pressure drag (interference drag). The angle between the root upper wing surface and the fuselage's wall contributes significantly to this interference drag [F. Hoerner, 1965], since the angle was considerably smaller than 90 degrees, increasing the separation in the narrowed area. Figure 18.a shows the detached streamlines at this region for cruise condition.

To solve this problem, five optimization runs were conducted using the adjoint solver and taking the drag force as an observable variable. The final geometry presented a reduction of drag coefficient of 5.1% and increased the lift to drag ratio in 11.5%, bringing it to 13.58. The lift coefficient was also increased by 6.1% due to the flow reattachment and the aircraft passed to fly at  $2.3^\circ$  of AoA with the fuselage producing 11.2% of the total lift. Figure 18.b shows the final result during cruise condition for the aircraft Dolphin 4000.

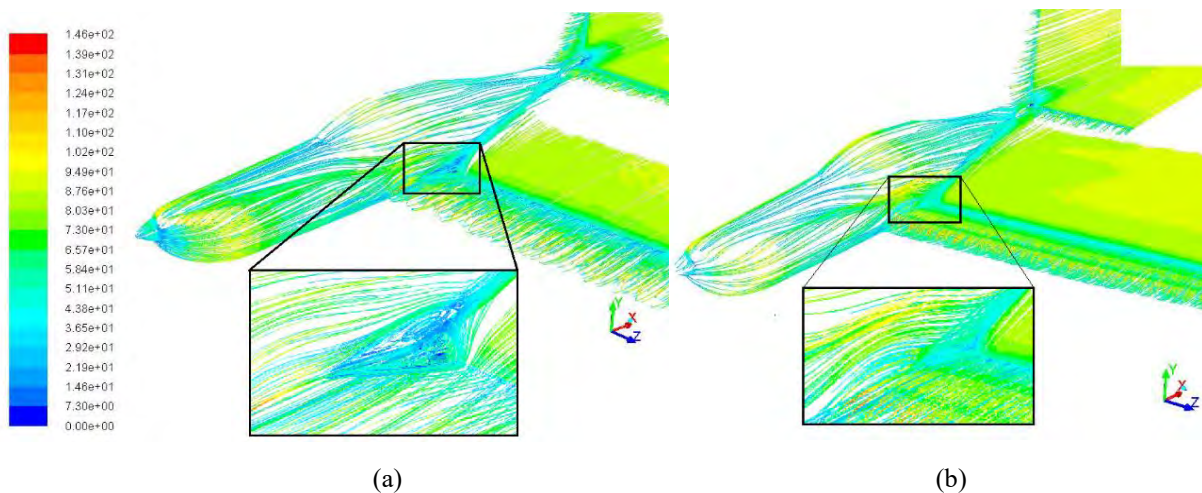


**Figure 18: (a) Detached streamlines at the wing root and (b) Final result obtained using the Adjoint solver.**



## 5.6. Winglets

Although the aerodynamic efficiency had reached the target value of 13.58, the CFD simulations did not take into consideration the drag caused by the presence of gaps at the surfaces. To account for this portion of drag force, the actual drag coefficient was increased by 8%. Notwithstanding some references that suggest an increase of 10%, a smaller percentage was considered since the aircraft was manufactured almost entirely employing composite materials, which guarantee good surface quality and brings the number of exposed rivets almost to zero. Therefore, there was still a need for increasing the aerodynamic efficiency of the aircraft.

In order to satisfy the need for a higher aerodynamic efficiency, four types of wingtip devices were analyzed aiming to reduce the induced drag, which is mostly generated by the wingtip vortices. The first geometry was just a “smoothing” of the wingtip, an attempt to avoid the boundary layer detachment caused by the sharp edges. Furthermore, winglets were analyzed with geometries based on shapes often used in the industry. Three different geometries were then created by changing the tip chord, height and curvature radius, in order to gain the best ratio between surface friction area increase and vortex reducing. All the four geometries were drawn on CATIA, as shown in Figure 19.



**Figure 19: Four geometries analyzed.**

The visual post-processing of the results was done using the ANSYS CFS-POST software, and to save a lot of visual information, only the result of the winglet B, which produced the best results, is presented here. In order to verify the presence of vortices, the CFD-POST visualization method called *vortex core region* was used. Figure 20 shows a large presence of vorticity in the geometry without wingtip and a considerable reduction of this parameter in the wing that employs the device.

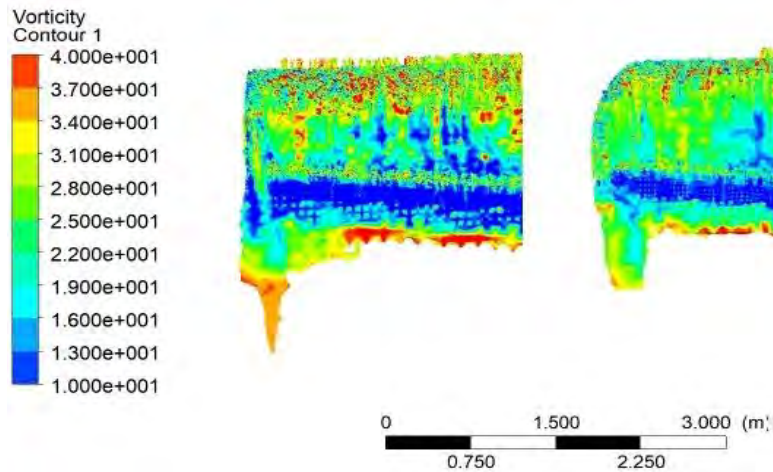


**Figure 20: Vorticity distribution without the wingtip (left) and with the wingtip(right)**

The final aerodynamic efficiency for the Dolphin 4000 was 14.8 not considering the losses caused by imperfections at the surfaces and 13.7 after accounting the 8% of additional drag.

### 5.7. Final Drag Polar

Figure 21 shows the final drag polar already corrected with 8% of addition drag to account for surface gaps and imperfections for the Dolphin 4000 and 6000. It is possible to observe that both aircraft flight in the region close to the maximum aerodynamic efficiency using the same wing planform and airfoils, which contributes to ensure high commonality and low manufacturing costs.

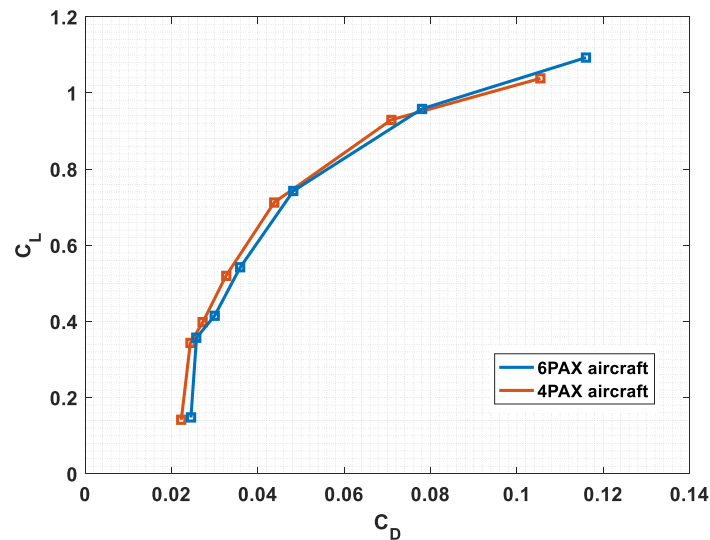


**Figure 21: Final drag polar for both aircraft.**



## 6. Performance Analysis

### 6.1. Take-off analysis

The takeoff analysis was performed with the following characteristics: aircraft in its MTOW and using both ICE and battery bank. At first, the analysis of the obstacle of 50 ft that the aircraft must overcome will be done separately.

The 4PAX and 6PAX aircraft will climb at an approximate angle of  $9^\circ$  and  $8^\circ$ , respectively, as it will be demonstrated in this report in the following sections. Therefore, to overcome the 50 ft obstacle they will need, approximately, 282 and 256 ft (86 and 78 m) of runway. As both aircraft have been requested to takeoff using less than 1500/1800 ft (457.2/548.6 m), there is a length of ground takeoff left for the aircraft of 1218/1544 ft (367/470 m).

Using the equations of the literature for ground takeoff and assuming that the takeoff velocity is approximately 1.2 of stall velocity (historical trend of aircraft), the following graphs are given for the takeoff of the 4 and 6 PAX aircraft, varying the altitudes.

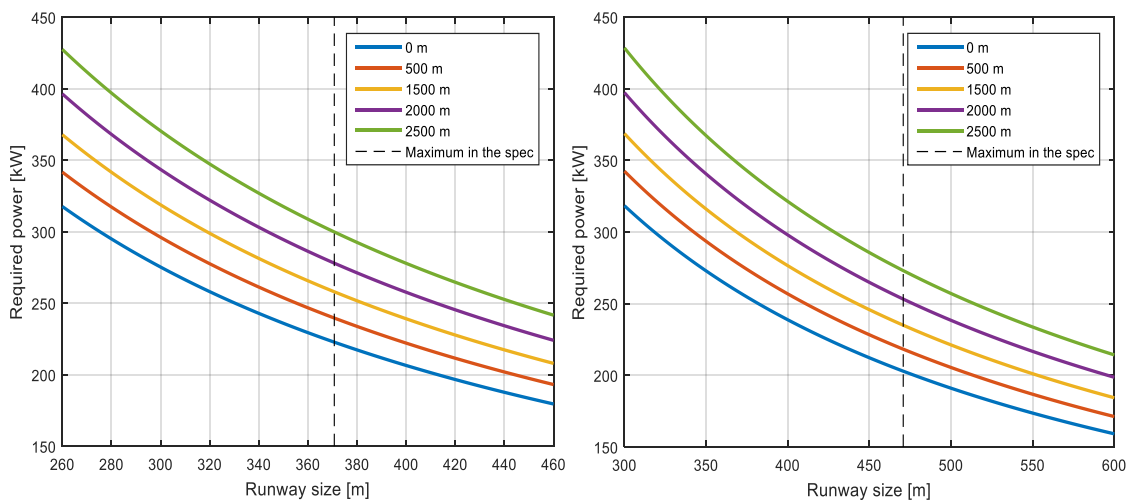


**Figure 22: Required thrust vs. required takeoff runway. 4PAX (on the left) and 6PAX (on the right).**

To accomplish the requirements of the specifications, it is possible to note from the graphs above (Figure 22) that the 4PAX aircraft needs 224 kW (sea level + 18 °F) and 259 kW (1500 m ~ 5000 ft) of power during take-off; for the 6 PAX aircraft, it is necessary 205 kW (sea level + 18 °F) and 237 kW (1500 m ~ 5000 ft). If the total power (260 kW) is used, the 4 PAX aircraft can take off at sea level + 18 °F using 317.5 m, while the 6 PAX a value of 367.2 m. This analysis is for a standard concrete runway.



The analysis for a grass runway is similar, changing only one variable in the literature equations (precisely the variable that represents the runway friction coefficient). The results for this kind of runway are: 4 PAX – 262 kW (sea level + 18 °F)/301 kW (5000 ft); 6 PAX – 251 kW (sea level + 18 °F)/288 kW (5000 ft).

Thus, it is possible to conclude that the projected aircraft fulfill the design requirements, since the electric motor chosen in the conceptual design has the desired power for taking off.

As shown in the conceptual design, it was decided that the optimal hybridization for the aircrafts during takeoff is 42%, however the graphs of Figure 22 show that the aircraft operator is allowed to vary that hybridization if desired and depending on the type operation.

## 6.2. Aircraft climb

The climb analysis was performed with the following characteristics: aircraft using only 0.8% of the fuel during takeoff, and using ICE and electric batteries.

To make the analysis easier, two dimensionless parameters were included, which are:

- 1-  $\lambda = \eta \cdot \frac{P}{D_{min} \cdot V_{MD}}$  ( $\lambda$  is maximum when the power is maximum);
- 2-  $u = \frac{V}{V_{MD}}$

where,

- $\eta$  = propeller efficiency = 0.85 (as determined in the conceptual design);
- $P$  = Total power
- $V_{MD}$  = Minimum drag velocity,  $V_{MD} = \sqrt{\left(\frac{2 \cdot \text{Aircraft weight}}{\text{Wing area} \cdot \rho}\right) \cdot \sqrt{\frac{K}{C_{D0}}}}$ , where K and  $C_{D0}$  coming from the drag polar;
- $D_{min}$  = Minimum drag that the aircraft can suffer (constant =  $0.5 \cdot \rho \cdot V_{MD} \cdot \text{Wing Area} \cdot 2 \cdot C_{D0}$ ). This value is constant due to the fact that the density of the equation will cancel out with the density coming from the minimum drag velocity. For the 4 PAX aircraft  $D_{min} = 995$  N, while for the 6 PAX  $D_{min} = 1054.6$  N;

Using the literature for an aircraft climb, the following charts of sea level + 18 °F climb for the 4PAX (Figure 23) and 6PAX (Figure 24) aircraft are obtained.

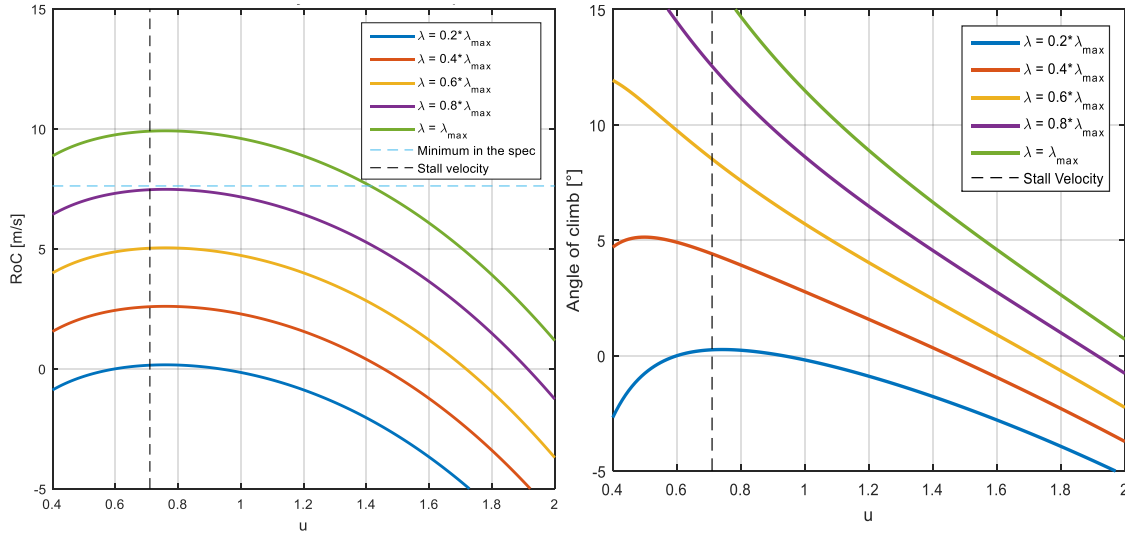


**Figure 23: Rate of climb (on the left) and angle of climb (on the right) vs. relative airspeed (u) for 4PAX aircraft.**

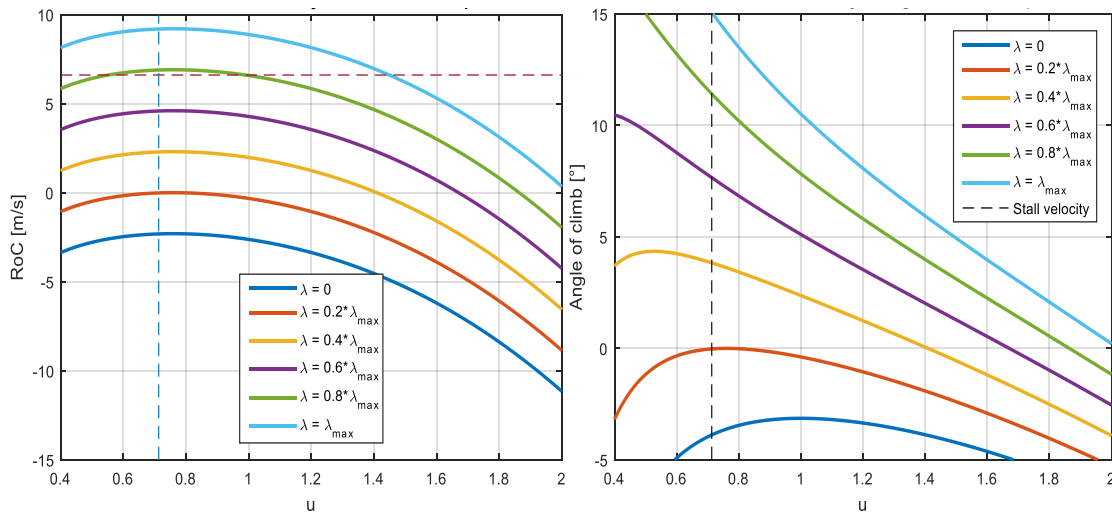


**Figure 24: Rate of climb (on the left) and angle of climb (on the right) vs. relative airspeed (u) for 6PAX aircraft.**

As the specification requires a minimum rate of climb of 1500 ft (7.62 m/s) and respecting the stall velocity, the first graph of Figure 23 shows that the 4 PAX aircraft should rise with a power above 80% of total power and with velocity “u” between 0.7 and 1.41. However, when analyzing the second graph of the same figure, it is noticed that for low velocities the angle of climb is very high, something that cannot happen in practice. Thus, it can be concluded that the ideal climb velocity is with a “u” between 1.2 and 1.4 – giving a rate of climb between 2746 fpm (8.87 m/s) and 1500 fpm (7.62 m/s) with an angle between 8.9 and 6.5 degrees. Doing the same analysis in Figure 28 for the 6 PAX aircraft (minimum rate of climb of 1300 fpm), it is also concluded that the power needs to be above 80% of total power, with velocities between 1.1 (1685 fpm and 9.25 degrees) and 1.45 (1300 fpm and 5.45 degrees).



### 6.3. Cruise condition

A cruise condition is the largest phase in the flight, so it is in it that the main features of a hybrid aircraft appear. As decided in the conceptual design, the cruising altitude will be 12000 ft (the pressurizing system is not necessary). For that altitude, keeping the admission parameter "u" already quoted and using the hybridization equation shown in the conceptual design (with a hybridization of 11%), it is possible to get the following charts for the aircraft cruising flight:

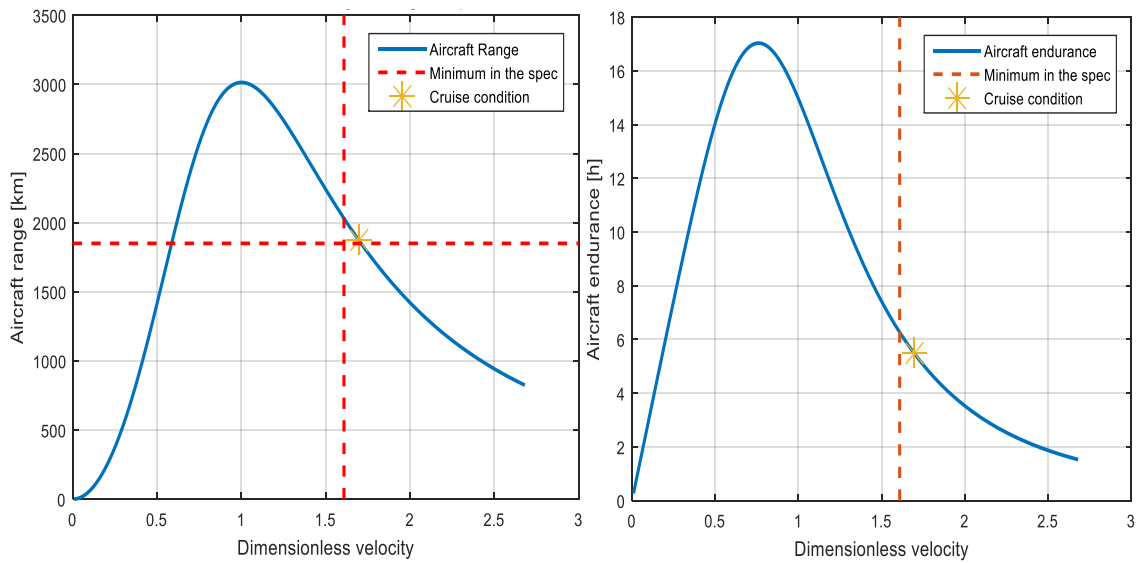


Figure 25: Range (on the left) and endurance (on the right) vs. relative airspeed (u) for 4PAX aircraft.

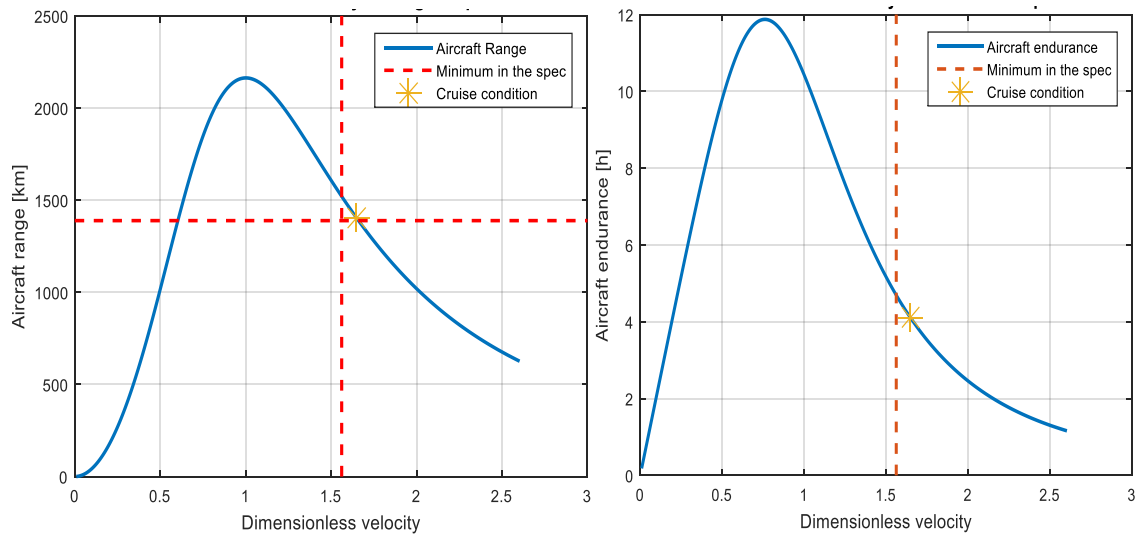


Figure 26: Range (on the left) and endurance (on the right) vs. relative airspeed (u) for 6PAX aircraft.



The spec requires that the 4PAX and 6PAX aircraft have a minimum range of 1000 nmi (1852 km) and 750 nmi (1389 km), respectively, and that the cruise velocity for both be at least 174 knots (322.25 km/h –  $u = 1.61$ ). Thus, the region that will meet these requirements is the region in the first quadrant (above and on the right) on the Rang chart of Figures 24 and 26.

It is desirable a cruise velocity close to 200 knots (370.4 km/h), so it was determined by the optimizer that the best point of the curve will be the one closest to the horizontal line separating the quadrants. Thus, the results for cruise condition obtained for both aircraft are:

**Table 21: Results for cruise condition.**

	<b>Range [km]</b>	<b>Endurance [h]</b>	<b>Velocity [km/h]</b>
4PAX	1870.30	5.47	338.91
6PAX	1404.02	4.01	342.25

An important information also obtained from Figures 25 and 26 is that both aircraft have a maximum range for " $u = 1$ " and a maximum endurance for " $u = 0.76$ ". These results are expected for a conventional propeller aircraft, i.e., the fact that the aircraft are hybrid did not change the behavior of the power system plus propeller.

In terms of range, the aircraft can go very far, as shown by Figure 27, which represents the range of the 4PAX aircraft after leaving two important airports in the Americas (Brasília – Brazil and Chicago – USA).

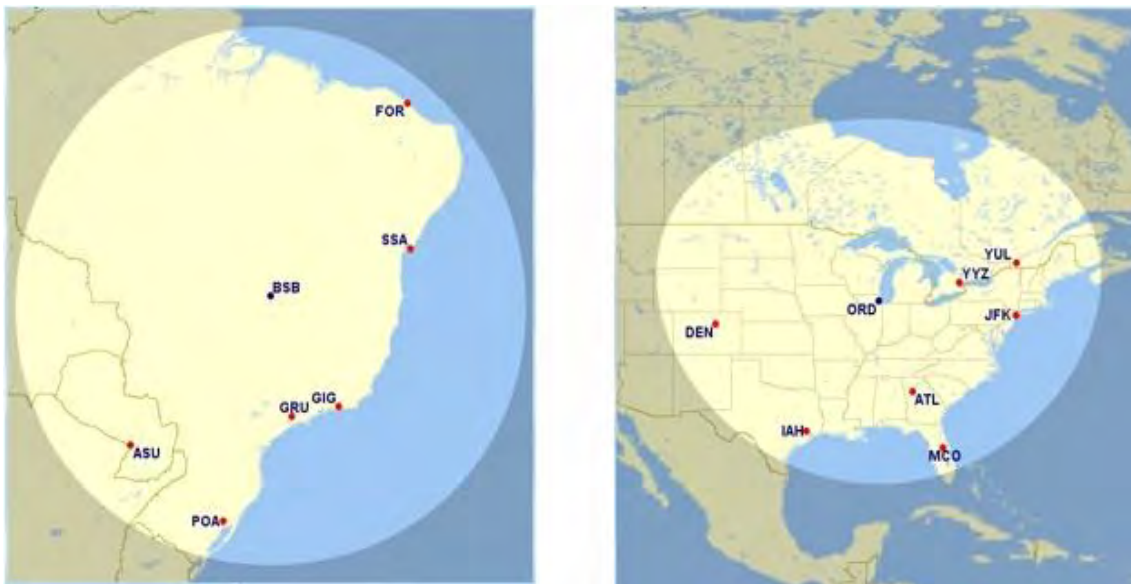


**Figure 27: Range of the 4PAX aircraft from Brasília (on the left) and Chicago (on the right).**

Now dealing exclusively with the hybrid part in performance, the following relationships on fuel consumption are important for analysis:

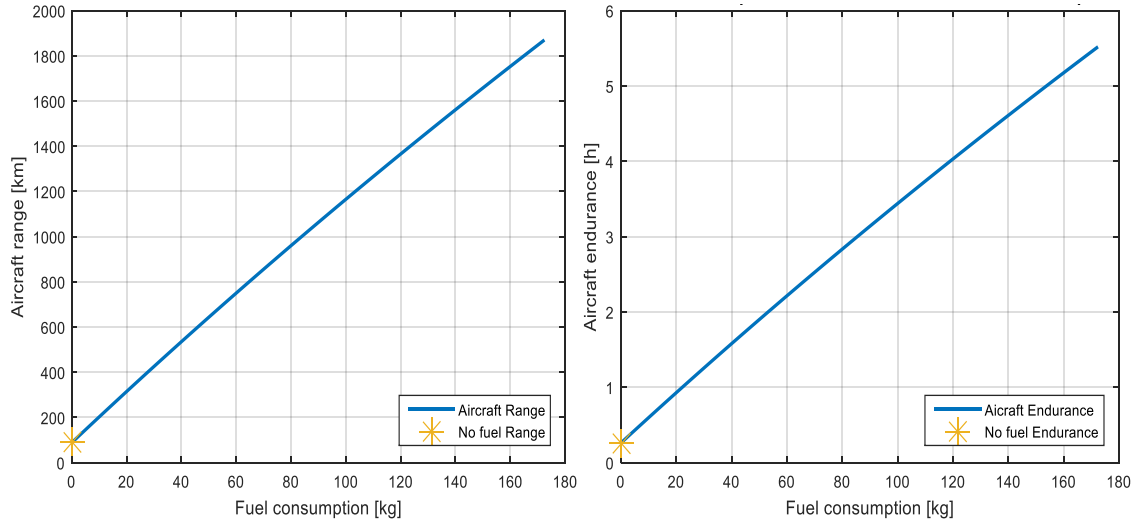


**Figure 28: Range (on the left) and endurance (on the right) vs. fuel consumption for 4PAX aircraft at cruise.**

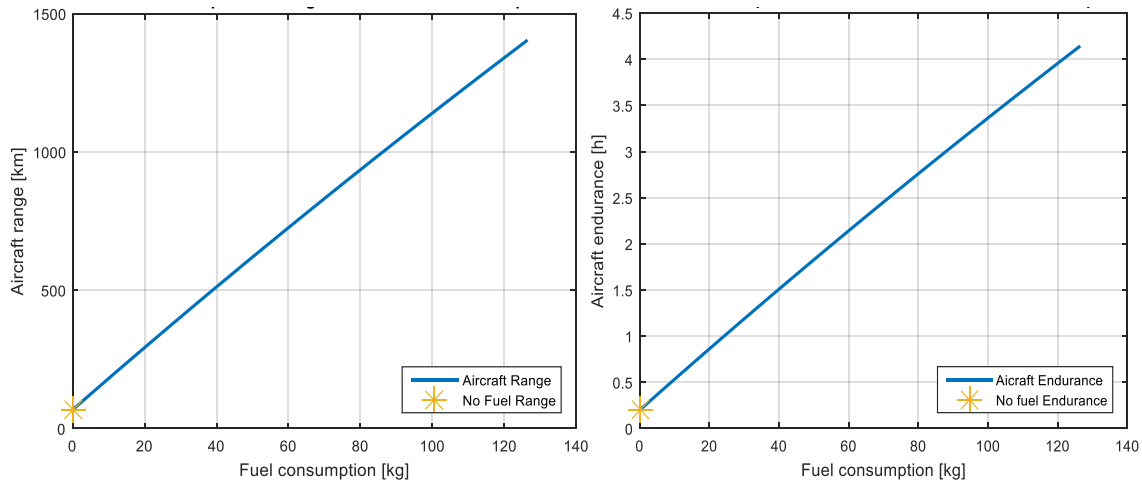


**Figure 29: Range (on the left) and endurance (on the right) vs. fuel consumption for 6PAX aircraft at cruise.**

Those graphs show that the aircraft have a range even with no fuel, since there is charge in the batteries. The results are presented in Table 22.

**Table 22: Results for cruise condition with no fuel.**

Cruise with no fuel	Range [km]	Endurance [h]
4PAX	82.83	0.24
6PAX	67.61	0.20

The necessary power to keep the flight in these conditions comes from the battery bank. With a higher hybridization value, the range with zero fuel will also be higher; however, the total range tends to decrease since the calorific power of the fuel is greater than that of the battery. Those graphs are also important to show to the pilot the range and the endurance that he or she has for a determined quantity available.



## 6.4. Landing

For the landing analysis, it was considered that the weight of the aircraft would be the weight of the battery for landing and emergency and a reserve of 10% of fuel. Keeping the ICE in idle, only the battery bank will be used, which allows a very quiet landing. The 50 ft obstacle is already included in the first analysis.

Using the landing performance equations, the results are:

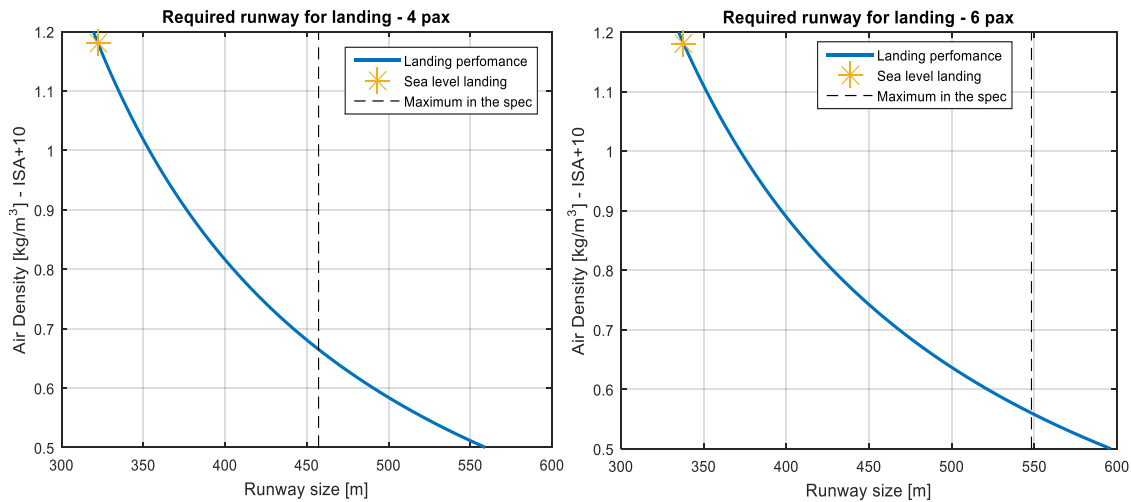


**Figure 30: Required runway for landing. 4PAX (on the left) and 6PAX (on the right).**

The graphs in Figure 30 show the landing runways required for the 4PAX and 6PAX aircraft at sea level + 18 °F and on concrete runway are 322.3 and 338 m, respectively. Using the maximum allowed runway size, the aircraft can land at places that the density is 0.67 and 0.56 kg/m<sup>3</sup> – ISA+18°F, which is equivalent to altitudes of 5500 and 7000 m. Just like in the takeoff analysis, on grass runway it is necessary to change one parameter of the equations, which leads to the following results:

- 4PAX: 390.7 m (sea level + 18 °F) and 3250 m (maximum landing runway size);
- 6PAX: 415.5 m (level + 18 °F) and 4850 m (maximum landing runway size).

## 6.5. Payload-Range Diagram

Another important curve in the performance analysis is the “Payload-Range” of the aircraft. It shows how far the aircraft, in cruise condition, can go with a certain quantity of fuel or payload.

Although in the preliminary design it was determined that the aircraft will carry, in cruise condition, 172.44 kg (4PAX) and 130.63kg (6PAX) of fuel, it was calculated that the wing can carry 200 kg of fuel for both aircraft. So,



for the second curve of the diagram, this value (200 kg) has been considered. The Payload-Range diagrams for both aircraft are shown in Figure 31.

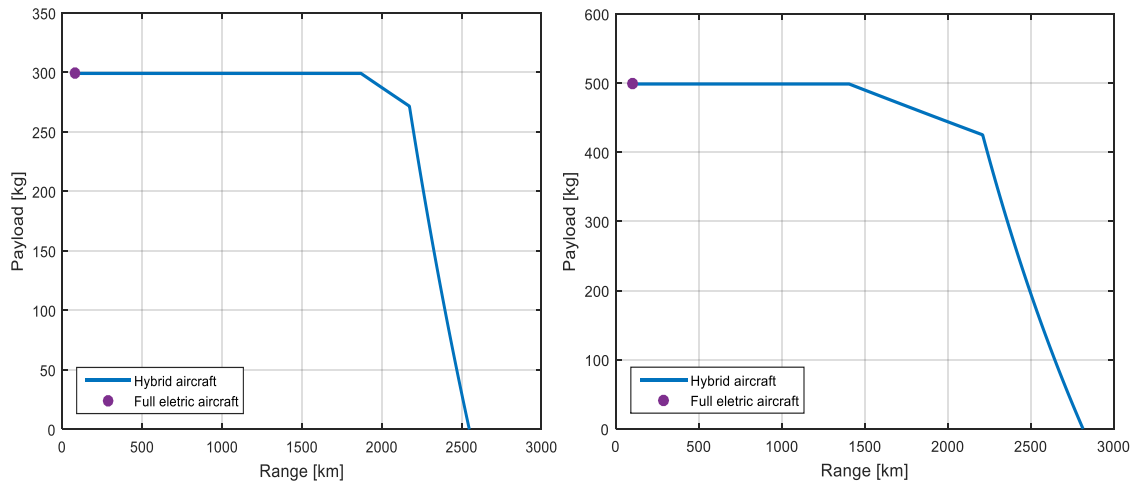


**Figure 31: Payload-range diagram of the 4PAX (on the left) and 6PAX (on the right) aircraft.**

The Payload-Range diagrams just confirm some of the information of the cruise condition: the maximum range to the maximum payload and that the aircraft has a range even with no fuel (just battery – full electric aircraft point in the graphic).

## 6.6. Emergency situation

It was proposed an analysis of how the aircraft would behave in an emergency situation: with the aircraft totally without fuel and at an altitude of 5000 ft AGL (ISA + 18 °F).

Then it was decided that the aircraft would have a reserve of battery only for emergencies (45 kg for 4PAX and 40 kg for 6PAX); besides the battery that is already reserved for the landing.

Two cases have been planned for the emergency situation:

- 1- The aircraft will continue in a straight flight until the fuel reserve is exhausted and proceed with a gliding flight until reach the ground;
- 2- The aircraft will descend with an ideal angle that will maximize their range and the batteries will end at the moment the aircraft touch the ground.

Here are the results obtained, considering that the aircraft are with full payload:



**Table 23: Results for emergency situation – First case with straight + gliding flight and second case with descent with an ideal angle.**

	First Case		Second Case		
	Range [km]	Endurance [h]	Range [km]	Endurance [h]	Angle [°]
4PAX	41.11	0.24	179.44	1.05	0.4866
6PAX	50.05	0.24	154.94	0.85	0.5636

As it is possible to see from the tables above, the descent situation with an ideal angle is the best for the aircraft and the range is large enough to perform the land.

Now analyzing only for curiosity another emergency situation, where there will be only the gliding flight, it is possible to obtain the maximum range of the aircraft according to their flight altitude through the following graphs:

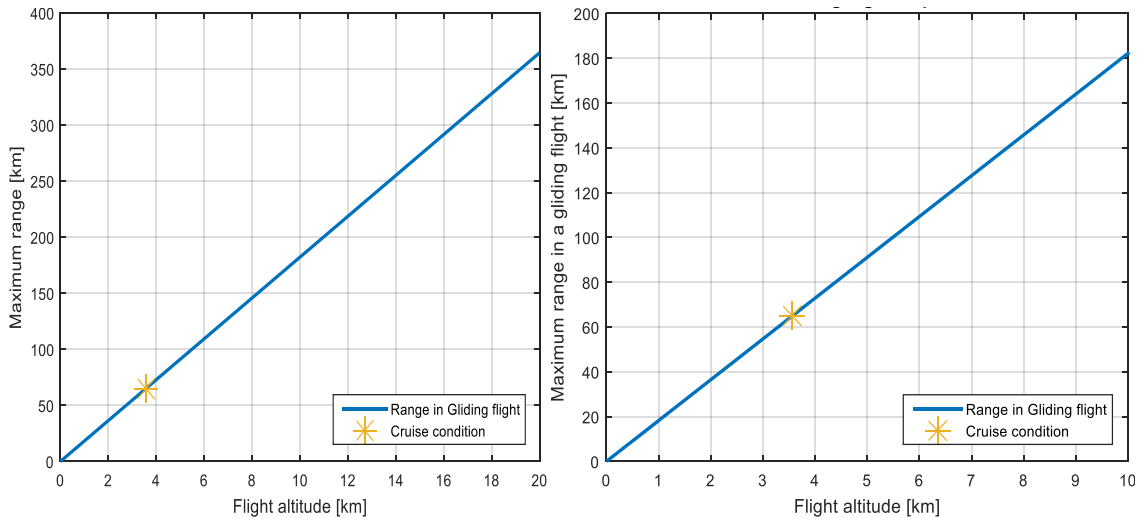


**Figure 32: Gliding flight for 4PAX (on the left) and 6PAX (on the right) aircraft.**

## 7. Structural Analysis

In any structural project, it is necessary to know the loads that the structure will be subjected. Thus, it is possible to better size the structure, avoiding failure and reducing weight, which is determinant for any aviation project.

The V-n diagram provides a treasure trove of information regarding flight performance for pilots. Following the procedures described in the FAA regulation [36], the V-n diagrams for both aircraft designed in this work were calculated. They are illustrated in Figure 36 and the results are arranged in Table 24. The colorful dots on both diagrams are the loads conditions evaluated, as explained later in Table 25 and 26.

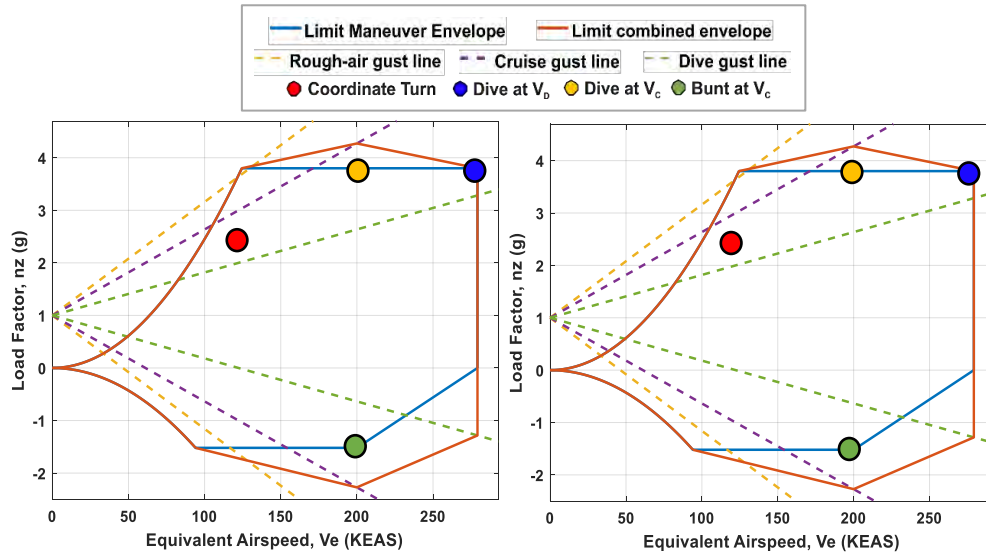


Figure 33: V-n diagram for 4PAX (on the left) and 6PAX (on the right) aircraft.

Table 24: Results from V-n diagrams.

Parameters	4PAX	6PAX
$n_{z_{max}}$	3.8	3.8
$n_{z_{max}^{Gust}}$	4.27	4.27
$n_{z_{min}}$	-1.5	-1.5
$n_{z_{min}^{Gust}}$	-2.1	-2.0
$V_G$	93.6 KEAS	96.0 KEAS
$V_A$	123.8 KEAS	127.0 KEAS
$V_C$	200.0 KEAS	200.0 KEAS
$V_D$	279.1 KEAS	278.9 KEAS

The image gives a never exceed speed and the limit load factors for a particular altitude of 12000 ft, which are arranged in Table 24. The parabolic curves, called the stall lines, are branching out from the origin on either side. Beyond around 280 KEAS and above 3.8G and below -1.0G, the airframe would be subject to structural damage.

In addition to the limit maneuver envelope curve, the diagram includes the gust lines, which represent the loads experienced when the aircraft encounters a strong gust (when flying close to a thunderstorm or during a clear air turbulence encounter) and may exceed the maneuver loads. Therefore, it is necessary to create a new envelope combining the gust loads, as shown in the diagrams.



Furthermore, it was necessary to ensure the structural design would handle all critical cases. Thus, some specific conditions had been chosen to evaluate the loads, such as: dive at  $V_C$ , dive at  $V_D$ , and bunt at  $V_C$  from V-n diagram; and coordinate turn from the maneuver boundaries. The gust loads analysis is planned to be performed using reduced models.

The maneuver boundaries are calculated using theory in [37] and shown in Figures 34 and 35. Analyzing the curves, the extreme condition possible during a coordinate curve is at a velocity of 64.6 m/s for 4PAX and 64.8 m/s for 6PAX.

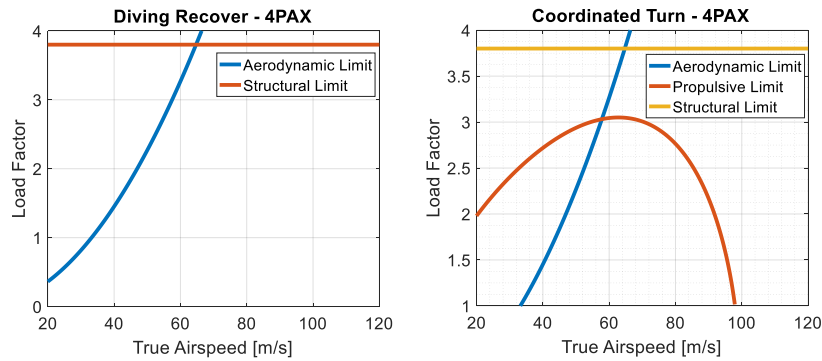


**Figure 34: Maneuver boundaries for 4PAX aircraft.**

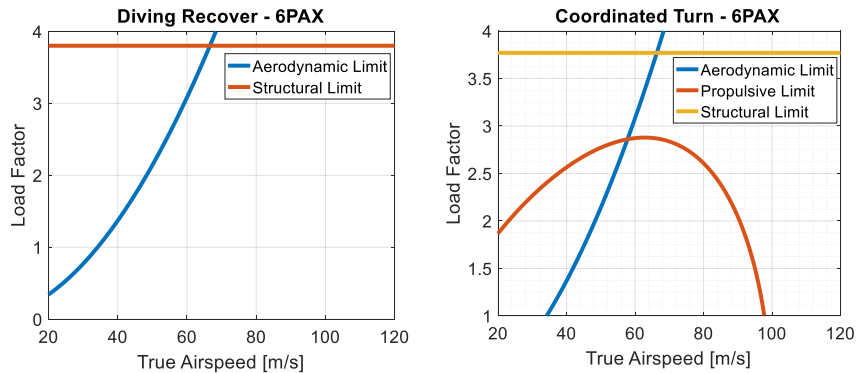


**Figure 35: Maneuver boundaries for 6PAX aircraft.**

Thus, there are velocities and load factors for each of the aforementioned four conditions. Inserting these parameters into AVL program, it was possible to determine the aircraft bank angle and the trim angles for each of the control surfaces. From these results, the following Tables 25 and 26 have been set up. The colorful dots represent the conditions on V-n diagrams from Figure 36.



**Table 25 - Trim conditions for 4PAX aircraft.**

Condition	Velocity [m/s]	Altitude [ft]	$\rho_{air}$ [kg/m <sup>3</sup> ]	$n$	$\alpha$ [°]	$\delta_e$ [°]	$\phi$ [°]	$\delta_a$ [°]	$\delta_r$ [°]
● Coordinate Turn	64.6	ISA + 18°F	1.1839	2.7	5.34	-3.52	68.85	-4.41	11.63
● Dive at $V_D$	143.80	ISA + 18°F	1.1839	3.8	4.24	-3.55	0	0	0
● Dive at $V_C$	102.89	12000	0.6981	3.8	9.19	-8.20	0	0	0
● Bunt at $V_C$	102.89	12000	0.6981	-1.5	-4.99	4.19	0	0	0

**Table 26 - Trim conditions for 6PAX aircraft.**

Condition	Velocity [m/s]	Altitude [ft]	$\rho_{air}$ [kg/m <sup>3</sup> ]	$n$	$\alpha$ [°]	$\delta_e$ [°]	$\phi$ [°]	$\delta_a$ [°]	$\delta_r$ [°]
● Coordinate Turn	64.8	ISA + 18°F	1.1839	2.5	5.20	-3.16	66.27	-4.45	11.78
● Dive at $V_D$	143.63	ISA + 18°F	1.1839	3.8	4.87	-3.35	0	0	0
● Dive at $V_C$	102.89	12000	0.6981	3.8	10.39	-7.15	0	0	0
● Bunt at $V_C$	102.89	12000	0.6981	-1.5	-5.47	3.79	0	0	0

Having the aircraft trim conditions in hands, the next step was to calculate the lift and pitching moment distributions over the wing and empennage surfaces, for both aircraft. To do so, the aerodynamic analyses were evaluated through the software XFLR5, as illustrated in Figure 40 for the 4PAX configuration.

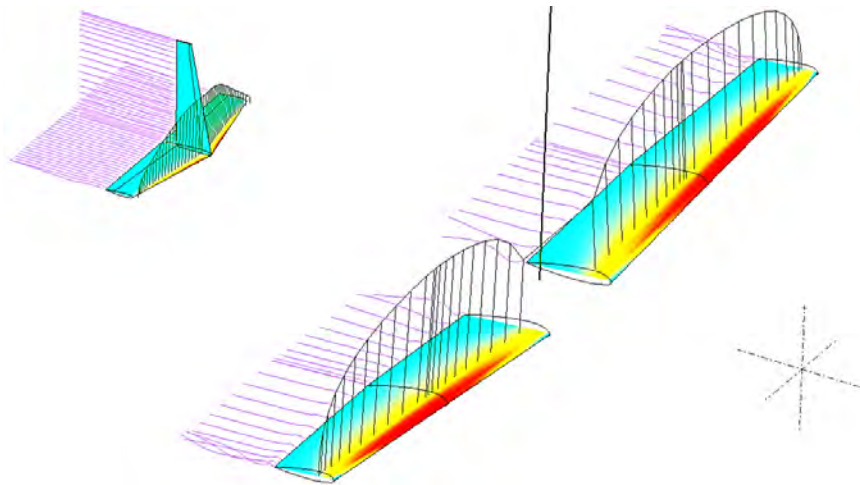


**Figure 36: Aerodynamic analysis in XFLR5.**

From these results, and using theory in [38], the bending and torsion moments over the wing and empennage span were calculated and presented in Figures 37 and 38.

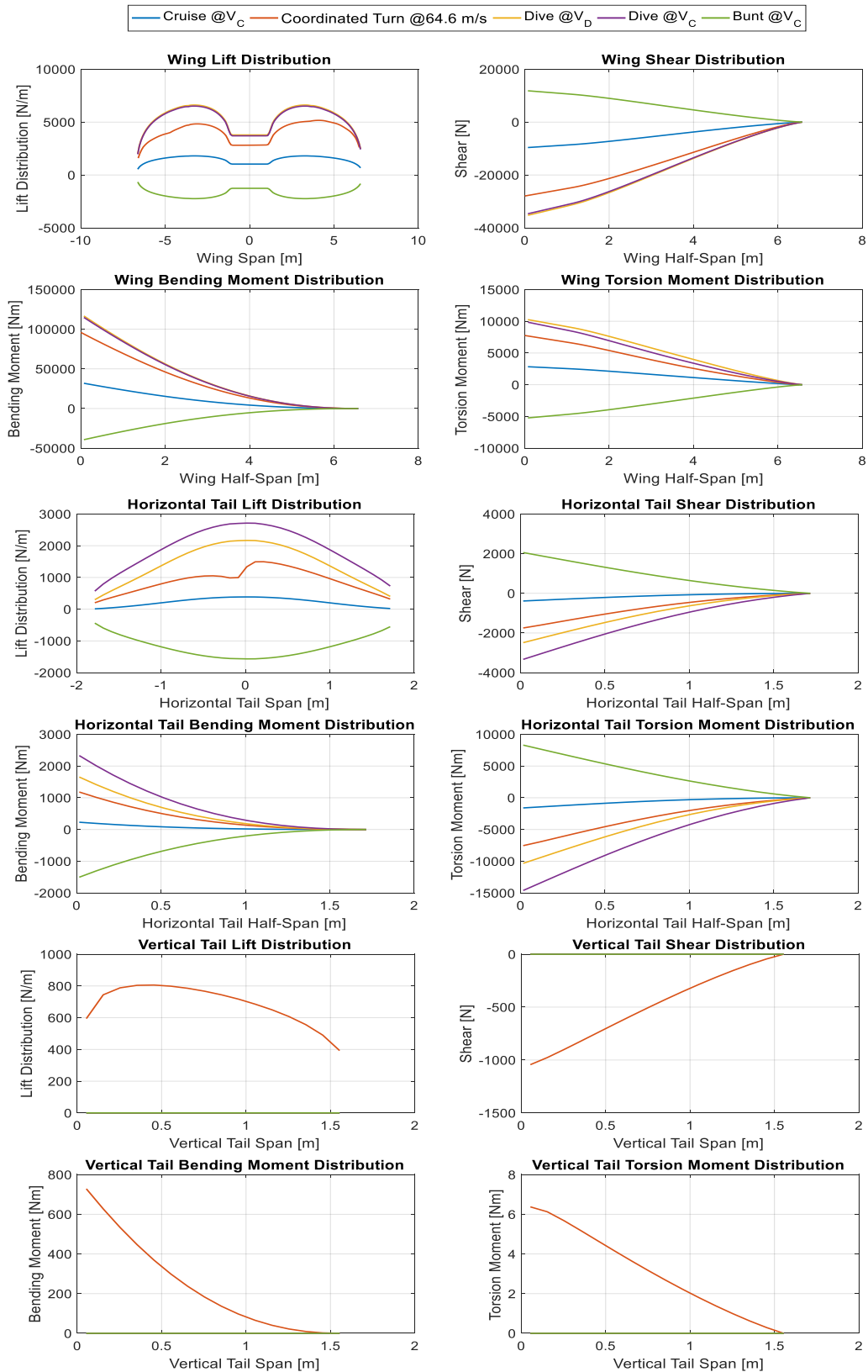


Figure 37: 4PAX aircraft loads.

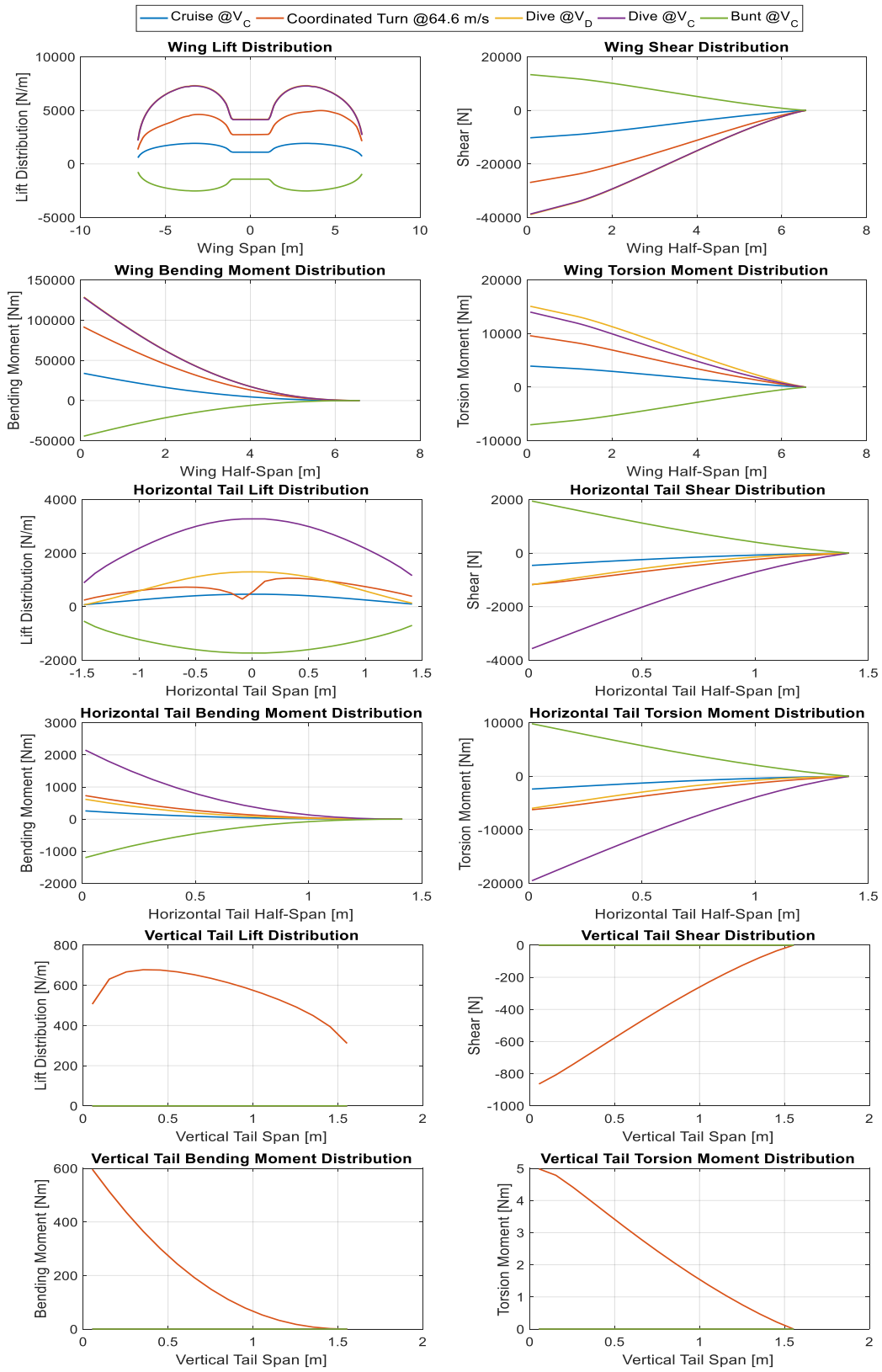


Figure 38: 6PAX aircraft loads.



## 7.1. Structural Wing Design

For the wing design, the number and position of spars, ribs and stringers were estimated using cutaway of conventional aircraft of same size.

The position and quantity of these elements were adapted to the actual aircraft's span and were not optimized due to the complexity of implementation, what led to the following coordinates, as shown in Figure 39.

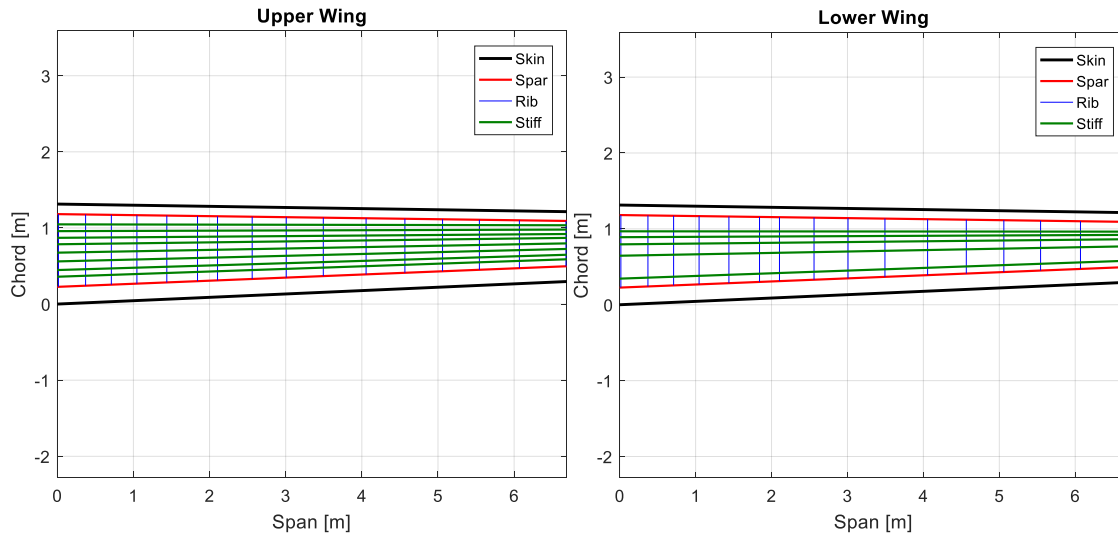


**Figure 39: Aircraft upper (on the left) and lower (on the right) wing structure elements along the span.**

Thus, an initial wing design was made using CATIA V5R21, so it was possible to refine the curvature and airfoil profile. Next, the model was exported to HyperMesh to create the mesh. The mesh size was designed in order to allow a satisfactory finite element analysis and to avoid an excessive computational consumption. Thus, it was used the quadrilateral-mesh with an element size of 30 mm, generating a mesh of 19885 elements. Moreover, for each rib it was created a RBE3 (rigid body element) to connect a single node to multiple nodes, allowing each rib to subject to a specific bending and torsion moments at 25% of the wing chord, depending on its location.

Having the model done, the wing structure was imported into Femap with NX Nastran, and groups of components were created to make the analyses easier.

To get started with the modeling, a material needed to be specified. For the entire model, the Aluminum 7050-T651 had been chosen due to its large applications and popularity in the aerospace industry. It is a heat treatable alloy that has very high mechanical properties and high fracture toughness, and offers good stress and corrosion cracking resistance and high strength at subzero temperatures. The Aluminum 7050-T651's general properties used in the model are presented in Table 27.



**Table 27: Aluminum 7050-T651 properties [58].**

Property	Value
Young's Modulus, $E$	72000 MPa
Poisson's Ratio, $\nu$	0.33
Mass Density, $\rho$	$2.7 \times 10^{-6}$ kg/mm <sup>3</sup>
Yield Strength, $\sigma_Y$	490 MPa

Coloring each component with a different color, representing different properties, the following full model is presented in Figure 40.

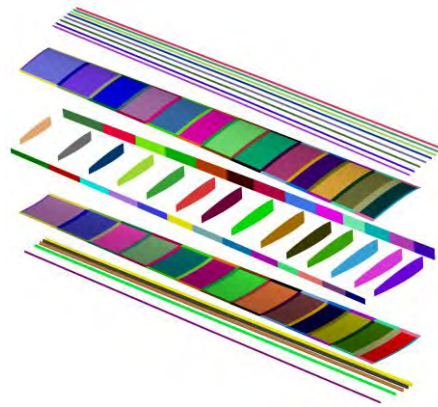


**Figure 40: Exploded wing and properties classified by colors.**

Next, it comes up with the static analysis of the wing. The load cases evaluated in this analysis are those presented in Table 28. Hence, for each load case it was necessary to determine and apply the specific loads in each RBE3. Thus, using the bending and torsion moments distributions from Figures 37 and 38, the loads were calculated and corrected for the actual Femap reference axes.

**Table 28: Load cases classifications in Femap.**

Load Case	Load Case Number	
	4PAX	6PAX
Dive at $V_C$	1	6
Dive at $V_D$	2	7
Bunt at $V_C$	3	8
Coordinate turn - RHS	4	9
Coordinate turn - LHS	5	10

Running the first static analysis for multiple load cases, the wing failed at these extreme conditions. Hence, the thicknesses of all elements in each group were manually modified so that the stresses throughout the wing were below 390 MPa, which is the Aluminum 7050's yield strength of 490 MPa with a safety factor of 1.2.



When analyzing the stress, the criteria of evaluation of the results were the maximum, minimum and shear stress for both plates and beams type elements. Thus, an envelope of results showing these stress values, for example, are presented in Figures 41, 42 and 43. On the right, it is displayed the stress values throughout all load cases, and on the left, it is displayed in which load case the maximum stress value was found.

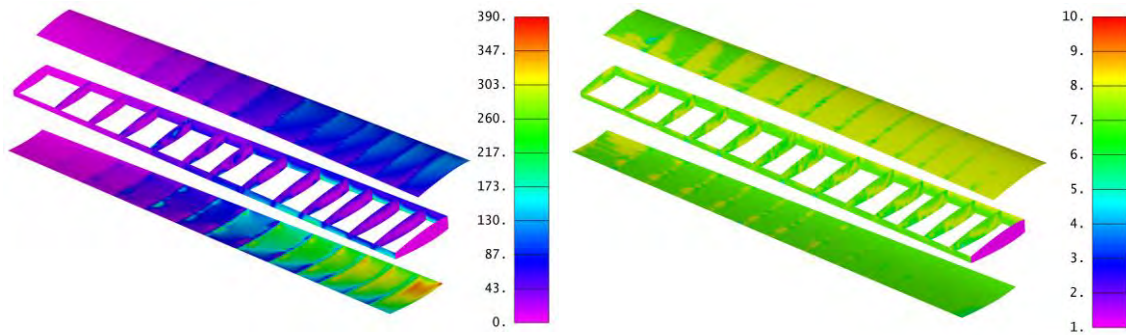


**Figure 41: Maximum stress values in MPa (on the left) and respective load cases envelope (on the right).**

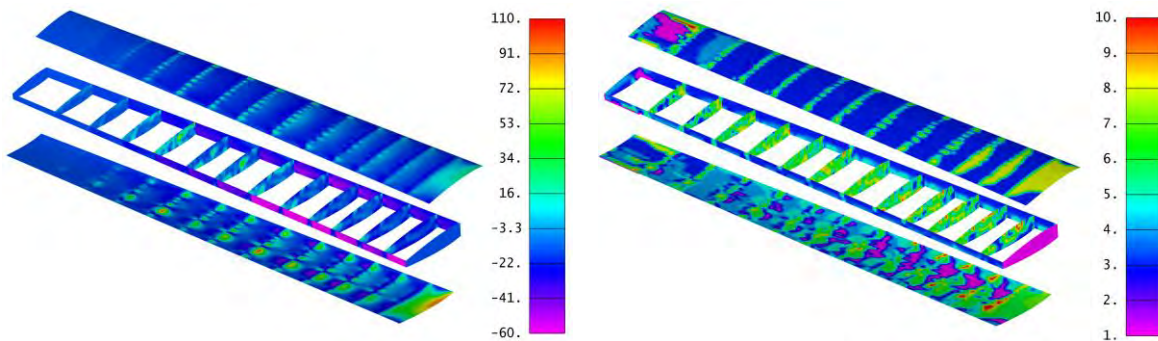


**Figure 42: Minimum stress values in MPa (on the left) and respective load cases envelope (on the right).**

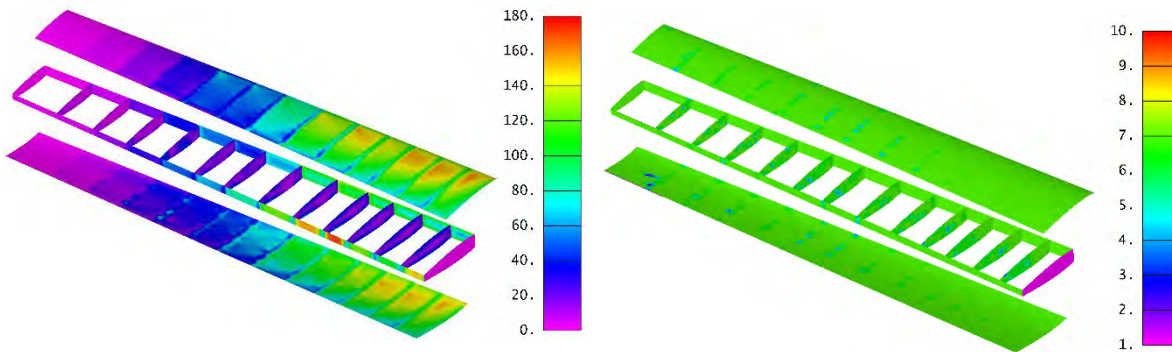


**Figure 43: Shear stress values in MPa (on the left) and respective load cases envelope (on the right).**

The stiffeners were modeled as beam type with a cross-section in “L”. Thus, they are not presented in Figures 41, 42 and 43, which show the results of the elements of plate type. However, it is worth pointing out that they were



also designed following the same process; in other words, changing cross-section dimensions and thicknesses. They are very important in the wing structural design because they increase the resistance of the skin panels, which is crucial against buckling. Therefore, the static analysis is not limited only to these stresses analyzes. Because of the high bending moments, the wing skins are subjected to high stresses of compression. Therefore, a buckling analysis is crucial to avoid any unforeseen phenomena.

When running a Femap buckling analysis, the software shows what percentage of the current loads would be sufficient to buckle any part of the structure. Thus, the first buckling analysis in Femap showed that some skin plates, for example, would fail at 45.5% of those current loads, as presented in Figure 44.

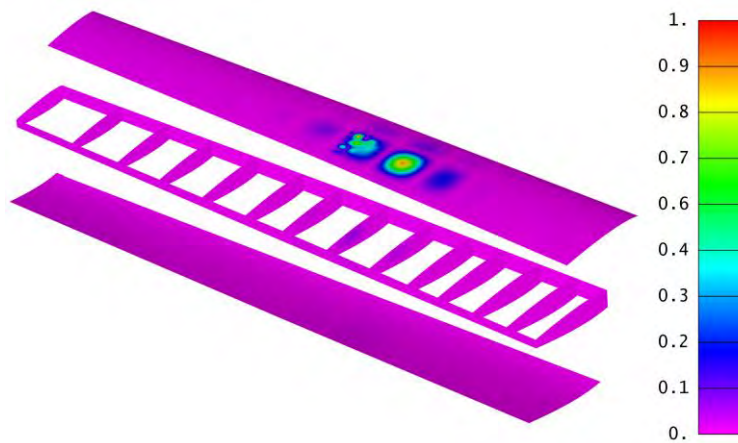


**Figure 44: Wing buckling analysis with failure at 45.5% of current loads.**

After analyzing all the eigenvectors, new thicknesses were manually inserted into the properties of the elements involved, until the buckling analyses showed no failure. Finally, the wing structure is well dimensioned for the evaluated loads and buckling analyses. The thickness distribution along the wing is shown in Figure 45.

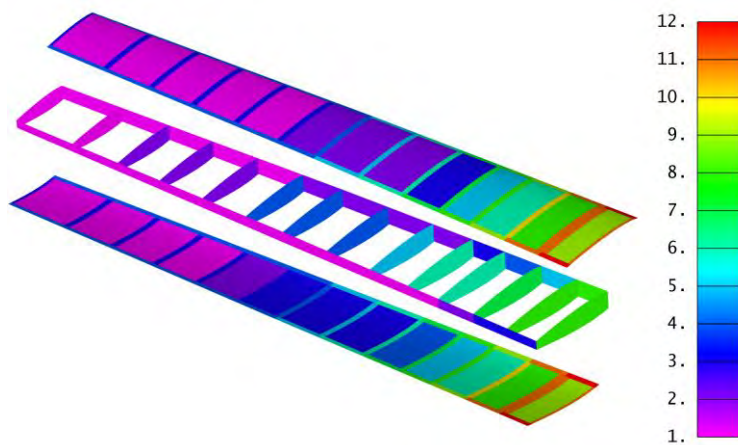


**Figure 45: Thickness distribution along the wing [mm].**



The current wing has a weight of 154.84 kg. This weight could be optimized and reduced changing the thickness, geometry, location and quantity of each element (skin, ribs, stiffeners and spars) throughout the wing. However, this has not been done because of the complexity and computational processing time that would spend. Alternatively, a new material proposal has been discussed and analyzed: the carbon fiber epoxy Hexcel 8552 NMS 128/2. Its properties are listed in Table 29.

**Table 29: Composite material (Hexcel 8552 NMS 128/2) properties [39].**

Property	Value
$E_{11}$	148 GPa
$E_{22}$	10.3 GPa
$\nu_{12}$	0.27
$G_{12}$	5.9 GPa
$G_{23}$	5.9 GPa
$G_{13}$	5.9 GPa
$X_{1t}$	2439 MPa
$X_{2t}$	66 MPa
$X_{1c}$	2013 MPa
$X_{2c}$	381 MPa
$S_{12}$	78 MPa
$S_{\text{Bonding}}$	34.7 MPa
$\rho$	1577 kg/m <sup>3</sup>

The carbon-epoxy plates are made of laminates with 0.2 mm of thickness, and their orientation start with 0° and varies with an increment of 45° for each layer. Thus, different plates were created following this pattern. Next, following the same process presented previously, the static analysis for the multiple set of critical load cases was evaluated for the new wing of composite material.

When analyzing structures in composite, it is not the maximum and minimum stress that are evaluated. Now it is the Tsai-Wu failure criterion [40]. Thus, an envelope of the results of this analysis using this composite fail criterion is presented on the left in Figure 46. The ribs were not substituted to composite material due to the high compression loads they are subjected to. Hence, when they were analyzed in composite, the thickness required to withstand the loads would be huge, resulting in a weight much greater if it were used aluminum. Therefore, they were kept in aluminum to save more weight. Their analysis is presented in the right in Figure 46.

The thicknesses of each element were manually readjusted in order to avoid any composite material failure. Next, a new buckling analysis was performed to ensure all elements were safe. The result of this analysis showed that some skin of composite material, for example, would fail for those current loads. Setting for the last time the elements'



thicknesses, the buckling failures were fixed. Therefore, a final designed wing is obtained, which is presented in Figure 47. The final wing weight is 115.21 kg, saving 39.63 kg when using composite material.

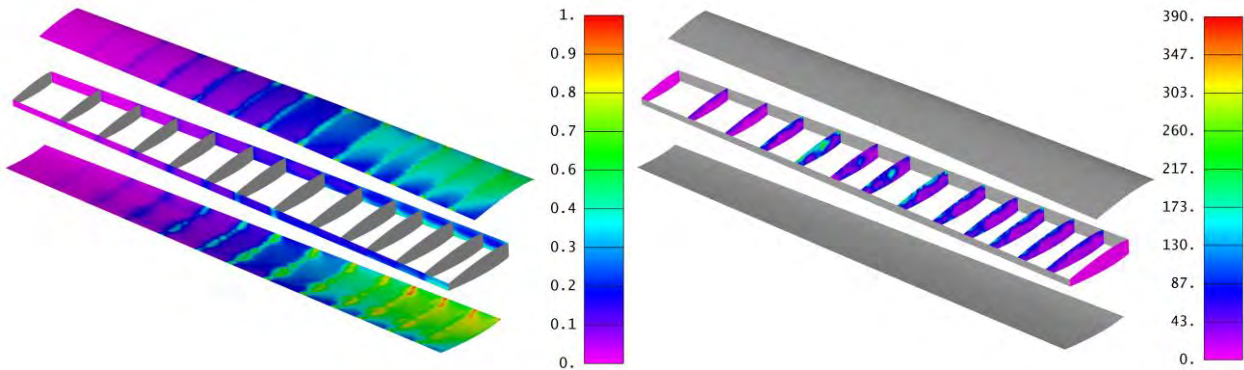


Figure 46: Tsai-Wu failure criterion analysis (on the left) and ribs maximum stress [MPa] (on the right).

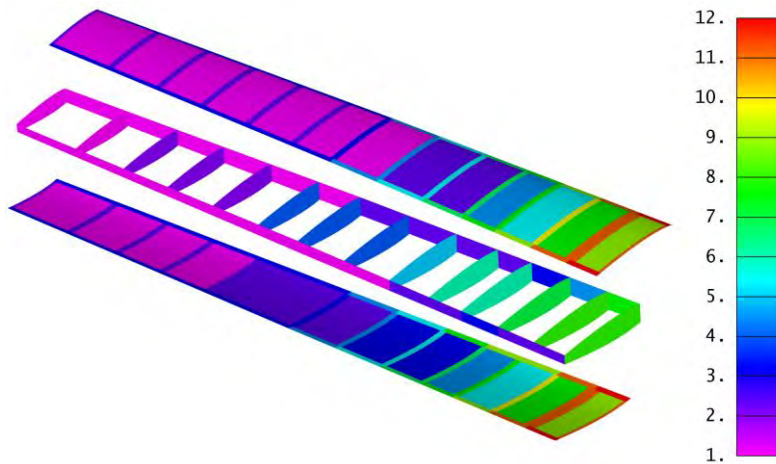
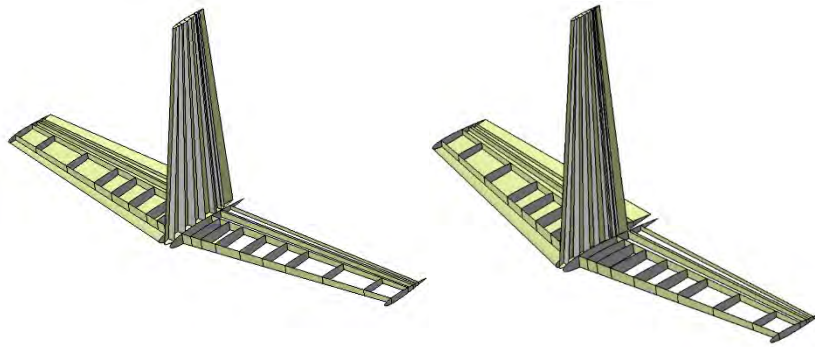


Figure 47: Final thickness distribution of the composite material layers along the wing structure [mm].

From Figure 47, it is noticed that the layers at the root are very thick. This is necessary because the wing has a high AR and there is a large stress concentration in that region. This is a recurring issue on wings like that, but its reduction of aerodynamic drag, specifically induced drag, justifies its application.

## 7.2. Structural Empennage Design

The empennage design followed the same project philosophy presented in Section 7.1. for the wing design. The horizontal tail comprises ribs and spars, while the vertical tail is a multiple spars structure. Each one of the aircraft (4PAX and 6PAX) has a different empennage, because each aircraft has different fuselage lengths and wing positions, what implies in different empennage sizes. Therefore, for each aircraft configuration it was designed in CATIA a specific vertical and horizontal tail, as presented in Figure 48. Their dimensions are available in Table 15.



**Figure 48: Empennages of the 4PAX (on the left) and 6PAX (on the right) aircraft.**

### 7.2.1. Structural Horizontal Tail Design

Similar to the structural wing design, the initial horizontal tail models for both aircraft were made using CATIA V5R21, so it was possible to refine the curvatures and airfoil profiles. Next, the models were exported to HyperMesh to create the meshes. The mesh size was designed in order to allow a satisfactory finite element analysis and to avoid an excessive computational consumption. Thus, it was used the quadrilateral-mesh with an element size of 10 mm, generating a mesh for the horizontal tails of 21274 elements for the 4PAX and 19456 elements for the 6PAX. Having the models done, they were imported in Femap with NX Nastran. Likewise in wing design, the Aluminum 7050-T651 was initially chosen as the material for both horizontal tails.

Therefore, coloring each component with a different color, representing different properties, the following full models are shown in Figure 49. The load cases evaluated in this analysis are those presented in Table 28. The static analysis for both horizontal tails was performed equally to the wing case, as presented in Section 7.1. In other words, the thicknesses were readjusted during the entire process, so the structures did not fail, even for buckling. The final designed horizontal tails in aluminum have a weight of 15.63 kg and 15.39 kg, for the 4PAX and 6PAX respectively.

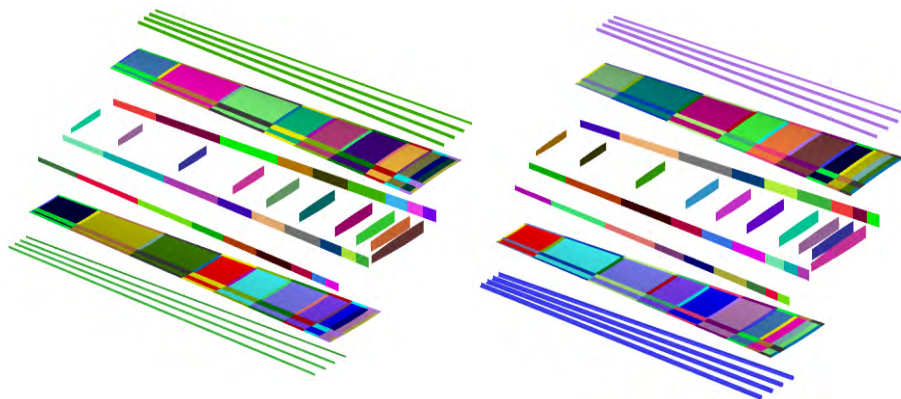


**Figure 49: 4PAX (on the left) and 6PAX (on the right) horizontal tails with properties classified by colors.**



Next, the material was substituted for the same composite used in Section 7.1, the Hexcel 8552 NMS 128/2. When the wing structure was designed, the ribs were not substituted to composite material due to the high compression loads, so they were kept in aluminum. Now, both empennage ribs presented good results when applied composite material, so they were kept in carbon-epoxy.

Thus, once more both structures were redesigned changing the thickness and appliance of layers in each element group so that they meet all the fail criteria. The Tsai-Wu failure criteria envelopes of results are displayed in Figures 50 and 51, for 4PAX and 6PAX, respectively.

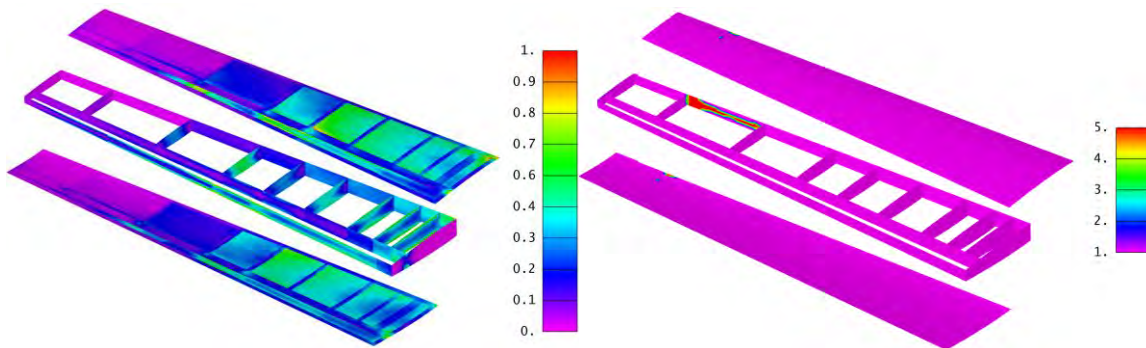


**Figure 50: Tsai-Wu failure criterion (on the left) and load cases (on the right) for the 4PAX horizontal tail.**

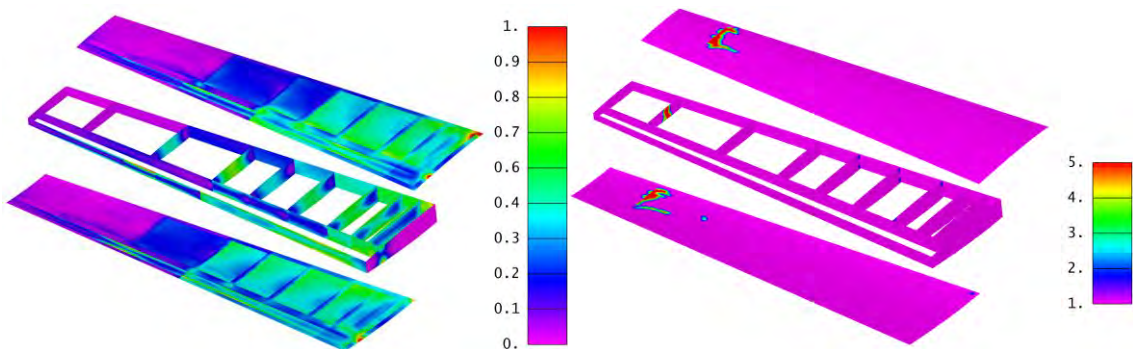


**Figure 51: Tsai-Wu failure criterion (on the left) and load cases (on the right) for the 6PAX horizontal tail.**

Next, the buckling analysis was performed for both horizontal tails. Since some elements were failing, the thicknesses were increased until the structures did not fail anymore.

Finally, both horizontal tails are well designed for the current loads, resulting in the following thickness distributions, presented in Figure 52. The change of material from aluminum to composite resulted in a reduction of 4.36 kg and 4.65 kg for 4PAX and 6PAX, respectively. Therefore, they ended weighting 11.27 kg and 10.72 kg, respectively.

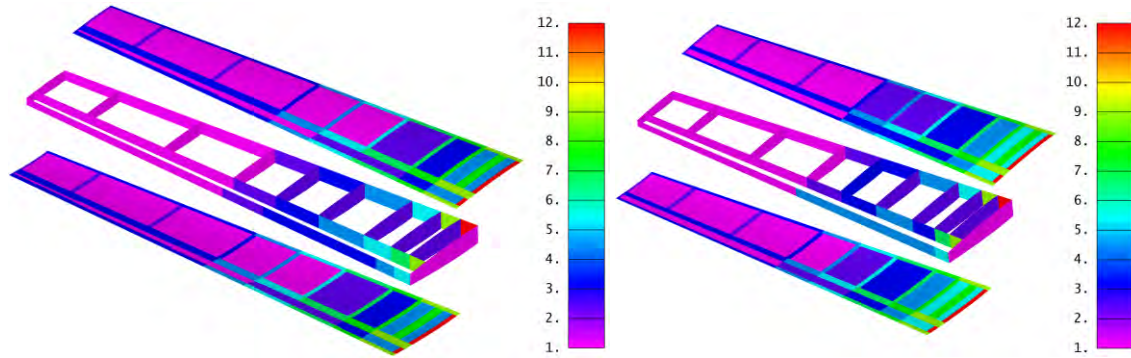


**Figure 52: Final thickness distribution [mm] of the composite material layers along the 4PAX (on the left) and 6PAX (on the right) horizontal tails.**

The horizontal tails, in addition to concentrating stresses at the root due to the high load values, also suffer with the influence of twisting, unlike the wing structure. It is possible notice that the sixth rib (counting from the root) is thicker than the root due to the twist in that location.

### 7.2.2. Structural Vertical Tail Design

The same process used for the horizontal tails has been used here. Thus, after drawing the structures on CATIA and creating the mesh on HyperMesh, the models were exported to Femap with NX Nastran, resulting in the following full models presented in Figure 53.

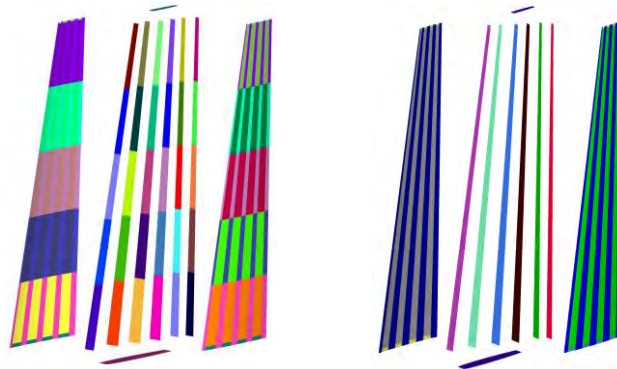


**Figure 53: 4PAX (on the left) and 6PAX (on the right) vertical tails exploded and properties classified by colors.**

Next, assuming the structures in aluminum, it was evaluated the load cases as done before, resulting in vertical tails of weight of 5.72 kg and 4.23 kg, for the 4PAX and 6PAX respectively. Later on, the material was substituted for the same composite used in Section 5.1, the Hexcel 8552 NMS 128/2. Thus, once more both structures were redesigned changing the thickness and appliance of layers in each element group so that they meet all the fail criteria. The Tsai-Wu failure criteria envelopes of results are displayed in Figures 54 and 55, for 4PAX and 6PAX, respectively.

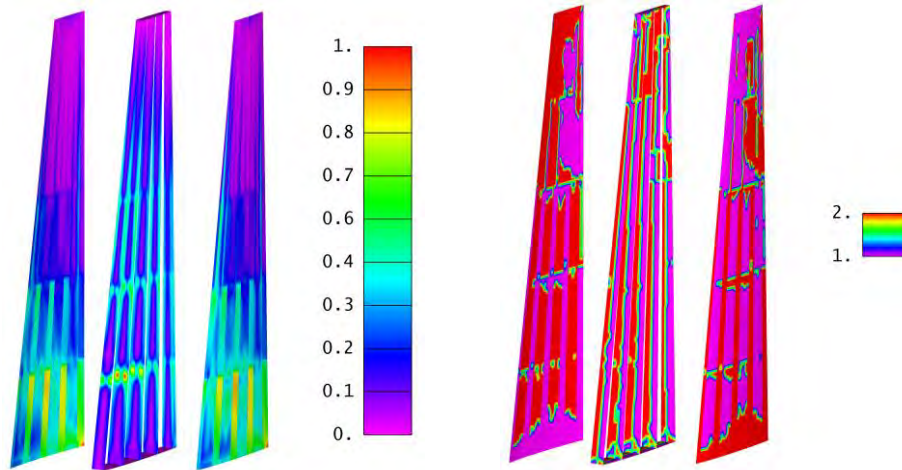


**Figure 54: Tsai-Wu failure criterion (on the left) and load cases (on the right) for the 4PAX vertical tail.**

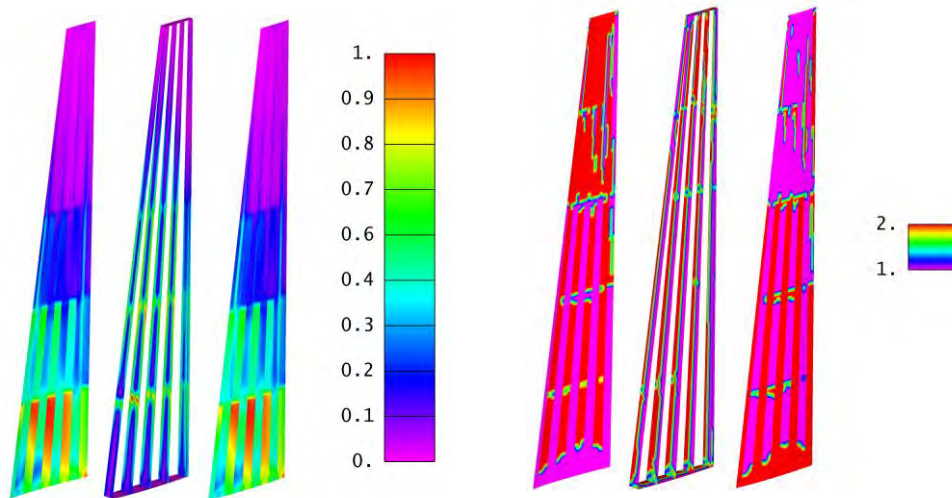


**Figure 55: Tsai-Wu failure criterion (on the left) and load cases (on the right) for the 6PAX vertical tail.**

Next, the buckling analysis was performed for both vertical tails. Since some elements were failing, the thicknesses were increased until the structures did not fail anymore. Finally, both vertical tails are well designed for the current loads, resulting in the following thickness distributions, presented in Figure 56. The change of material from aluminum to composite resulted in a reduction of 2.26 kg and 1.28 kg for 4PAX and 6PAX, respectively. Therefore, they ended weighting 3.46 kg and 2.95 kg, respectively.

The vertical empennage thicknesses ended thinner because the loads applied to the rudder are relatively lower and its size is relatively small. Its structure is made of multiple spars, increasing considerably its resistance to bending, which is the main stress the rudder is subjected to.

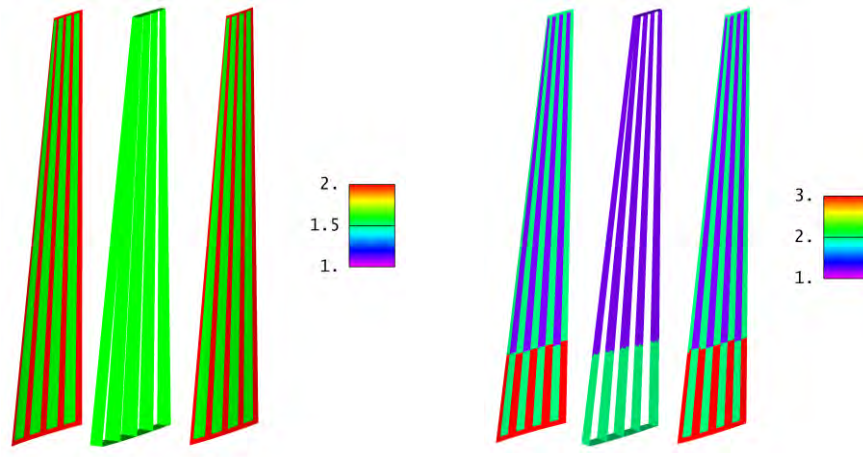


**Figure 56: Final thickness distribution of the composite material layers along the 4PAX (on the left) and 6PAX (on the right) vertical tails.**

### 7.3. Summary Results of Structural Analysis

Having the results presented in Sections 7.1 and 7.2, a summary of components and their respective critical stress and buckling conditions are displayed in Tables 31 and 32.

**Table 30: Summary of stress results of structural components in aluminum.**

Component	Load Case	Tensile Strength [MPa]	Margin of Safety
Wing	Dive $V_D$	352.00	0.2816
HT 4PAX	Dive $V_c$	333.60	0.3192
HT 6PAX	Dive $V_c$	382.40	0.2196
VT 4PAX	Coordinate Turn - LHS	265.90	0.4573
VT 6PAX	Coordinate Turn - LHS	288.10	0.4120

**Table 31: Summary of Tsai-Wu failure criterion of structural components in composite material.**

Component	Load Case	Failure Index (Tsai-Wu )	Buckling Margin of Security
Wing	Dive $V_d$	0.98	6.30%
HT 4PAX	Dive $V_c$	0.94	4.50%
HT 6PAX	Dive $V_c$	0.96	6.40%
VT 4PAX	Coordinate Turn - LHS	0.91	38.60%
VT 6PAX	Coordinate Turn - LHS	0.89	48.00%

### 7.4. Structural Fuselage Design

The structural design of the fuselage was based on conventional aircraft of same size. 28 stiffeners and 39 frames were used and distributed throughout the fuselage. The stiffeners were modeled as beam type with a cross-section in “L”. The frames in the middle part of the fuselage were arranged to coincide with the spars of the wing. Likewise, in the rear part they were arranged to coincide with the spars of the empennage to form the joint more smoothly.



Next, the structural mesh was created using HyperMesh. The size of the element created was 30 mm, being refined in the parts of tension concentration. A mesh of 38284 elements was obtained. RBE3 rigid elements have also been created in the position of each frame, where the loads will subsequently be applied. Figure 57 shows blue RBE3 created.

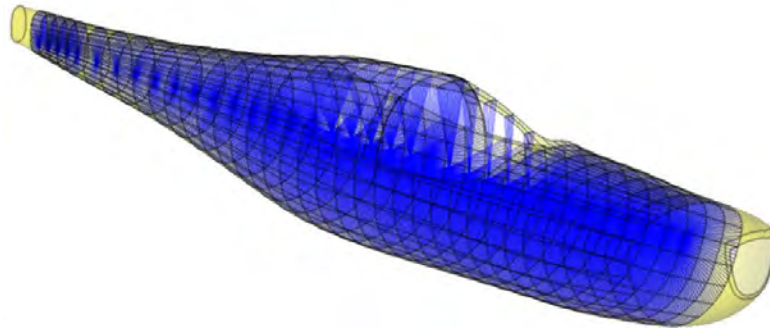


**Figure 57: 4PAX fuselage rigid elements.**

In order to obtain the force distribution  $Q$  and the momentum  $M$  in the fuselage, the Discretized Fuselage model proposed by [41] was used. It was considered the critical case of dive recovery presented in Section 7. Figure 58 shows the charge distribution for the 4PAX fuselage.

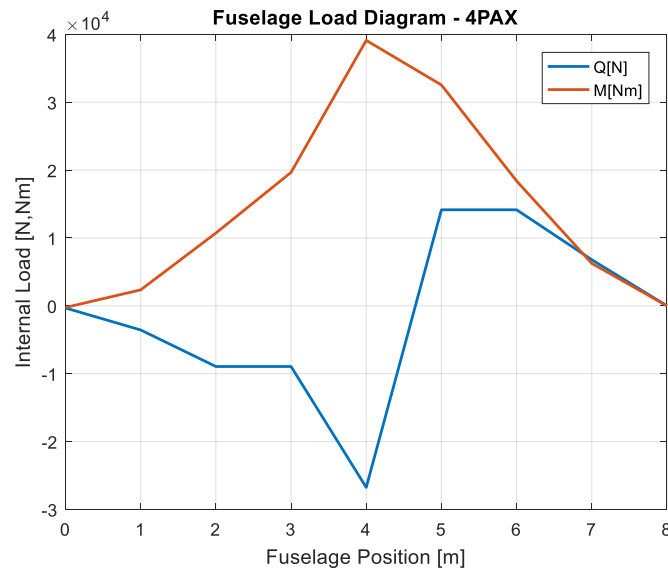


**Figure 58: 4PAX fuselage loads.**

Finally, the mesh and loads were applied in Femap to create the finite element model. When analyzing the stress, the criteria of evaluation of the results were the maximum, minimum and shear stress for both plates and beams type elements. The results are presented in Figures 59 and 60.

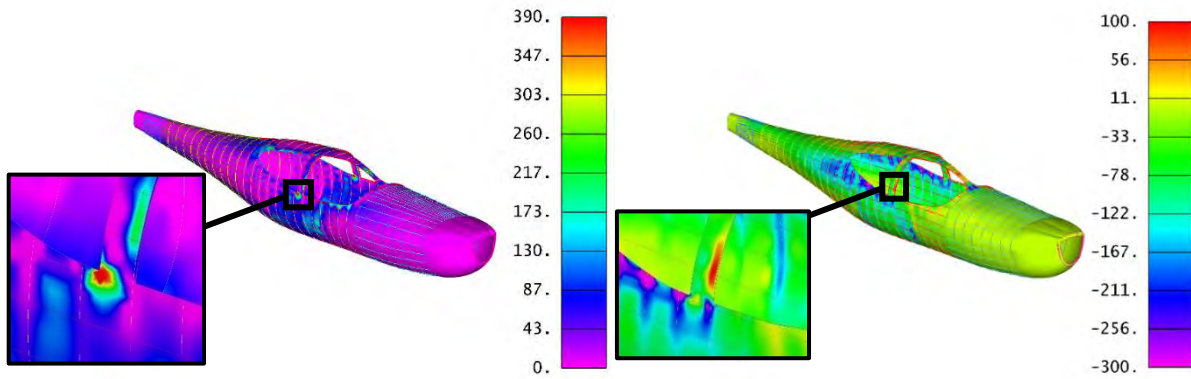


**Figure 59: Maximum (on the left) and minimum (on the right) stress values envelope in MPa.**

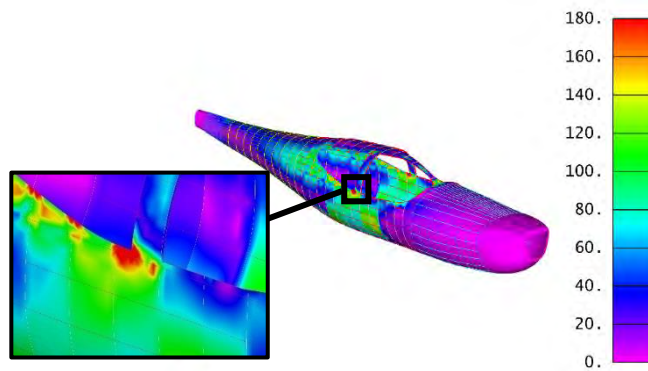


**Figure 60: Shear stress values envelope in MPa.**

Then the buckling analysis was performed, where the application of 101.45% would create the first case of buckling, as shown in Figure 61.

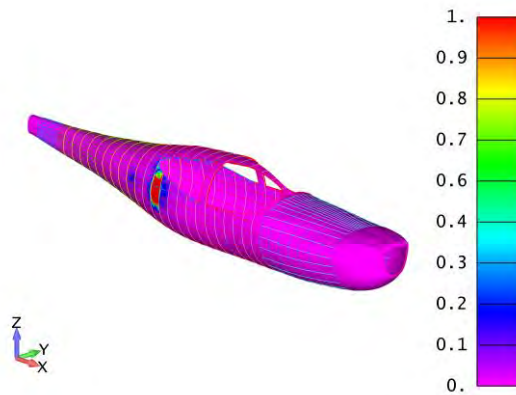


**Figure 61: Fuselage buckling analysis with failure at 101.45% of current loads.**

Finally, the fuselage is well designed and dimensioned for the evaluated loads and buckling analyses. The thickness distribution along the fuselage is shown in Figure 62.

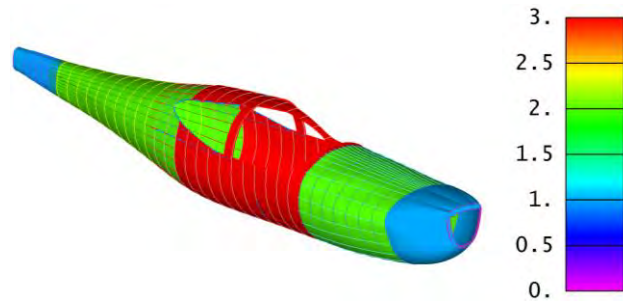


**Figure 62: Thickness distribution along the fuselage [mm].**

As seen in figures above, the most critical regions of the fuselage are at the edge of the windows. Therefore, the reinforcers used in this region had to be increased to support, mainly, cases of buckling in this region.

### 7.5. Final Material Composition

After designing the wing, the fuselage, and the vertical and horizontal tails, a final material composition of the aircraft's main components is displayed in Figure 63.

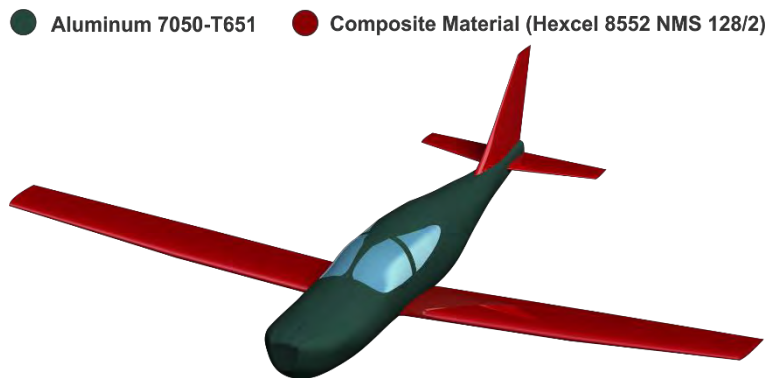


**Figure 63: Material composition of the aircraft.**

## 8. Aeroelastic Analysis

This section presents an aeroelastic analysis of the wing designed in Section 7.1. Firstly, it was evaluated the displacement and rotation values for the carbon-epoxy wing in order to estimate its flexibility when applying the loads specified in Table 28. These values are displayed in Figure 64.

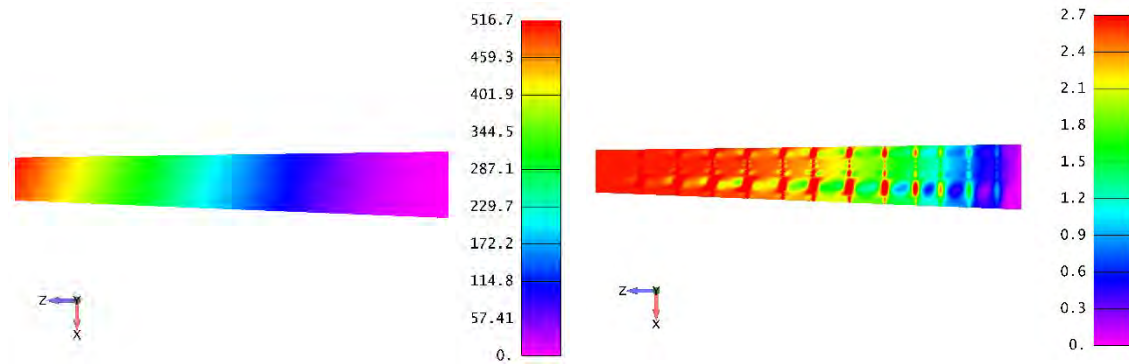


**Figure 64: Total displacements in mm (on the left) and total rotation in degrees (on the right) for the carbon-epoxy wing when applying the loads from Table 29.**

According to literature [41], the displacement presented in Figure 69 are among the theoretical values expected for this type of wing. However, the rotation values are much lower, which is curious. It is explained basing on how the wing has been designed.

A bunch quantity of ribs in aluminum was applied in the structure. Hence, an improved torsion resistance is obtained. If an optimization had been implemented, probably it would be necessary less ribs in the wing design.

Next, a modal analysis of the wing model was firstly performed in Femap in order to find the natural frequencies, which are presented in Table 32. The first four modes are mostly bending-modes, as observed in Figure 65. The twisting-mode only shows up in the fifth mode (Figure 66), which is explained by high strength of the wing related to torsion moments, as mentioned before.

**Table 32: Natural frequencies obtained from wing modal analysis.**

Mode Shapes	Natural Frequencies (Hz)
1	10.66
2	32.80
3	43.04
4	90.27
5	100.03
6	125.84
7	129.43
8	141.03
9	142.25
10	183.44

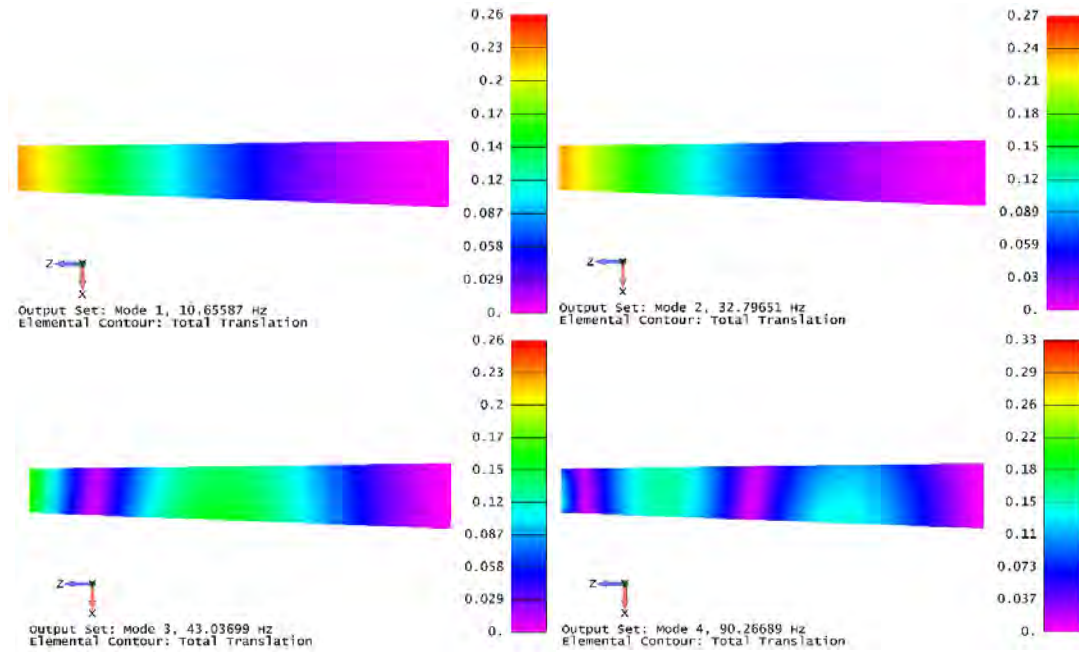


**Figure 65: First four mode shapes of the wing.**

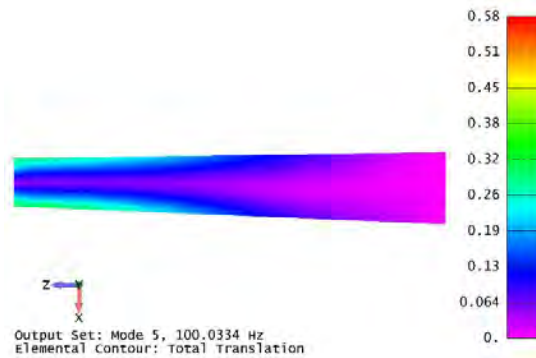


**Figure 66: Fifth mode shape of the wing.**

Next, a divergence and flutter analysis was performed using the NX Nastran SOL 145. First of all, the aerodynamic mesh was created to emulate the air flow through the wing.

The association of both aerodynamic and structural meshes was made through a SPLINE1 connection on the nodes that intersect the following structures: upper skin, ribs and stiffeners. This allows to distribute the aerodynamic loads over the entire wing elements, similarly to the RBEs in the structure design presented in Section 7.1.

Moreover, it was considered the first five mode shapes of the structure, and method used was PK-NL. The air density of  $0.818 \text{ kg/m}^3$  was the equivalent of a flight altitude of 12000 ft (cruise), and the density of reference was taken at sea-level (ISA +  $10^\circ\text{C}$ ). The airspeed was evaluated from 20 to 200 m/s TAS, representing the flight speed envelope of the aircraft. This analysis released the following results, presents as V-g-f plots in Figure 67.

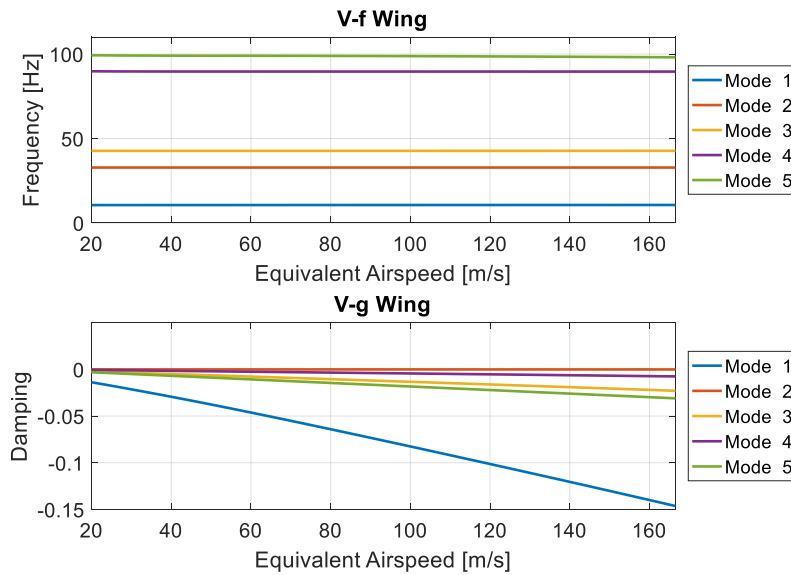


**Figure 67: V-g-f diagram for the aircraft velocities envelope.**

Analyzing the V-g and V-f plots, there is no flutter and divergence phenomenon for the aircraft velocities envelope. This is due to the high natural frequencies and mode shapes that need very high speed to couple and, consequently, bring the system do instability. In addition, the composite material (Hexcel 8552 NMS 128/2) applied contributes to increase the stiffness of the wing, improving the aeroelastic responses.

To verify when the instabilities occur, the interval of velocities was expanded to 1000 m/s TAS. Hence, a new analysis was evaluated, resulting in the following V-g-f plots presented in Figure 68.

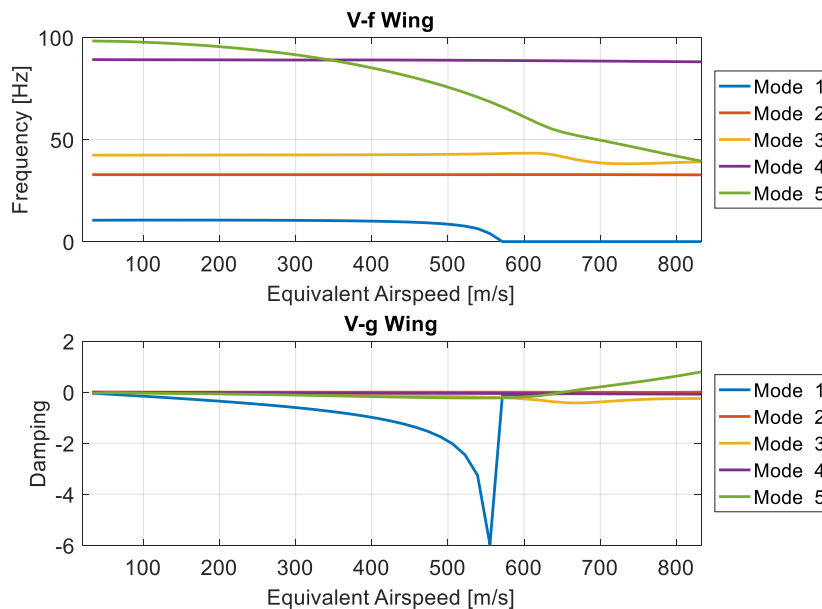


**Figure 68: V-g-f diagram for the expanded aircraft velocities envelope.**



Now, it is possible to observe the flutter showing up at 650 m/s EAS, where the third (bending) and fifth (twisting) modes are coupled, as shown in V-f plot. Consequently, the damping of mode 5 becomes positive ( $g > 0$ ) at this speed, as presented in V-g plot. The flutter speed is very high because the wing structure has a great strength, delaying the coupling of natural frequencies of the bending and twisting modes.

## 9. Modal Analysis of the Aircraft

The first four natural frequencies of the entire aircraft were analyzed in Femap. The frequencies found were 5.77 Hz, 9.16 Hz, 14.14 Hz and 15.95 Hz, and the mode shapes are shown in Figure 69.

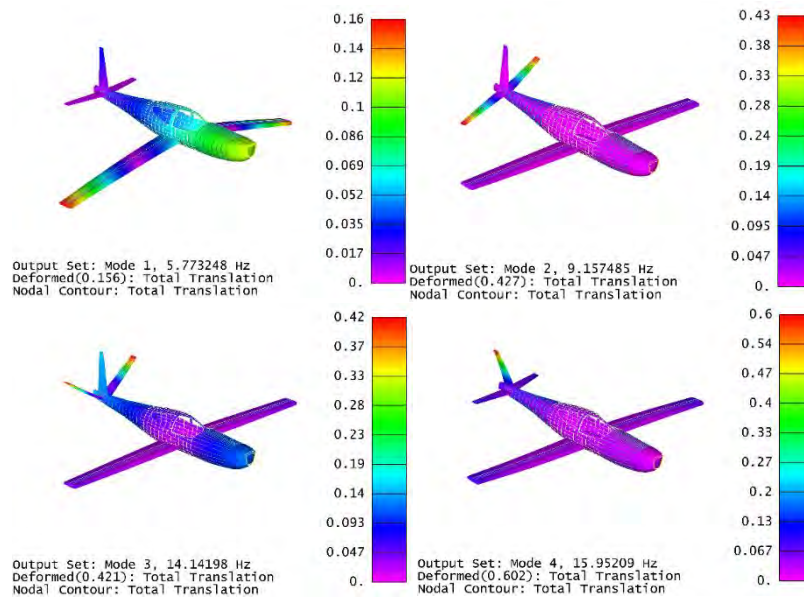


**Figure 69: First four mode shapes of the aircraft.**

Due to simplifications used in the joint with the fuselage, it was observed that the wing and empennage have an almost totally rigid behavior in the vibration modes.

## 10. Stability Analysis

### 10.1. Longitudinal Static Stability

For the analysis of longitudinal stability for both aircraft, a study of the influence of the wing, elevator, drag of the wing and propeller in the  $C_m$  of the aircraft was performed, as shown in Figure 70. As expected, the wing and its drag had a negative influence on the  $C_m$  of the aircraft, unlike the elevator and the propeller. As a sum of each of these influences, the  $C_m$  vs. AoA plots are obtained and shown in Figure 71.



In addition, the study of the trim angle of the elevator was carried out in relation to the airspeed of the aircraft (Figure 72). The results were satisfactory considering the speed envelope of operation of the aircraft.

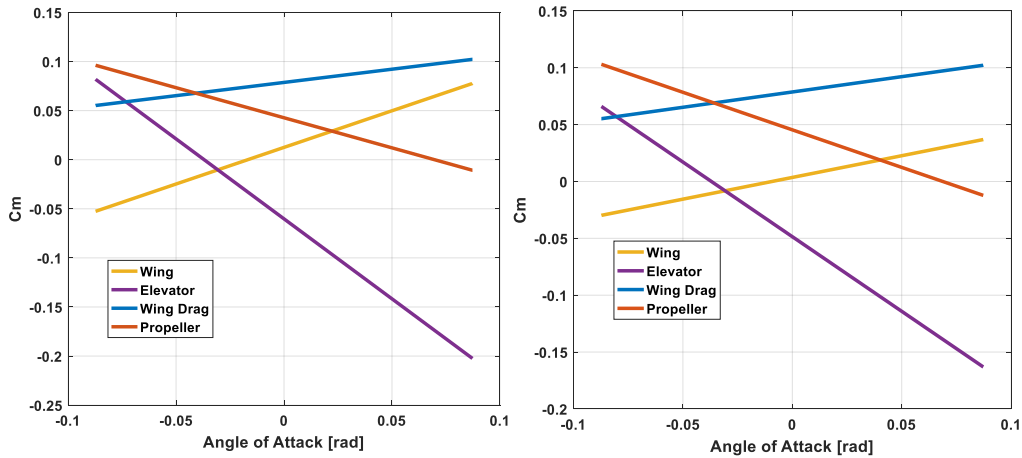


Figure 70: Longitudinal Static Stability of both aircraft: 4PAX (on the left) and 6PAX (on the right).

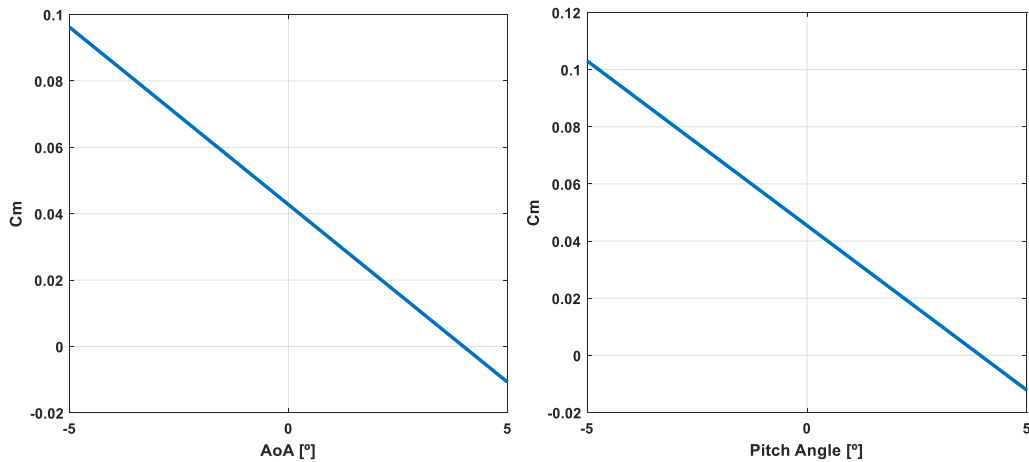


Figure 71: Cm x Alpha for both aircraft: 4PAX (on the left) and 6PAX (on the right).

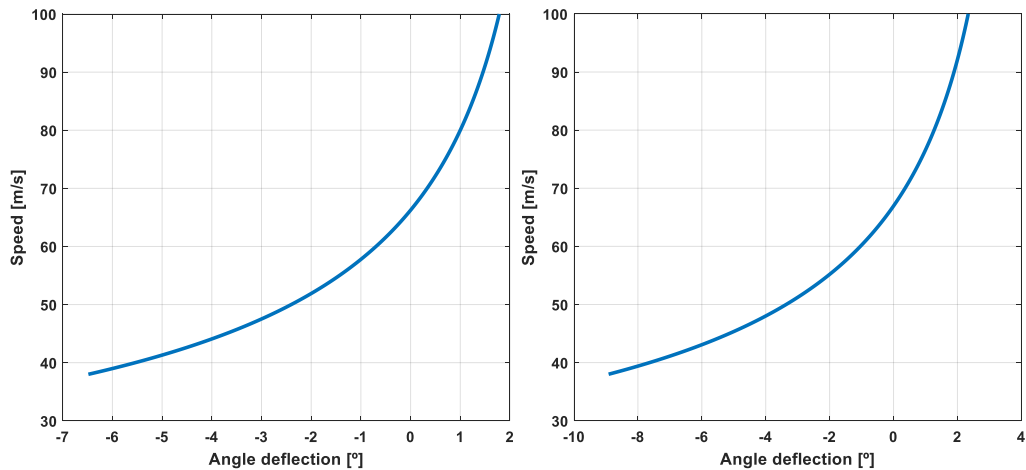


Figure 72: Elevator deflection angle vs Speed for both aircraft: 4PAX (on the left) and 6PAX (on the right).



Thus, the static margins for both aircraft were obtained and are presented in Table 33.

**Table 33: Static margin results for both aircraft.**

Aircraft	$Cm_\alpha$	Static Margin
4PAX	-0.6127	11,50%
6PAX	-0.3827	12,40%

## 10.2. Lateral-Directional Static Stability

The first analysis was the rudder and aileron trimming for lateral cross winds as shown in Figure 73. Next, it was analyzed the rudder and aileron trimming during a coordinate curve of radius of 1000 m, and the results are shown in Figure 74. Finally, the behavior of the rudder and aileron to perform the specified coordinate is shown in Figure 75.

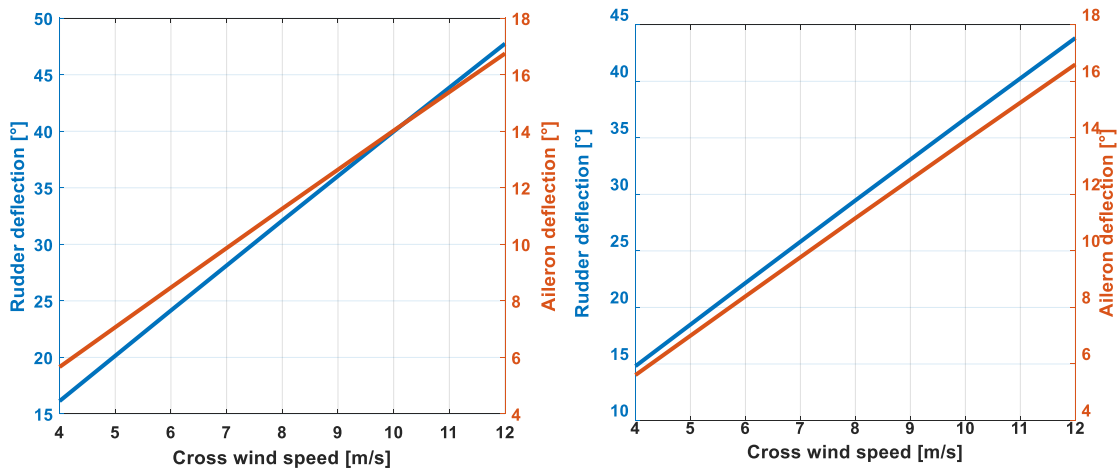


**Figure 73: Rudder and aileron deflection at trimming condition for 4PAX (on the left) and 6PAX (on the right).**

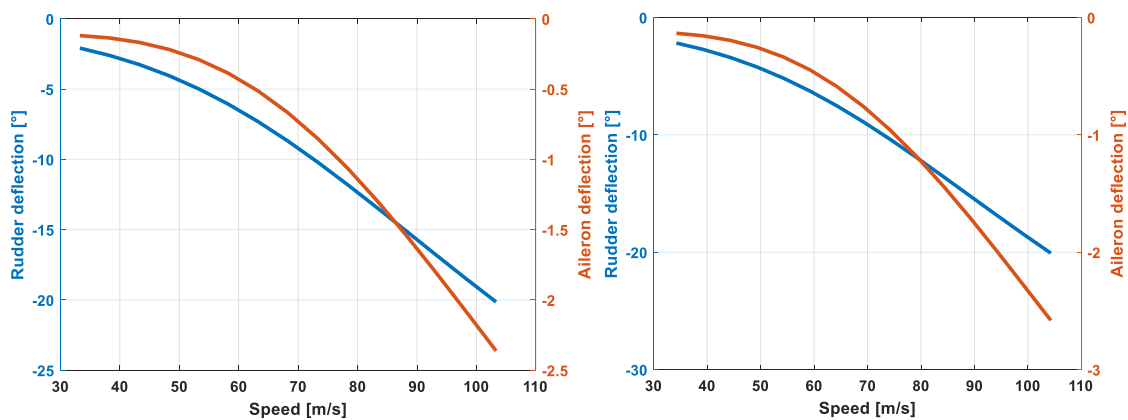


**Figure 74: Rudder and aileron trimming at coordinate curve for 4PAX (on the left) and 6PAX (on the right).**

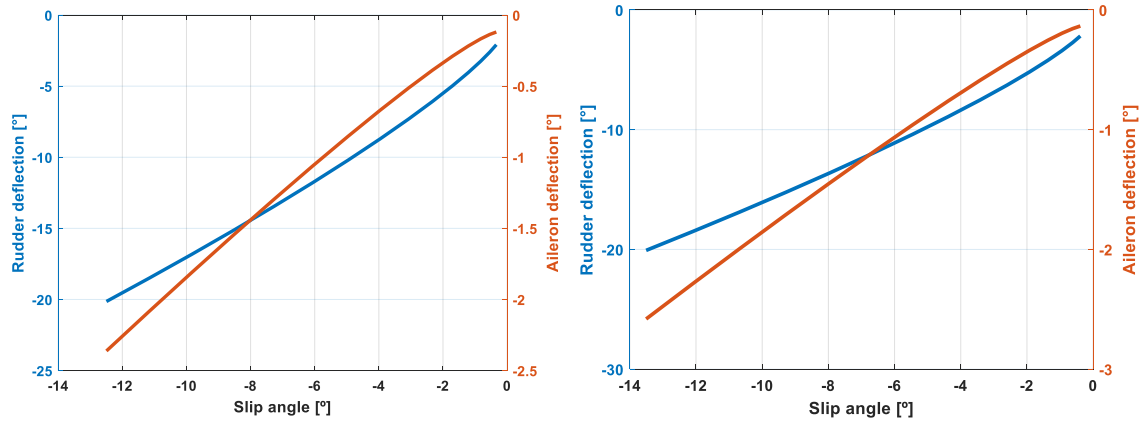


**Figure 75: Rudder and aileron deflections vs. Slip angle for 4PAX (on the left) and 6PAX (on the right).**

### 10.3. Longitudinal Dynamic Stability

The dynamic stability analyses were performed for both aircraft, and all results were satisfactory. However, only the results for the 4PAX aircraft will be presented here.

Firstly, it was evaluated the phugoid mode for the entire flight envelope. The results are very satisfactory and are presented in Figure 76. It shows the behavior analysis at sea-level and at service ceiling (FL120). Moreover, Figure 77 shows that the quality of flight meet the comfort conditions specified by the MIL-F-8785C, demonstrating that the aircraft meets the requirements of longitudinal dynamic stability.

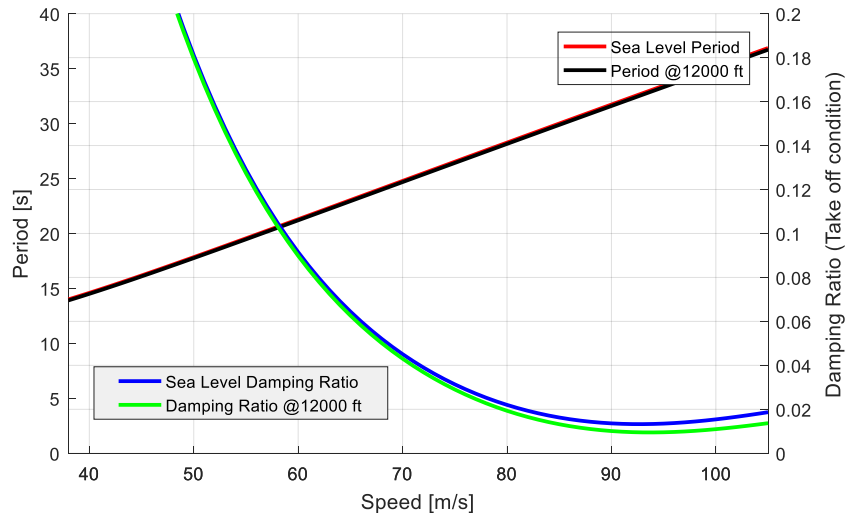


**Figure 76: Variation of phugoid mode over the 4PAX aircraft operation envelope.**

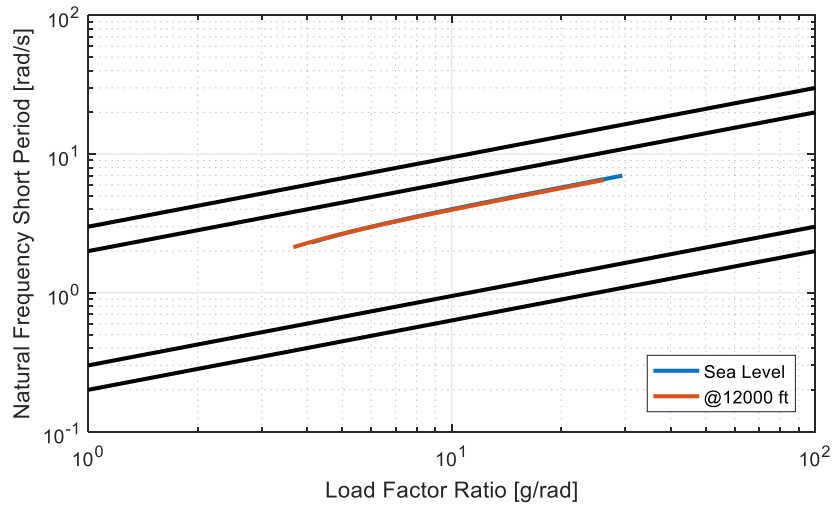


**Figure 77: Flight quality (MIL-F-8785C) related to the second period mode for the 4PAX aircraft.**

#### 10.4. Lateral-Directional Dynamic Stability

For the analysis of the lateral-directional dynamic stability of the 4PAX aircraft it was simulated the response of the aircraft to a cross wind of 10 m/s. Figure 78 shows on the left the aircraft's roll rate over time. As expected, the aircraft behaves in a convergent manner, i.e., there is a decay rate of the amplitudes over time. The analysis of the variation of the sideslip angle is shown in the right in Figure 78, where it is also possible to observe the convergent behavior of the aircraft in response to the lateral gust.

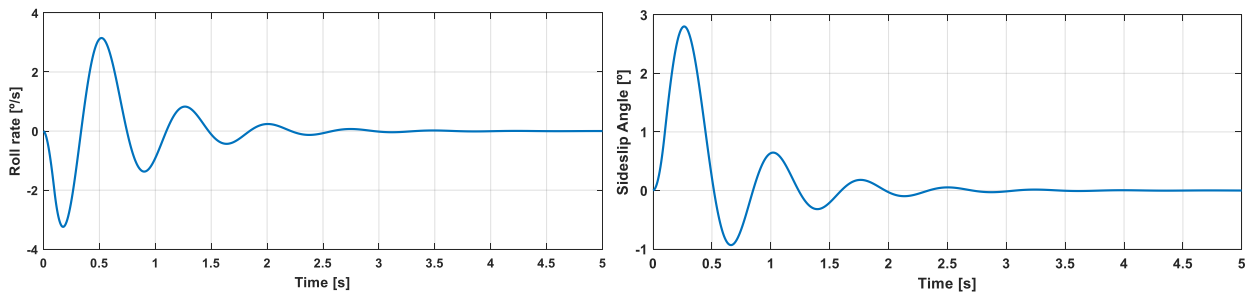


**Figure 78: Roll rate (on the left) and sideslip angle (on the right) over time for 4PAX aircraft.**

From the analyses performed for both aircraft, the following results are arranged:

**Table 34: Coefficients of dynamic stability for both aircraft.**

	$C_{n\beta}$	$C_{l\beta}$
Dolphin 4000	0.0632	-0.0866
Dolphin 6000	0.0910	-0.1061



## 11. Center of Gravity

During the entire design process, the evaluation of the center of gravity (C.G.) was one of the main concerns, since it affects the aircraft stability and, consequently, the control surfaces dimensions. Thus, a study of the contribution of each component was done in order to ensure the correct C.G. positioning, which are presented in Table 35 and illustrated in Figures 79 and 80.

**Table 35: Contribution of each component for the C.G. positioning of both aircraft.**

Component	4PAX			6PAX		
	Mass [kg]	X [m]	Y [m]	Mass [kg]	X [m]	Y [m]
Wing	115.21	3.76	0.40	115.21	3.80	0.40
Horizontal Tail	11.27	7.60	0.75	10.72	8.35	0.75
Vertical Tail	3.46	7.80	1.25	2.95	8.48	1.25
Fuselage	273.84	3.41	0.60	263.12	3.79	0.60
Main LG	62.93	3.92	0.00	64.23	3.85	0.00
Nose LG	23.24	1.57	0.00	23.59	1.55	0.00
Electrical Engine	89.21	0.50	0.60	89.21	0.50	0.60
Fuel System	16.21	3.76	0.40	13.45	3.80	0.40
Flight Control System	17.83	4.40	0.60	17.91	4.54	0.60
Hydraulic System	1.42	0.60	0.60	1.42	0.60	0.60
Avionics	32.85	1.11	0.60	32.85	1.11	0.60
Electrical System	41.51	0.55	0.60	40.30	0.55	0.60
Seats	53.38	3.91	0.78	53.38	4.20	0.78
ICE	163.29	1.11	0.60	163.29	1.11	0.60
Battery	300.00	6.23	0.60	300.00	6.82	0.60
Payload	399.20	3.91	0.78	598.80	4.20	0.78
Fuel	168.87	3.76	0.40	130.63	3.80	0.40
C.G. at MTOW		3.346	0.60		3.6645	0.60

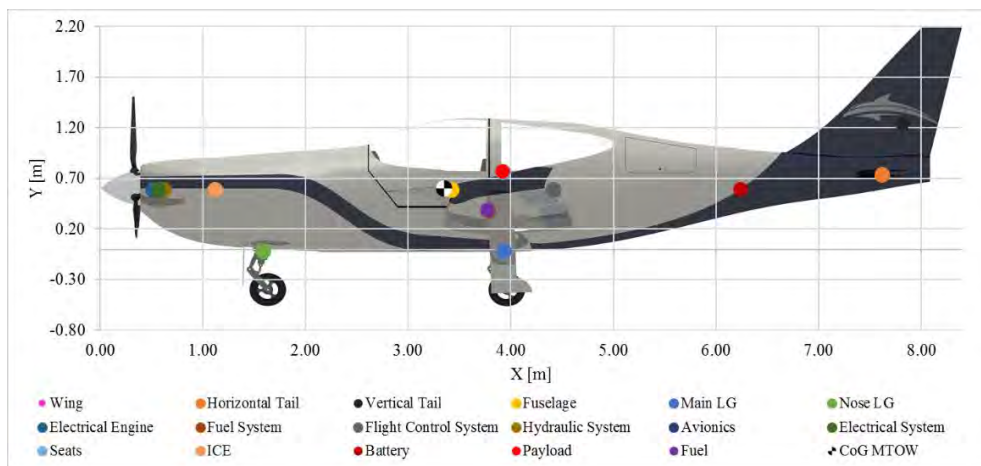


**Figure 79: C.G. distribution of each component for 4PAX aircraft.**

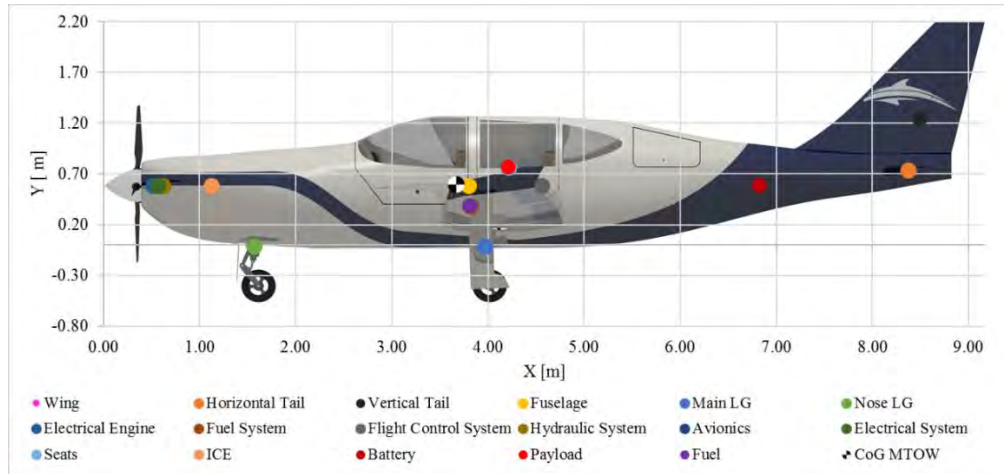


**Figure 80: C.G. distribution of each component for 6PAX aircraft.**

In order to construct the C.G. envelope of the aircraft, the procedures proposed by FAA-H-8083-1B were used. Based on the location of the components presented in the previous section, it was possible to calculate their moments and variations of payload and fuel position, together with the longitudinal stability limits of the aircraft presented in Section 10. Thus, it is possible to obtain the positions of the center of gravity that are safe for flight.

Figure 81 shows the CG envelope for the 4PAX and 6PAX aircraft.

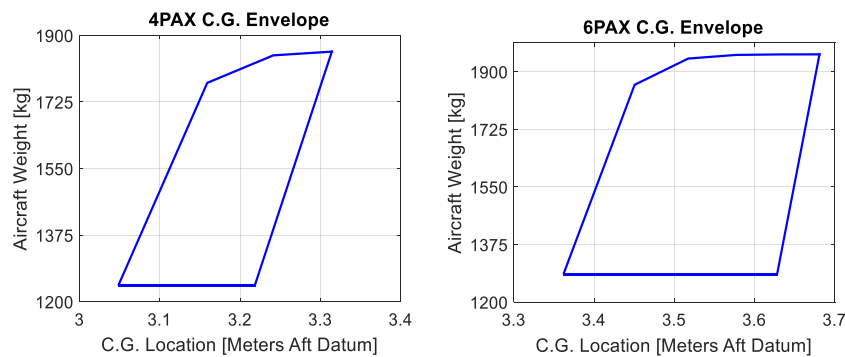


**Figure 81: 4PAX (on the left) and 6PAX (on the right) aircraft's C.G. envelopes.**

The 6PAX aircraft's C.G. envelope is wider than the one for 4PAX. This is due to the increase in the total length of the aircraft to accommodate the two additional passengers, which causes a greater sensitivity in the displacement of the components throughout the aircraft.



## 12. Subsystem Selections

### 12.1. Electric

The electric subsystem for the Dolphin 4000 and Dolphin 6000 is also common for both aircraft, featuring one generator driven by the engine. This generator outputs a voltage of 12 VAC and its power is used to recharge the auxiliary battery. The lead-acid battery is located in the nozzle of the aircraft and its mass is approximately 22 lb (10 kg). The power of the auxiliary battery is used to run avionics, lighting, ventilation systems, flaps and hydraulic subsystem. A scheme of the electric subsystem is shown in Figure 82.

The main avionic used is Garmin G2000, a premium touchscreen-controlled integrated flight deck designed for high performance piston aircraft. This integrated flight deck gives pilots rapid and intuitive access to vast amounts of flight, system, and sensor information, and also gives the pilot the ability to set how that information is presented.

It is worth noting that the electric subsystem is independent of the aircraft's hybridization system.

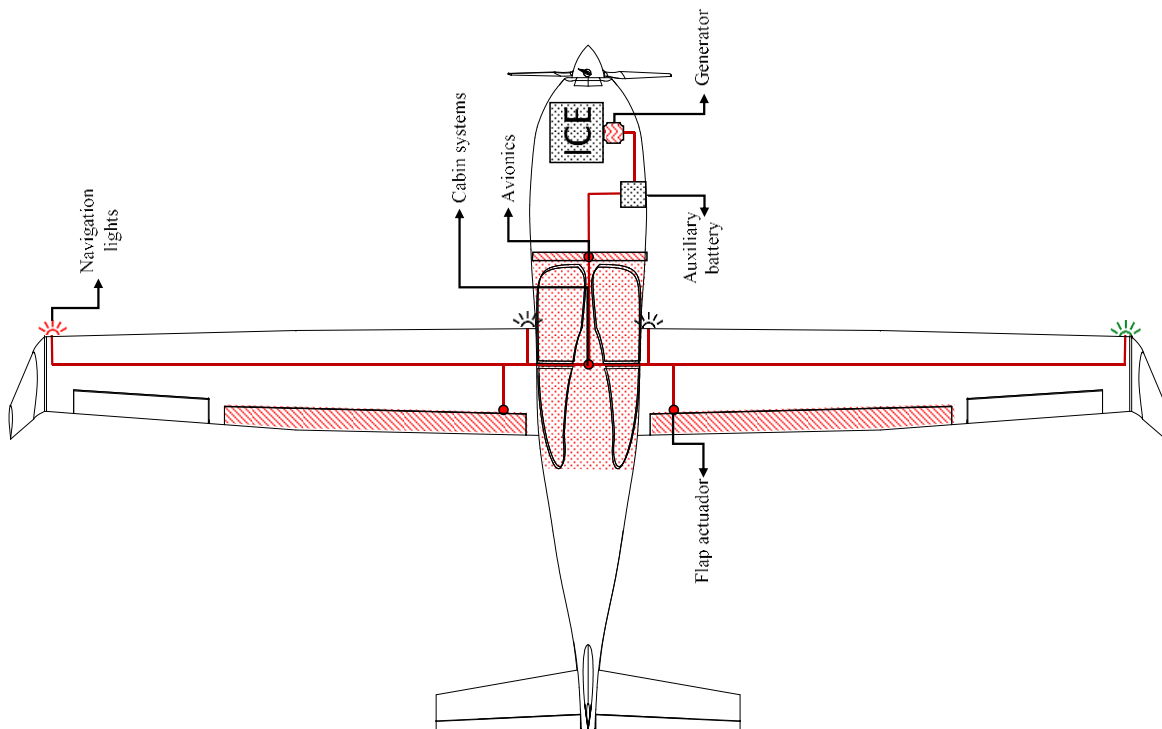


**Figure 82: Electric subsystem.**

### 12.2. Hydraulic

Because of the commonality approach, the hydraulic subsystem for the Dolphin 4000 and Dolphin 6000 are identical for both aircraft. This subsystem is only used for landing gear retraction and braking system. The hydraulic



pressure comes from a 12V hydraulic powerpack, which is a small unit that comprises an electric pump, filters, reservoir, valves, and pressure relief valve. The power to drive this pump is provided by an auxiliary battery. This hydraulic powerpack is located in the nozzle of the aircraft and its mass is approximately 11 lb (5 kg). An overview of the hydraulic subsystem is presented in Figure 83.

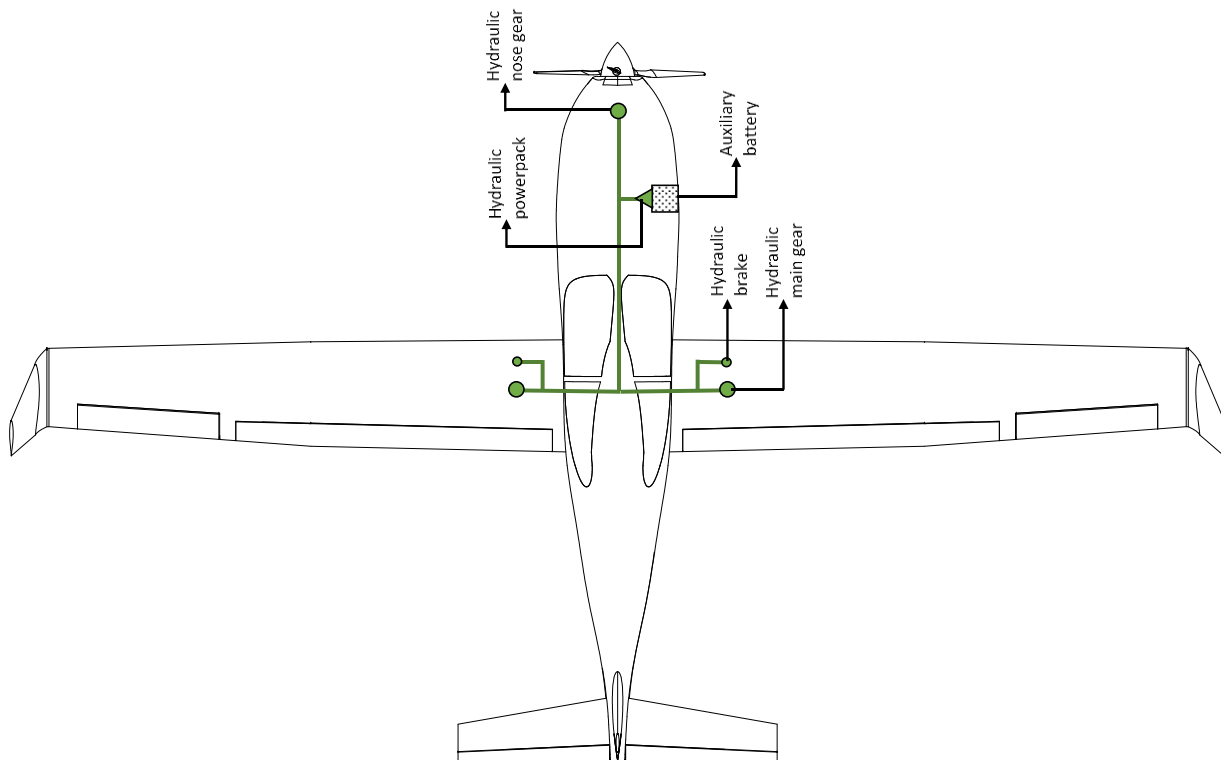


**Figure 83: Hydraulic subsystem.**

### 12.3. Fuel

To meet the specified fuel requirements, both Dolphin 4000 and Dolphin 6000 aircraft feature fuel tanks throughout the wings; consequently, the fuel subsystem is the same for both aircraft. The fuel used is the Jet-A/A1, which has a density of 0.804 kg/l. The fuel tanks have a capacity of 42.5 gallons (160.8 liters), divided into two tanks. To properly regulate the usage and flow of fuel, a central fuel hopper is utilized, allowing for crossflow between tanks to help adjust the center of gravity in flight. For refueling, over-wing gravity refueling is used. The fuel is sent from the tank to the injection system through a fuel pump driven by the engine. A scheme of the fuel subsystem is presented in Figure 84.

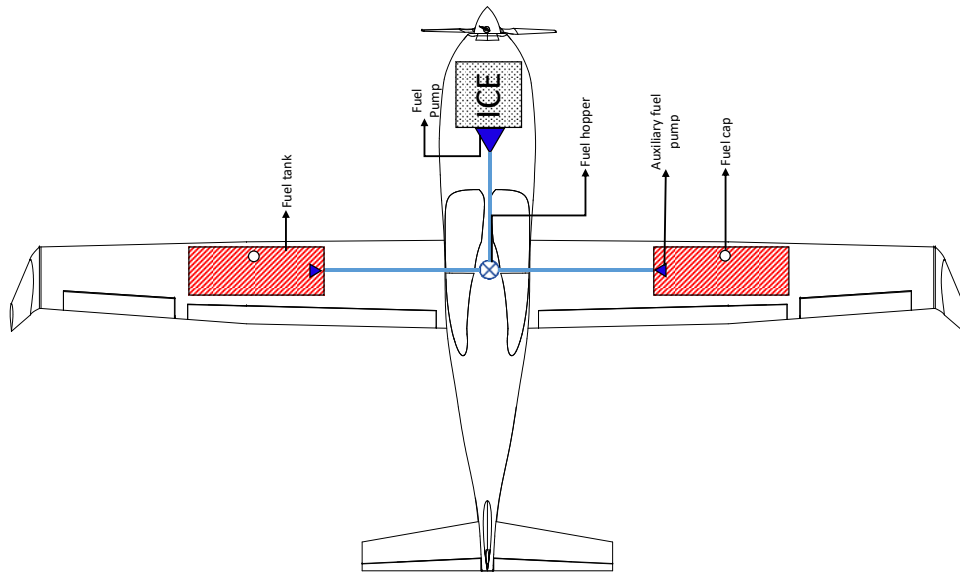


**Figure 84: Fuel subsystem.**

#### 12.4. Control

The control subsystem of Dolphin 4000 and Dolphin 6000 are the same. All control surfaces are actuated by cables and sheaves, except the flaps. One end of each cable is connected to a sheave attached to the stick, and another end of each cable is connected to a sheave attached to the control surfaces (called the control sheave). Cables and sheaves also actuate the trim-tabs, while flaps are driven by electric actuators. An overview of the control subsystem is presented in Figure 85.

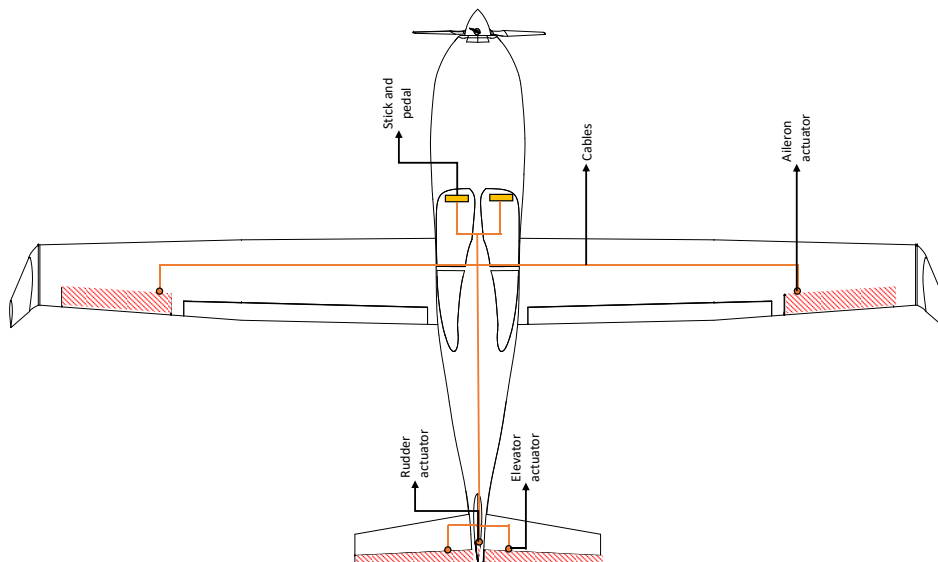


**Figure 85: Control subsystem.**



Both Dolphin 4000 and Dolphin 6000 aircraft have stick shaker and stick pusher. The stick shaker corresponds to a stick vibration system that works to alert the pilot about the imminence of stall occurrence. The stick pusher corresponds to an automatic actuation system of the stick that pushes the stick forward to lower the nose of the aircraft in case a critical angle of attack has been reached without the pilot taking any preventive action.

The control surfaces deflection about their hinges are illustrated in Figures 86, 87 and 88.

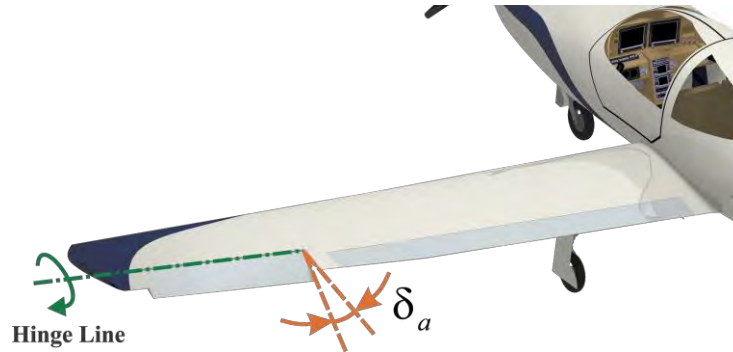


**Figure 86: Aileron deflection around its hinge.**

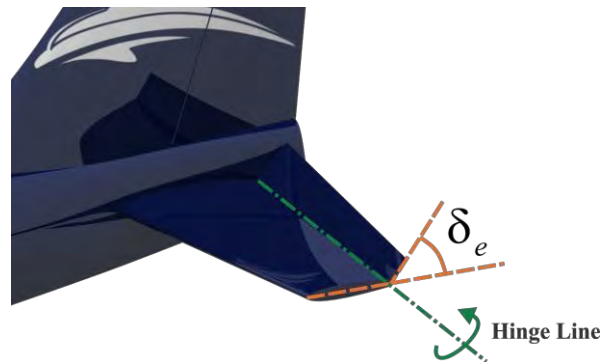


**Figure 87: Elevator deflection around its hinge.**

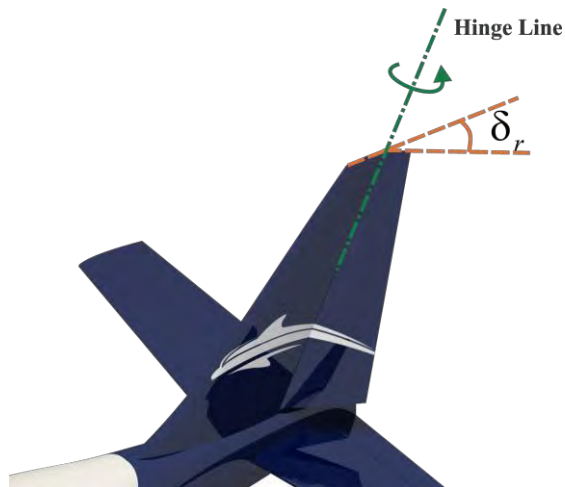


**Figure 88: Rudder deflection around its hinge.**



### 13. Landing Gear

The purpose of the landing gear is to allow the aircraft to return to the ground without causing damage to the structure. To accomplish this, the landing gear must not only react substantial forces and moments, but also provide a way to deliver the load safely into the airframe.

The tricycle landing gear arrangement has been chosen for the Dolphin 4000 and Dolphin 6000 due to its advantages compared to other configurations and aesthetic reasons. Within these advantages, it stands out that it is dynamically stable on the ground, becoming easier to maneuver. In addition, it presents good ground control in crosswinds, and also allows a better protection of the propellers against ground strike, among other advantages. Moreover, the landing gear location was confirmed to allow the plane to tip back  $15^\circ$  during takeoff (and leaving a margin of safety), which is presented in Figure 89.



**Figure 89: Aircraft is able to touch the ground at  $15^\circ$  without risk of tail strike.**

#### 13.1. Main landing gear

The main gear is a monowheel arrangement with suspension system with an oleo shock absorber and trailing link as shown in Figure 90. Trailing link landing gear is excellent at landing rough terrain, making the aircraft capable of taking off and landing on different runways (dirt, grass, metal mat, gravel, asphalt, and concrete). Another benefit is that the wheel contacts the ground aft of the main strut of the landing gear, which improves the longitudinal tip over criteria for the aircraft.



**Figure 90: Main landing gear.**



Retractable landing gear allowed substantial reduction in drag and increase in cruising speed, making aircraft more efficient. The main landing gear struts are mounted to ribs on the wing and retracted under hydraulic power into the belly of the fuselage. The retractable system is driven by a hydraulic powerpack. Figure 91 shows how the main gear fits into the wing-body fairing. With safety in mind, both aircraft have an emergency actuation system to allow the pilot to implant landing gear manually if the normal actuation mechanism fails.



**Figure 91: Main landing gear up.**

### **13.2. Nose landing gear**

The nose landing gear features monowheel arrangement with suspension system with an oleo shock absorber. A nose wheel steering wheel on the pilot side of the aircraft controls the nose gear. Nose landing gear is located into the nose of the airplane as previously shown in Figure 91.

## **14. Interior Design**

In the industry, the interior cabin design starts evaluating the interior space necessary to accommodate properly the passengers, pilot and baggage. The U.S. Federal Aviation Regulations (FAR) contain requirements for head impact protection, maximum G- loading, damage tolerant single load paths and so forth - but no minimum seat spacing requirements.

The United Kingdom (UK) Civil Aviation Authority (CAA) is currently the only regulatory body to prescribe minimum seat-space dimension. Thus, having the CAA Airworthiness Notice 64 (AN64) “Minimum Space for Seated



Passengers” as a reference, the interior sizing for both aircraft were designed. The dimensions chosen for the project are illustrated in Figure 92, and the actual drawings in CATIA are presented in Figure 93.



**Figure 92: Dimensions chosen for the interior design.**

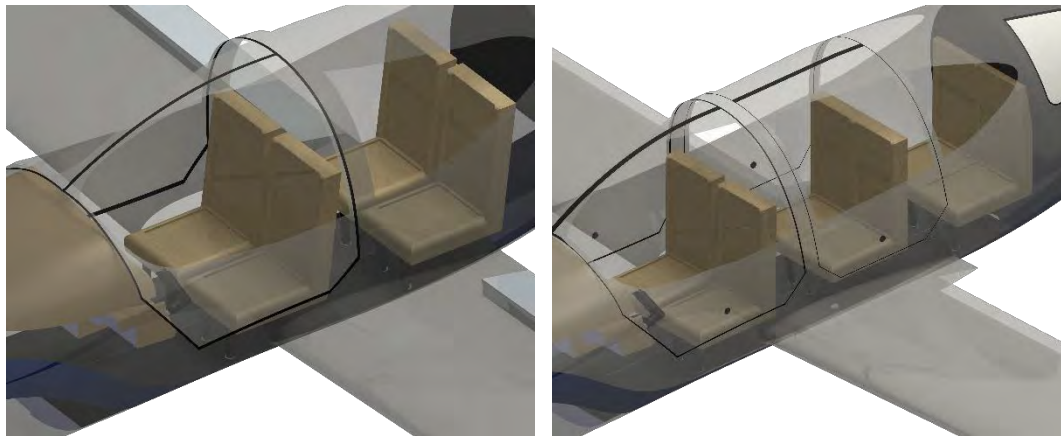


**Figure 93: Interior cabin of the 4PAX (on the left) and 6PAX (on the right) aircraft.**

Moreover, it was required that both aircraft had a compartment with enough space to storage baggage with weight per passenger/pilot of 30 lb and volume of at least 4 ft<sup>3</sup> per passenger. Therefore, after arranging the internal space, the baggage compartments have the following characteristics, presented in Table 36 and confirmed from CATIA in Figures 94 and 95.

**Table 36: Baggage compartment volumes.**

Aircraft	Volume [m <sup>3</sup> ]	Volume [ft <sup>3</sup> ]
4PAX	0.455	16.1
6PAX	0.763	26.9

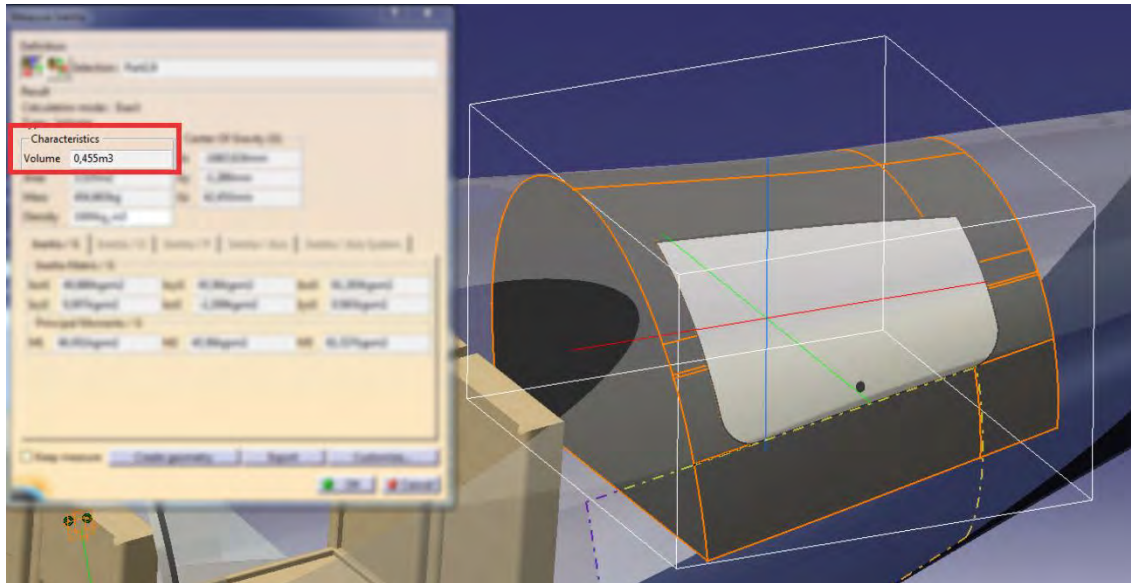


**Figure 94: Baggage compartment volume displayed on CATIA for the 4PAX aircraft.**

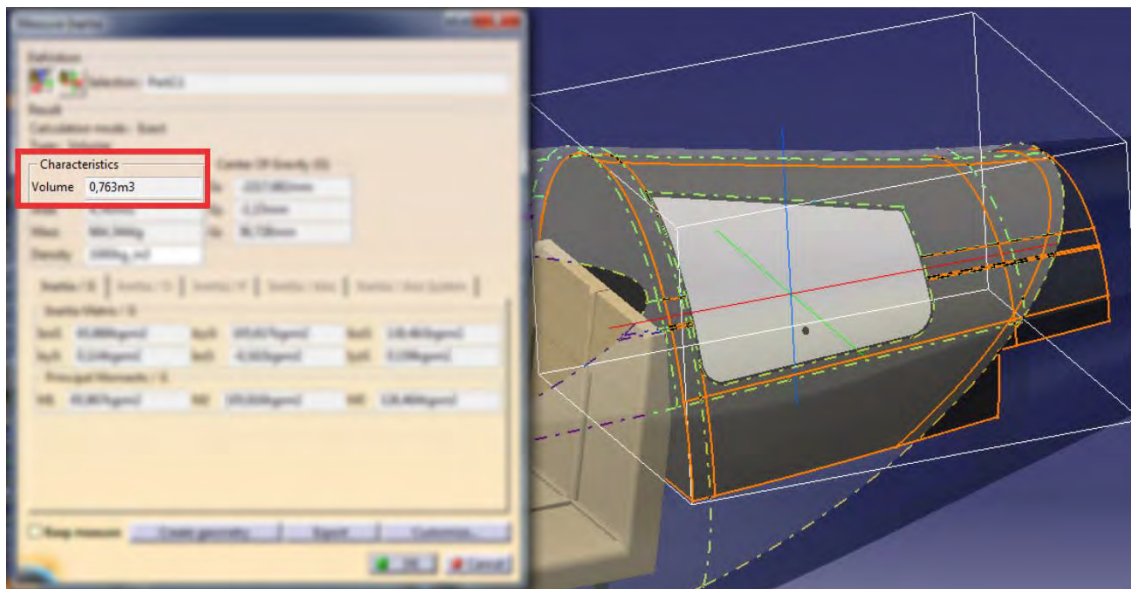


**Figure 95: Baggage compartment volume displayed on CATIA for the 6PAX aircraft.**

#### **14.1. Thermal & Acoustic Insulation**

For any aircraft it is important to ensure thermal and acoustic comfort. Therefore, the aerospace industry has spent some effort to design silent internal cabins with enjoyable climate.

The thermal environment outside an airplane produces fuselage skin temperatures from about -60 °F when in flight at altitude to about +160 °F when parked in direct sunlight in the desert. The amount of insulation needed for the



air conditioning/heating system to economically produce comfortable cabin temperatures varies with airplane type and location. On the other hand, outside noise is generated by aerodynamics and engines. Insulation is used to attenuate outside noise to allow reasonable levels of comfort and verbal communication inside the passenger cabin and cockpit.

Therefore, for both aircraft, it has been designed the following components for the insulation system:

- Fiberglass batting encapsulated in a plastic pillowcase covering distributed along the aircraft;
- Skin-dampings glued to the fuselage-skin to absorb vibration;
- Vibration isolators to support the internal panels;
- Felt with viscoelastic material along the cabin.

#### 14.2. Alternative Cabin Options

The internal space of the 4PAX aircraft is very reduced. Thus, for the cargo and maritime surveillance variants, if two passenger-seats and the baggage compartment are removed, it will be released some useful space, which could be properly arranged for cargo transportation, or even loading more batteries for maritime surveillance. In this case, it would certainly generate a new performance (range and endurance), which is very desirable for that application.

On the other hand, the 6PAX aircraft's fuselage is longer. Therefore, it comprises more internal space. So, removing four passenger-seats and the baggage compartment, it would release a lot of space (red volume of 8820 ft<sup>3</sup> in Figure 96), which could be also used as a huge cargo compartment or placing a pack of batteries for maritime surveillance.

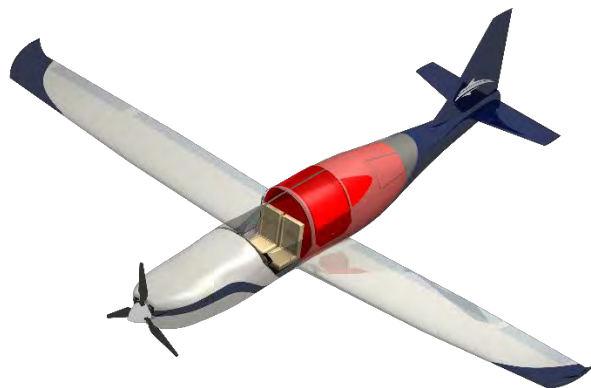


**Figure 96: Red volume representing the available internal space for variants.**



### 15. Geometric Configurations

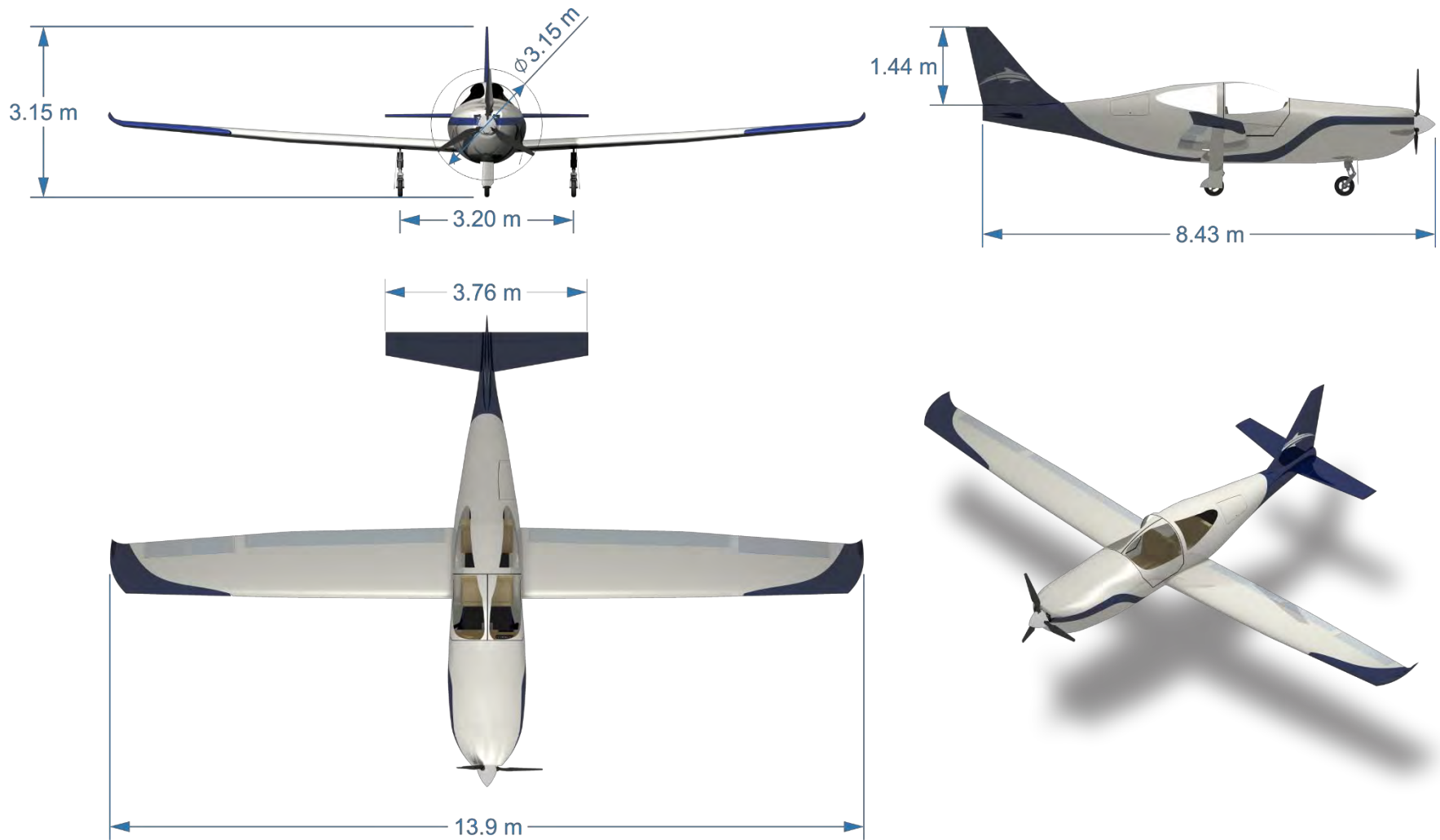


Figure 97: 4PAX aircraft final dimensions.

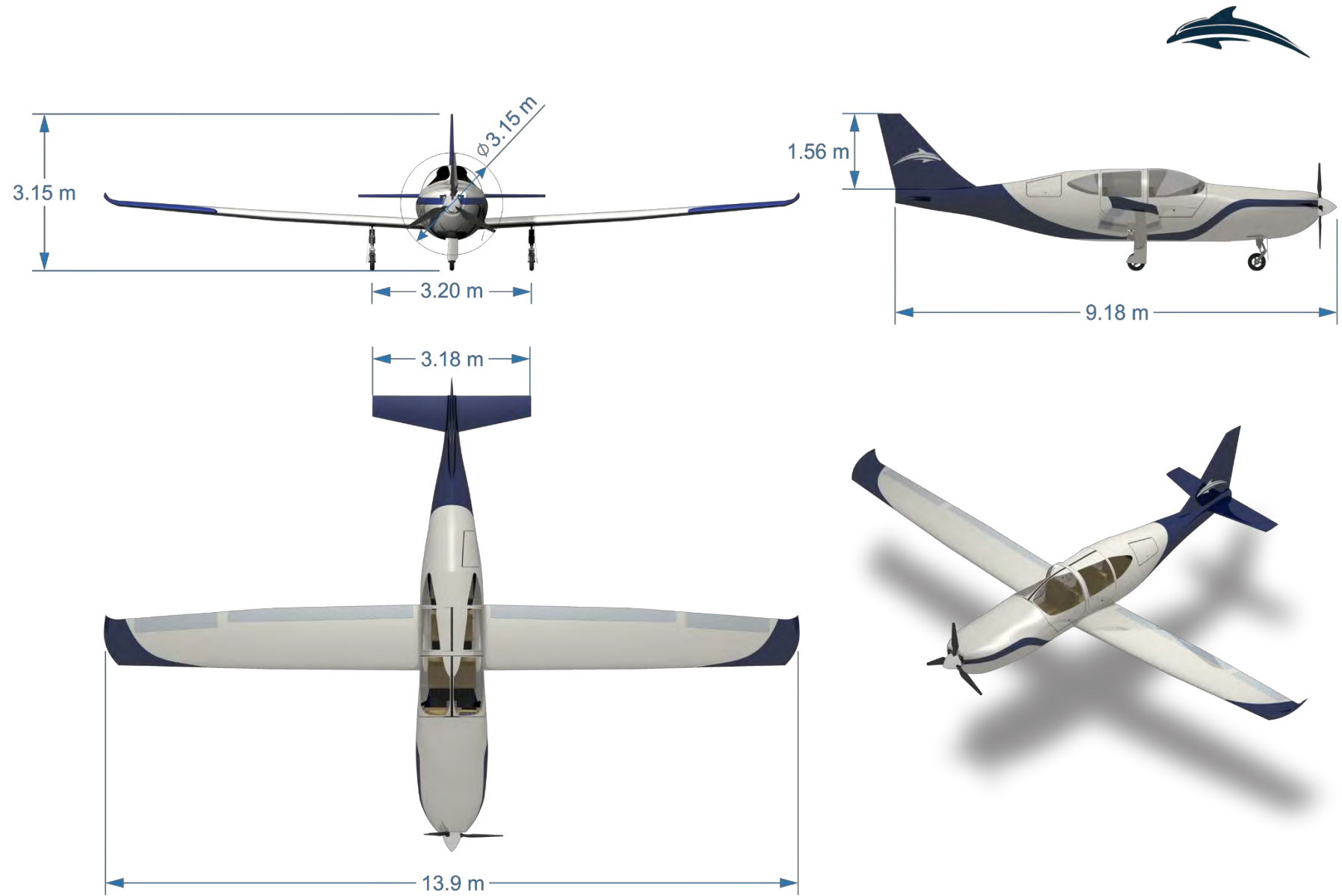


Figure 98: 6PAX aircraft final dimensions.



## 16. Cost Analysis

### 16.1. Development and Production Costs

Development and production costs are crucial when evaluating the economic viability of a hybrid aircraft over conventional aircraft in the market.

The price estimation model used was based on the Snorri Gudmundsson's formulation and on the Development and Procurement Cost of Aircraft, Version IV (DAPCA-IV). This model considers variable and fixed cost factors of production.

The variable costs are comprised of components purchased from third parties, such as avionics, engines and propellers, and vary in the reduction in the number of units acquired given by the *QDF* factor.

$$QDF = (F_{EXP})^{1.4427 \ln(N_{month})} \quad (4)$$

where  $F_{EXP}$  is the experience effectiveness (assumed as 0.8) and  $N_{MONTH}$  is the total number of aircraft produced per month.

The fixed costs depend directly on the number of aircraft produced per month, which are the costs of: Total Cost to Certify (Cost of Flight, Cost of Flight Testing and Cost of Flight), Total Cost of Manufacturing, Total Cost of Quality Control, and Total Cost of Materials. There are also some assumed values based on the cost of production of this type of aircraft shown in Table 38.

**Table 37: Rate per hour from labor man-hours.**

Labor	Rate per hour [\$/hr]
Engineering Labor Man-hours	80
Tooling Labor Man-hours	28
Manufacturing Labor Man-hours	24

The admitted sales profit was 10% and cost estimates were also adjusted for expected inflation in the year of service entry – 2028 for 4PAX and 2030 for 6PAX.

As shown in Section 4.4 the aircraft family has a commonality of 96%, where they share the same wing. Analyzing separately the production costs of each aircraft, the cost of production had a small variation, showing that the high communality of the family generated important economic benefits for the project. Figure 99 presents the selling price for 4PAX and 6PAX aircraft according to their production for a 5-year production to break-even.

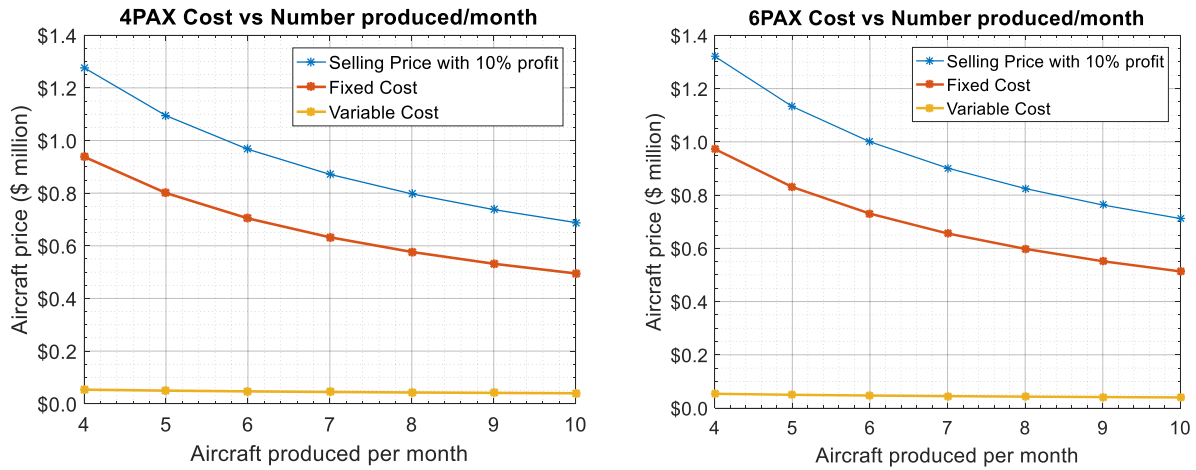


**Figure 99: 4PAX and 6PAX selling price over 5 years production to break-even.**

To create a competitive aircraft in the market, the volume of production of the competitors in the first five years of production was analyzed, where the production rate was around 6 aircraft per month, which is the value adopted for the project. Thus, the sale value of the aircraft will be \$ 966,700.00 for the 4PAX and \$ 1,000,000.00 for the 6PAX.

The development and production value of the two aircraft based on a sale of 360 aircraft over 5 years is \$ 253,590,000.00 for 4PAX and \$ 262,950,000.00 for 6PAX. Figures 100 and 101 present the breakdown values for both aircraft.

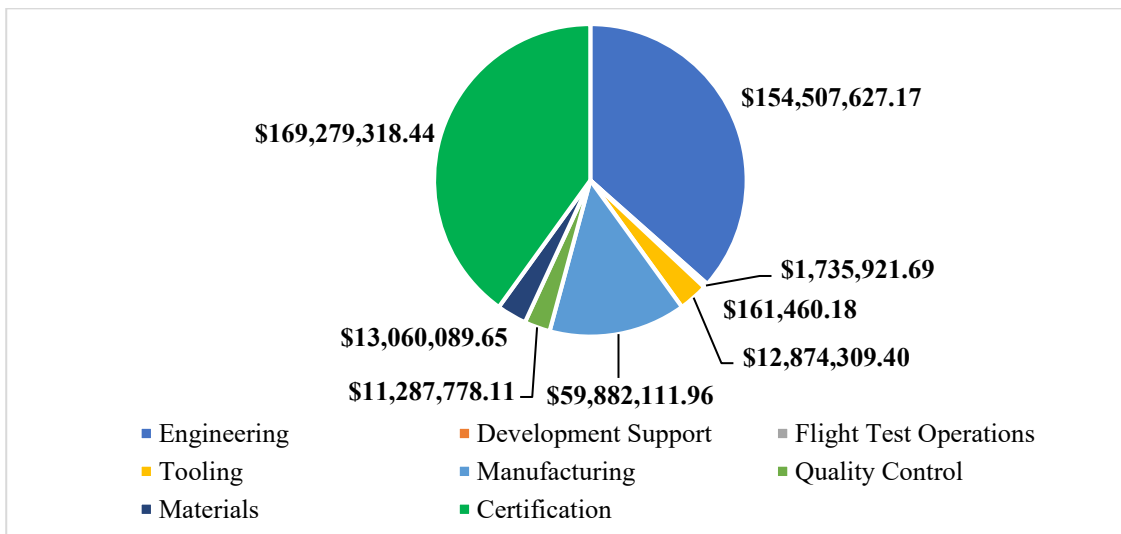


**Figure 100: 4PAX breakdown of costs on sales of 360 aircraft over 5 years.**

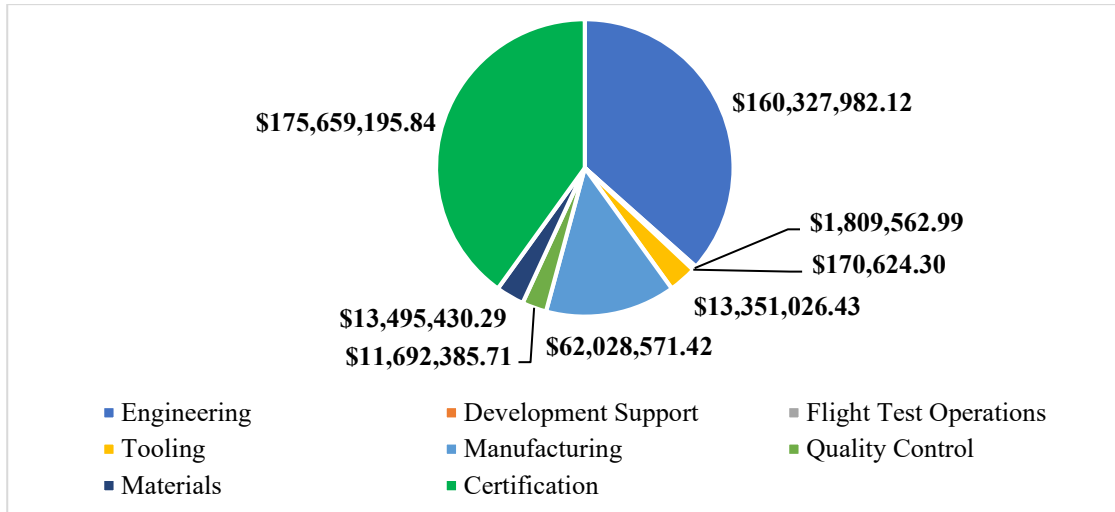


**Figure 101: 6PAX breakdown of costs on sales of 360 aircraft over 5 years.**

However, it is necessary to consider the fact that the 6PAX aircraft will enter the market only 2 years after 4PAX. To ensure a high penetration and greater visibility of the aircraft in the market, in the first 2 years of production the production rate of the 4PAX aircraft will be 6 aircraft per month and after the second year its rate will be reduced to 3 aircraft per month, complemented by the production of 3 aircraft/month of the 6PAX model. Thus, the actual breaking-even point curve is shown in Figure 102.

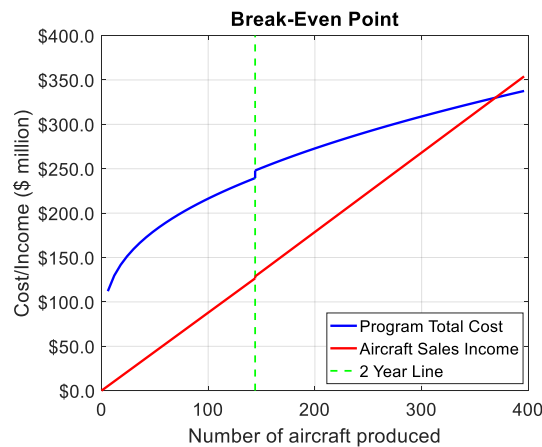


**Figure 102: Production break-even point for 5 years projection.**

It is possible to observe that the breaking-even point occurred in 369 aircraft, i.e., 9 more aircraft than expected. This is due to the lower sales income in the first 2 years. An increase to 7 aircraft/month would not justify this difference, so it would be better to create a plan to include the production of 9 more aircraft during those five years or to realize that the breaking-even point will occur 45 days after the expected if the rate of 6 aircraft/month is maintained.



## 16.2. Operational Cost

The operational cost of the first year of operation of the aircraft is the sum of fuel costs, maintenance, hangar, insurance, inspections, engine overhaul and battery recharge. The price of the Jet-A/A1 fuel assumed was \$ 4.98, the hourly rate for mechanic work is assumed to be \$ 53/hr, the cost of hangar storage is assumed to be \$ 250/month, and the kWh price was assumed to be \$ 0.12/kWh.

Thus, Snorri Gudmundsson's model can estimate the operating price of aircraft per hour and Figure 103 shows the operational cost estimation.

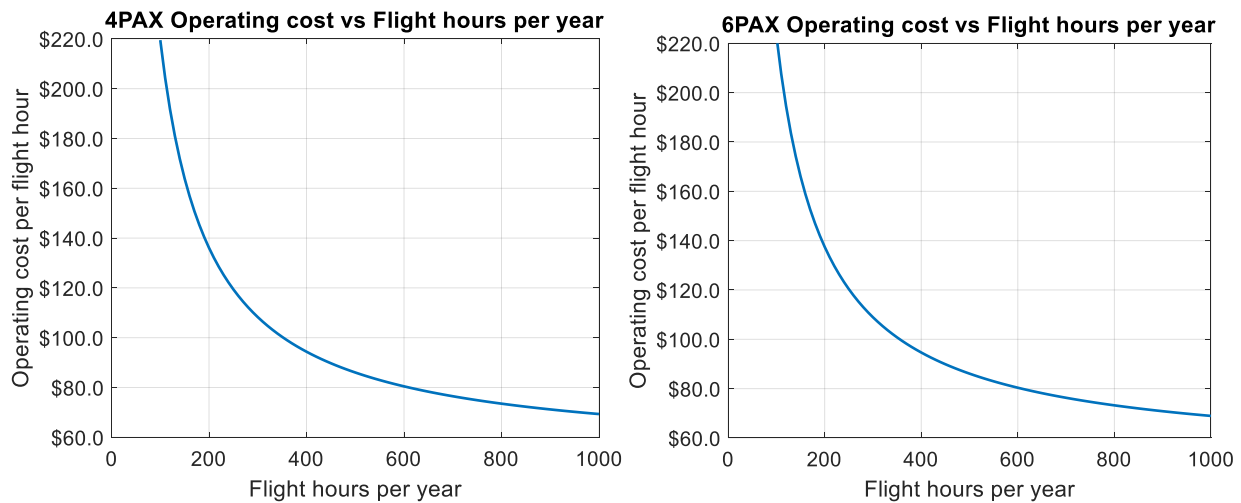


**Figure 103: 4PAX and 6PAX cost per flight hour with number of hours flown per year.**

It is possible to see that the cost of flight hours for the 4PAX aircraft is practically the same as that for the 6PAX. This happens because the first one has a longer range, being necessary greater use of fuel and battery, while the second one uses less fuel and less battery, but it has more expensive insurance for the higher selling price of the aircraft.

Considering that both aircraft have an annual flight rate of 300 hours, the operating cost per hour of flight for the 4PAX aircraft is \$ 108.27 and for the 6PAX is \$ 108.93. Figures 104 and 104 give a summary of the hourly flight costs of each aircraft.

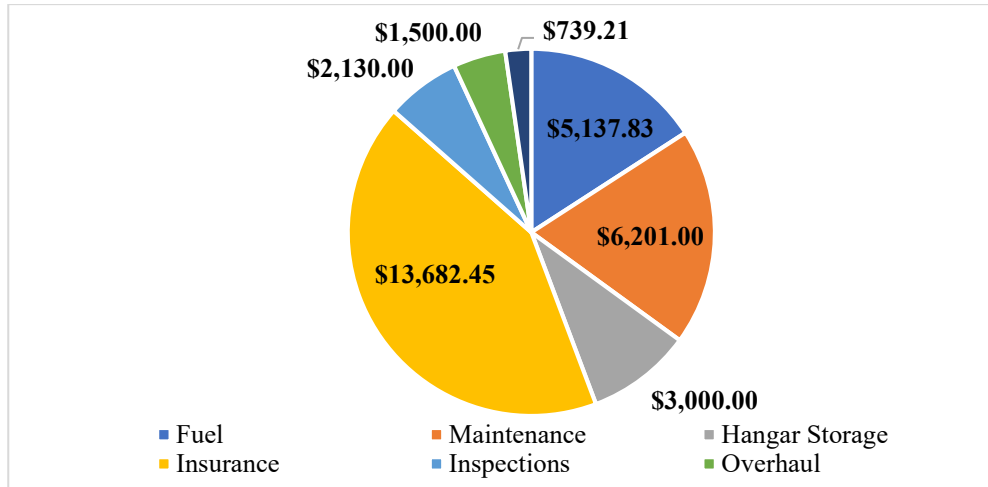


**Figure 104: 4PAX operating cost breakdown.**

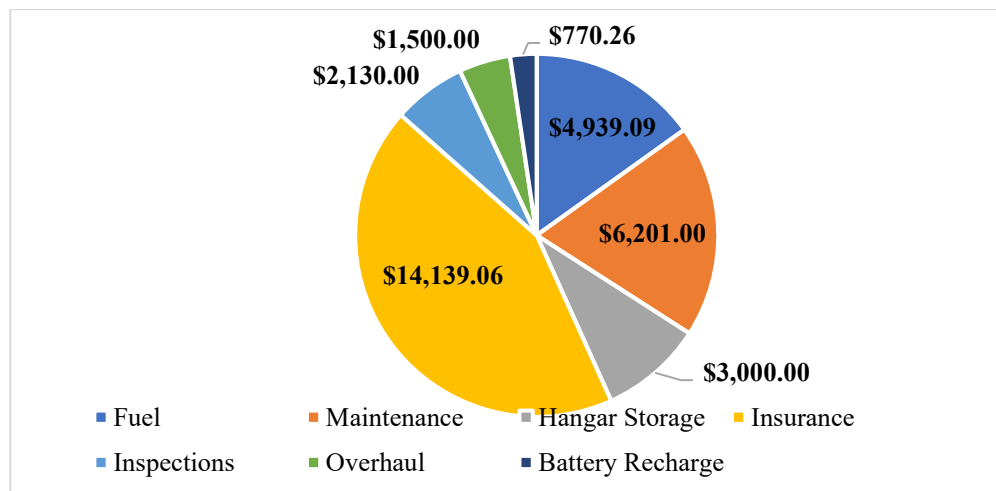


**Figure 105: 6PAX operating cost breakdown.**

It is expected that a hybrid aircraft will have a higher cost per unit of aircraft than the competitors, and the great feature of this type of aircraft is the hourly cost per flight. Table 38 presents a comparison between the sales figures and operating costs of the 4PAX aircraft and its competitors.

**Table 38: Comparison between the sale price and the cost per flight hour to the competitors.**

Aircraft Model	Sale Price	Cost Per Flight Hour
4PAX	\$966,700.00	\$108.27
Diamond DA42	\$522,750.00	\$223.00
Cirrus SR22	\$724,900.00	\$173.00
Cessna TTx	\$733,950.00	\$170.64



Thus, it is possible to estimate how much time of use of the 4PAX aircraft the buyer will need to make a profit, compared to the others. Table 39 shows the amount of time to obtain a break-even point in relation to the aircraft's flight time per year.

**Table 39: Comparison of the break-even point to the competitors.**

<b>Aircraft Model</b>	<b>100 hour/year</b>	<b>200 hours/year</b>	<b>300 hours/year</b>	<b>400 hours/year</b>	<b>500 hours/year</b>
Diamond DA42	38.70 years	19.35 years	12.90 years	9.67 years	7.74 years
Cirrus SR22	37.36 years	18.68 years	12.45 years	9.34 years	7.47 years
Cessna TTx	37.32 years	18.66 years	12.44 years	9.33 years	7.46 years

Therefore, for commercial applications, this type of aircraft is feasible only for operators with a high flight load. However, this estimate does not consider the price variation of the fuel over the years. Even though hybrid aircraft still have some economically issues compared to conventional competitors in the market, their features offer many advantages in the future, even more when new electric batteries are expected.

## 17. Conclusions

The Dolphin family fulfills the requirements proposed by the AIAA's RFP. The design featured two aircraft (4PAX and 6PAX) able to compete against the competitors, showing to the market that they are good alternatives to existing airplanes, even though entering in service by 2028.

In this work, the conceptual design used a genetic algorithm, which combined multi-interfaces, and resulted in very good geometries. Next, performing aerodynamic and structural analyses, the main characteristics were obtained, allowing evaluations in performance and stability. Thus, the project has achieved good attributes and essential qualities for aeronautical design. Nonetheless, both aircraft share 96% of commonality, which facilitates the manufacturing and reduces fixed costs.

After all, the "icing on the cake" of this report is the electric-hybrid propulsive system. No doubt this is going to be the future. The companies and the industry seek for these more efficient and sustainable technologies, which would allow reduction of fuel consumption, reduction of noise during landing, improvement of cruise performance, and aid in the reduction of greenhouse gas emissions. However, there are many issues involving these new approaches, since more electric systems imply the need to generate more power, distribute power to more places, and deal with more waste heat than ever before. Therefore, the development of new architectures and devices will be essential.



## 18. Bibliography

- [1] Air Transport Action Group (ATAG), *The Right Flightpath to Reduce Aviation Emissions*, Durban, South Africa, 2010.
- [2] “Annual Energy Outlook 2012,” DOE/EIA-0383(2012), U.S. Energy Information Administration, U.S. Dept. of Energy, Washington, D.C., 2012
- [3] R. Muller, *ACARE Goals (AGAPE) Progress Evaluation, Project Final Report Publishable Summary*, 2010.
- [4] Seeckt, K. *Performance assessment of part-electric General Aviation aircraft*. Hochschule für Angewandte Wissenschaften Hamburg, Hamburg, 2006.
- [5] Girishkumar, G., McCloskey, B., Luntz, A.C., Swanson, S., Wilke, W.: Lithium-air battery: promise and challenges. *J. Phys. Chem. Lett.* 1(14), 2193–2203 (2010)
- [6] Hepperle, M. *Electric Flight – Potential and Limitations*. German Aerospace Center. Institute of Aerodynamics and Flow Technology. Braunschweig, Germany. 2012.
- [7] Friedrich, C., and Robertson P.A. “Hybrid-Electric Propulsion for Aircraft”, *Journal of Aircraft*, Vol. 52, No. 1 (2015), pp. 176-189.
- [8] *Plane & Pilot Magazine*. (2017). *Hybrid Aircraft? - Plane & Pilot Magazine*. [online] Available at <http://www.planeandpilotmag.com/article/hybrid-aircraft/#.Wh59E0pKs2w> [Accessed 29 Nov. 2017].
- [9] Engadget. (2017). *Airbus, Rolls-Royce and Siemens team on a hybrid electric aircraft*. [online] Available at: <https://www.engadget.com/2017/11/28/airbus-e-fan-x-hybrid-electric-aircraft/> [Accessed 29 Nov. 2017].
- [10] *Layout Geral de Aeronaves* [Powerpoint slides]. Personal Collection of Giuliano Gardolinski Venson for Aircraft Design, Aeronautical Engineering Program, Faculty of Mechanical Engineering, Federal University of Uberlândia, Uberlândia, Minas Gerais, 2013.
- [11] *Estimativa da Polar de Arrasto de Aeronaves* [Powerpoint slides]. Personal Collection of Giuliano Gardolinski Venson for Aircraft Design, Aeronautical Engineering Program, Faculty of Mechanical Engineering, Federal University of Uberlândia, Uberlândia, Minas Gerais, 2015.
- [12] *Estimativa de Pesos de Aeronaves* [Powerpoint slides]. Personal Collection of Giuliano Gardolinski Venson for Aircraft Design, Aeronautical Engineering Program, Faculty of Mechanical Engineering, Federal University of Uberlândia, Uberlândia, Minas Gerais, 2015.



- [13] Dimensionamento Inicial de Aeronaves [Powerpoint slides]. Personal Collection of Giuliano Gardolinski Venson for Aircraft Design, Aeronautical Engineering Program, Faculty of Mechanical Engineering, Federal University of Uberlândia, Uberlândia, Minas Gerais, 2015.
- [14] Balanceamento de Aeronaves e Distribuição de Pesos [Powerpoint slides]. Personal Collection of Giuliano Gardolinski Venson for Aircraft Design, Aeronautical Engineering Program, Faculty of Mechanical Engineering, Federal University of Uberlândia, Uberlândia, Minas Gerais, 2014.
- [15] Raymer, D. P. Aircraft design: a conceptual approach. 4th ed. Reston: AIAA Education, 2006.
- [16] Siemens. 2016. Aerobatic Airplane “Extra 330LE”. [ONLINE] Available at: <https://www.siemens.com/press/pool/de/events/2016/corporate/2016-12-innovation/inno2016-aerobatic-airplane-e.pdf>. [Accessed 14 September 2017].
- [17] Scholz, D., 2015. Aircraft Design. 1st ed. Hamburg, Germany: Hamburg University of Applied Sciences.
- [18] Ma, H., Wang, B., Fan, Y., & Hong, W. (2014). Development and characterization of an electrically rechargeable zinc-air battery stack. *energies*, 7(10), 6549-6557.
- [19] PennState. 2017. Efficiency of Inverters. [ONLINE] Available at: <https://www.e-education.psu.edu/eme812/node/738>. [Accessed 9 November 2017].
- [20] Photovoltaic-software. 2017. Electricity losses : AC and DC electrical wire voltage drop and energy losses. [ONLINE] Available at: [http://photovoltaic-software.com/DC\\_AC\\_drop\\_voltage\\_energy\\_losses\\_calculator.php](http://photovoltaic-software.com/DC_AC_drop_voltage_energy_losses_calculator.php). [Accessed 24 November 2017].
- [21] Home Power. 2017. Input Voltage & Controller Efficiency. [ONLINE] Available at: <https://www.homepower.com/input-voltage-controller-efficiency>. [Accessed 24 November 2017].
- [22] International Journal of Engine Research. 2017. Maximum efficiencies for internal combustion engines: Thermodynamic limitations. [ONLINE] Available at: <http://journals.sagepub.com/doi/abs/10.1177/1468087417737700>. [Accessed 24 November 2017].
- [23] Transformative Vertical Flight Workshop. 2015. Electric propulsion components with high power densities for aviation. [ONLINE] Available at: <https://nari.arc.nasa.gov/sites/default/files/attachments/Korbinian-TVFW-Aug2015.pdf>. [Accessed 29 November 2017].



- [24] EPI, Inc. 2017. Propeller Performance Factors. [ONLINE] Available at: [http://www.epi-eng.com/propeller\\_technology/selecting\\_a\\_propeller.htm](http://www.epi-eng.com/propeller_technology/selecting_a_propeller.htm). [Accessed 6 September 2017].
- [25] Voskuijl, M., 2017. Analysis and design of hybrid electric regional turboprop aircraft. *Journal of Aircraft*, 52, 11.
- [26] IVAO Aero. 2017. Top of Descent Calculation. [ONLINE] Available at: [https://www.iviao.aero/training/documentation/books/SPP\\_APC\\_Top\\_of\\_descent.pdf](https://www.iviao.aero/training/documentation/books/SPP_APC_Top_of_descent.pdf). [Accessed 29 September 2017].
- [27] Hepperle, M. Electric Flight–Potential and Limitations. German Aerospace Center. Institute of Aerodynamics and Flow Technology. Braunschweig, Germany. 2012.
- [28] Bruce, P. G., Freunberger, S. A., Hardwick, L. J., & Tarascon, J. M. (2012). Li-O<sub>2</sub> and Li-S batteries with high energy storage. *Nature materials*, 11(1), 19-29.
- [29] Ji, X., & Nazar, L. F. (2010). Advances in Li–S batteries. *Journal of Materials Chemistry*, 20(44), 9821-9826.
- [30] Toussaint, G., Stevens, P., Akrou, L., Rouget, R. & Fourgeot, F. Development of a rechargeable zinc-air battery. *ECS Trans.* 28, 25–34 (2010).
- [31] Zhang, X. G. (2007). U.S. Patent No. 7,291,186. Washington, DC: U.S. Patent and Trademark Office.
- [32] Hermann, W. A., Straubel, J. B., & Beck, D. G. (2017). U.S. Patent No. 9,559,532. Washington, DC: U.S. Patent and Trademark Office.
- [33] IATA. 2017. Fuel Price Analysis. [ONLINE] Available at: <http://www.iata.org/publications/economics/fuel-monitor/Pages/price-analysis.aspx>. [Accessed 8 December 2017].
- [34] U.S. Energy Information Administration. 2017. Average Price of Electricity to Ultimate Customers by End-Use Sector. [ONLINE] Available at: [https://www.eia.gov/electricity/monthly/epm\\_table\\_grapher.php?t=epmt\\_5\\_6\\_a](https://www.eia.gov/electricity/monthly/epm_table_grapher.php?t=epmt_5_6_a). [Accessed 8 December 2017].
- [35] Storn, R., & Price, K. (1997). Differential evolution—a simple and efficient heuristic for global optimization over continuous spaces. *Journal of global optimization*, 11(4), 341-359.
- [36] U.S. Government Publishing Office. 2002. 14 CFR 23.335 - DESIGN AIRSPEEDS.. [ONLINE] Available at: <https://tinyurl.com/designairspeeds>. [Accessed 17 November 2017].
- [37] Eshelby, M., 2000. *Aircraft Performance: Theory and practice*. 1st ed. Burlington, MA: Elsevier.



- [38] MIT. 2017. Wing Bending Calculations. [ONLINE] Available at: <https://ocw.mit.edu/courses/aeronautics-and-astronautics/16-01-unified-engineering-i-ii-iii-iv-fall-2005-spring-2006/systems-labs-06/spl10.pdf>. [Accessed 2 November 2017].
- [39] Krupa, E., Cooper, J., Pirrera, A., & Silva, G. H. C. (2016). Aeroelastic Tailoring for Enhanced Aerodynamic Wing Performance. In 5th Aircraft Structural Design Conference Royal Aeronautical Society.
- [40] Tsai, S. W., & Wu, E. M. (1971). A general theory of strength for anisotropic materials. *Journal of composite materials*, 5(1), 58-80.
- [41] Wright, J. R., & Cooper, J. E. (2008). *Introduction to aircraft aeroelasticity and loads* (Vol. 20). John Wiley & Sons.